

**TEL AVIV UNIVERSITY**

The Iby and Aladar Fleischman Faculty of Engineering

**Patterning Large Scale  
Electronic Networks of  
Carbon Nanotubes**

A thesis submitted toward the degree of  
Master of Science in Electrical and Electronic Engineering

by

**Ze'ev R Abrams**

July 2007

**TEL AVIV UNIVERSITY**

**TEL AVIV UNIVERSITY**

The Iby and Aladar Fleischman Faculty of Engineering

# Patterning Large Scale Electronic Networks of Carbon Nanotubes

A thesis submitted toward the degree of  
Master of Science in Electrical and Electronic Engineering

by

**Ze'ev R Abrams**

This research was carried out in the Department of Electrical Engineering  
– Physical Electronics under the supervision of Dr. Yael Hanein

July 2007

# 1 Abstract

Using the tools established by the new field of Nanotechnology, many of the active components of electronic devices have been miniaturized down to the molecular level. These miniscule nano-elements and nano-materials have enhanced properties when compared to their bulk-fabricated counterparts. This is due to some of the unique physical processes encountered when approaching these small dimensions, such as quantum effects. Leading the research in nano-materials is the field of carbon nanotubes, whose properties have been found to be unrivaled for many diverse applications. However, when dealing with the fabrication aspects of integrating carbon nanotubes in nano-devices and, in particular, nano-circuitry, a major obstacle is encountered: How does one manipulate such nano-scaled objects so that they can be patterned, integrated and isolated from one another?

The research here describes a method of patterning individually isolated single-walled carbon nanotubes in a pre-arranged fashion using a method of nano-imprinting that is both independent of the substrate used, as well as completely IC compatible. The method entails the growth of nanotubes between micro-fabricated silicon pillars, creating a suspended network of taut nanotubes, and their subsequent imprinting onto different substrates, resulting in a large array of clean, straight and long nanotubes. The method does not require the substrate to be exposed to high temperatures, as is usually required to grow nanotubes on a surface, and can be used on various substrates and thin films.

An explanatory model of the formation of the suspended networks is described as well as the description and demonstration of a Raman spectroscopy mapping method. The Raman mapping can be used to identify the structure of each nanotube in the suspended array prior to imprinting, which can be used to integrate the stamping method into a more complete scheme of imprinting large arrays of nanotubes.

The results described here are among the best demonstrations of controlled placement of carbon nanotubes, and the method described can provide an integral technological advance towards the arrangement of molecular components on the nano-scale.

## **Acknowledgments**

The work described here encompassed three extremely productive and enjoyable years at Tel Aviv University. This thesis includes research done in both my undergraduate 4<sup>th</sup> year project in engineering, as well as my Master's degree, all under the supervision of Dr. Yael Hanein. My extreme appreciation goes to her guidance and assistance in these undertakings, without which, I would probably have been a depressed graduate student in some "second-rate" US school.

Special thanks goes to all the graduate students in Yael's research group [Tamir, Eyal, Itzik, Nimrod, Moti, Daniel, Nir, Raya, Orli, Alon, Asaf and Gaby], both past and present, who had to put up with my constant complaining. Some of them even taught me a thing or three.

Thanks go to the staff at the TAU microfabrication center, Mark Oksman and Alexander Gurevich, for assistance in many of the processes used. Also, thanks go to the staff at the TAU Nanoscience and Nanotechnology Center; especially Dr. Alexander Tsukernik, for his assistance with the HRSEM.

I would also like to thank Prof. Ori Cheshnovsky's lab, as well as the students in his lab, especially Zvika, who sat for many long hours searching for signals; and Prof. Gil Markovich and crew, who helped me with all sorts of questions on nanoparticles. Lastly, Dr. Yossi Lereah, whose assistance with the TEM earned me a couple of papers.



## **Table of Contents**

|          |  |            |
|----------|--|------------|
| <b>1</b> | <b>Abstract</b>                                | <b>i</b>   |
|          | <b>Acknowledgments</b>                         | <b>ii</b>  |
|          | <b>List of Figures:</b>                        | <b>v</b>   |
|          | <b>List of Abbreviations:</b>                  | <b>vii</b> |
| <b>2</b> | <b>Introduction:</b>                           | <b>1</b>   |
| 2.1      | Nanotechnology                                 | 1          |
| 2.2      | Top-Down vs. Bottom-up                         | 2          |
| 2.3      | Carbon Nanotubes                               | 4          |
| 2.3.1    | Carbon Nanotube Structure                      | 4          |
| 2.3.2    | Carbon Nanotube Growth                         | 7          |
| 2.4      | Carbon Nanotubes and Nanocircuitry             | 8          |
| <b>3</b> | <b>Literature Review:</b>                      | <b>10</b>  |
| 3.1      | SWCNT Characterization                         | 10         |
| 3.1.1    | TEM Analysis                                   | 11         |
| 3.1.2    | AFM Analysis                                   | 13         |
| 3.1.3    | SEM Analysis                                   | 14         |
| 3.1.4    | Carbon Nanotube Spectroscopy                   | 15         |
| 3.2      | SWCNT Devices                                  | 17         |
| 3.2.1    | CNT Transistors and Nanowires                  | 18         |
| 3.2.2    | SWCNT Sensors                                  | 20         |
| 3.3      | Nanotube Placement                             | 24         |
| 3.3.1    | Nanotemplates                                  | 24         |
| 3.3.2    | Catalyst Patterning                            | 25         |
| 3.3.3    | Field Alignment                                | 25         |
| 3.3.4    | Epitaxial Growth                               | 27         |
| 3.3.5    | Soft Lithography                               | 28         |
| 3.3.6    | Exact Positioning Patterning                   | 29         |
| 3.4      | Nanotubes between Pillars                      | 31         |
| <b>4</b> | <b>Research Goals</b>                          | <b>35</b>  |
| 4.1      | Significance and Context of this Project       | 36         |
| <b>5</b> | <b>Experimental Materials and Methods</b>      | <b>37</b>  |
| 5.1      | Fabrication Processes                          | 37         |
| 5.1.1    | Photo and E-Beam Lithography                   | 37         |
| 5.1.2    | RIE and DRIE                                   | 38         |
| 5.1.3    | E-Beam Evaporation and Sputtering              | 39         |
| 5.1.4    | Nanostrip and Oxygen Plasma Substrate Cleaning | 39         |
| 5.2      | CVD Nanotube Growth                            | 40         |
| 5.3      | Suspended Nanotube Process Flow                | 41         |
| 5.4      | Imaging and Spectroscopic Techniques           | 43         |
| 5.4.1    | HRSEM  | 43         |
| 5.4.2    | TEM  | 44         |
| 5.4.3    | Raman Spectroscopy                             | 45         |
| 5.5      | Stamping Method                                | 48         |

|       |   |    |
|-------|---|----|
| 5.6   | Electrical Measurement Systems                      | 48 |
| 6     | <i>Results</i>                                      | 49 |
| 6.1   | Pillar Design and Fabrication                       | 49 |
| 6.2   | CVD Growth of Suspended Nanotubes                   | 51 |
| 6.3   | Suspended Nanotube Analysis                         | 54 |
| 6.3.1 | Imaging Analysis                                    | 54 |
| 6.3.2 | Quantitative Analysis                               | 60 |
| 6.4   | TEM Analysis of Individual SWCNTs                   | 62 |
| 6.4.1 | Radial Deformation                                  | 62 |
| 6.4.2 | Twisting and Melting                                | 65 |
| 6.5   | Raman Spectroscopy Mapping                          | 66 |
| 6.6   | Stamping Networks of SWCNTs                         | 69 |
| 6.7   | TEM Stamping Verification                           | 73 |
| 6.8   | CNTFET Fabrication                                  | 75 |
| 6.9   | Electrical Measurements                             | 77 |
| 7     | <i>Summary, Conclusions and Future Developments</i> | 79 |
| 7.1   | Summary and Conclusions                             | 79 |
| 7.2   | Future Developments                                 | 81 |
| 8     | <i>References</i>                                   | 84 |
| 9     | <i>Appendix</i>                                     | 90 |
| 9.1   | The Physics of Raman Spectroscopy                   | 90 |
| 9.2   | Spectral Information from SWCNTs                    | 92 |
| 9.3   | Fabrication Recipes                                 | 96 |

## List of Figures:

|   |    |
|---|----|
| Figure 1: Moore's Law .....   | 2  |
| Figure 2: Carbon Nanotube Structure .....                                     | 4  |
| Figure 3: Internal Structure of a single-walled nanotube .....                | 5  |
| Figure 4: Density of states of a single-walled nanotube .....                 | 6  |
| Figure 5: Cover of Science, December 2001 .....                               | 9  |
| Figure 6: STM and TEM images .....  | 11 |
| Figure 7: TEM images of nanotubes .....                                       | 12 |
| Figure 8: AFM manipulation of a nanotube .....                                | 14 |
| Figure 9: HRSEM imaging of nanotubes .....                                    | 15 |
| Figure 10: Raman Spectroscopy of Carbon Nanotubes .....                       | 16 |
| Figure 11: Global Raman Mapping and Fluorescence of Nanotubes .....           | 17 |
| Figure 12: Single Walled Nanotubes as Quantum Wires .....                     | 19 |
| Figure 13: The IBM Nanotube Complementary Transistors .....                   | 20 |
| Figure 14: Nanotube Based Sensors .....                                       | 21 |
| Figure 15: Nanotube Flow Sensor .....   | 21 |
| Figure 16: Nanotubes in NEMS .....  | 22 |
| Figure 17: Infra-red Nanotube Photonics .....                                 | 23 |
| Figure 18: Nanotemplates for Nanotube Deposition .....                        | 24 |
| Figure 19: Catalyst Island Nanotube Growth .....                              | 25 |
| Figure 20: Electric Field Alignment .....                                     | 26 |
| Figure 21: Atomic Step Nanotube Growth .....                                  | 27 |
| Figure 22: Soft Lithography Transfer Printing .....                           | 28 |
| Figure 23: Cutting-Edge Controlled Placement Methods .....                    | 30 |
| Figure 24: Nanotubes Between Silicon Pillars .....                            | 32 |
| Figure 25: Bridging Nanotube Growth Analysis .....                            | 34 |
| Figure 26: Multiple Parallel Complementary CNTFETs on a Single Nanotube ..... | 36 |
| Figure 27: Computerized CVD System .....                                      | 40 |
| Figure 28: Suspended Nanotube Process Flow .....                              | 42 |
| Figure 29: HRSEM Artifacts .....  | 44 |
| Figure 30: TEM DuraSiN Grids .....  | 45 |
| Figure 31: Raman Bands from a Single Nanotube .....                           | 46 |
| Figure 32: Pillar Designs and Bad Etching .....                               | 50 |
| Figure 33: Additional Pillar Designs .....                                    | 51 |
| Figure 34: Suspended SWCNT networks .....                                     | 53 |
| Figure 35: Comparison of HRSEM and TEM Images of Suspended Growth .....       | 55 |
| Figure 36: Tube-Tube Zipper-Effect Model .....                                | 56 |
| Figure 37: Tube-Tube Interaction Images .....                                 | 57 |
| Figure 38: Tube-Surface Zipper-Effect Model .....                             | 58 |
| Figure 39: Tube-Surface Interaction Images .....                              | 59 |
| Figure 40: Binding Energy between Nanotubes .....                             | 61 |
| Figure 41: Radial Deformation Measurements .....                              | 64 |
| Figure 42: TEM Measurements of Twisting and Irradiation .....                 | 66 |
| Figure 43: Raman Mapping Images .....   | 67 |
| Figure 44: Intensity of Suspended Raman Signal .....                          | 68 |
| Figure 45: Initial Stamping Results .....                                     | 70 |
| Figure 46: Markings Made During Stamping Process .....                        | 71 |
| Figure 47: Best Stamping Results .....  | 73 |

|   |     |
|---|-----|
| Figure 48: TEM Verification of Stamped Nanotubes.....                     | 74  |
| Figure 49: Stamping onto Existing Electrodes .....                        | 75  |
| Figure 50 Electrodes Patterned on Stamped Nanotubes .....                 | 76  |
| Figure 51: I-V Characteristics of the CNTFETs.....                        | 77  |
| Figure 52: Conductance Measurements of a CNTFET .....                     | 78  |
| Figure 53: Complete Method for Stamping Nanotube Networks.....            | 80  |
| Figure 54: Possible Future Devices .....                                  | 82  |
| Figure 55: Local Gating of Perpendicular Sets of Aligned Nanotubes .....  | 83  |
| Figure 56: Graphical Representation of the Raman Effect.....              | 90  |
| Figure 57: Source of Raman Signal from a Diatomic Molecule .....          | 91  |
| Figure 58: Difference between Raman and IR Signals .....                  | 91  |
| Figure 59: Raman spectroscopy instrumentation. ....                       | 92  |
| Figure 60: Tables and Graphs of Spectral Information from Nanotubes ..... | 93  |
| Figure 61: Additional Images .....  | 102 |

***List of Abbreviations:***

- AFM – atomic force microscope
- CD – critical dimensions
- CMOS – complementary metal oxide silicon (transistors)
- CNT – carbon nanotube
- CNTFET – carbon nanotube field effect transistor
- CVD – chemical vapor deposition
- DI – de-ionized
- DOS – density of states
- DRIE – deep reactive ion etch (Bosch process)
- FEG – field emission gun
- HRSEM – high resolution scanning electron microscope
- IC –integrated circuit
- IR – infra red
- IRS – infra-red spectroscopy
- MEMS – micro electro mechanical systems
- MOSFET – metal oxide silicon field effect transistor
- MWCNT – multi-walled carbon nanotube
- NEMS – nano electro mechanical systems
- NMP – N-methyl-2-pyrrolidone
- PDMS – polydimethyl-siloxane
- PECVD – plasma enhanced chemical vapor deposition
- PMMA – polymethyl-methacrylate
- PR – photo-resist
- RBM – radial breathing mode
- RIE – reactive ion etch
- RS – Raman spectroscopy
- SAM – self assembled monolayer
- SC – semi-conducting
- SCCM – standard cubic centimeters per minute
- SEM – scanning electron microscope
- STM –scanning tunneling microscope
- SWCNT – single walled carbon nanotube
- TAU – Tel Aviv University
- TEM – transmission electron microscope
- TSI – tube surface interaction
- TTI – tube tube interaction
- vdW – van der Waals

## **2 Introduction:**

### **2.1 *Nanotechnology***

The field of solid-state devices has been advancing and reinventing itself at such a phenomenal rate that the scale and complexity of even a basic transistor has reached the nanoscale – nearly a billion times smaller than the first transistor created half a century ago. With the rapid advances in technology that both define the integrants of the device structures (e.g. transistors and circuitry), to the state-of-the-art machinery required to develop such devices (e.g. micro-fabrication facilities), new methods are constantly needed and then devised to handle the requirements of creating well-defined, mass-producible and affordable techniques and structures. Leading industrial firms and academic research groups are in a constant search for the next best thing, in terms of new technological breakthroughs that will push the current technology to the next step. The scope of this mass-undertaking is such, that a single group or company can barely attempt to solve all of the difficulties inherent to these new technological breakthroughs, leading to the formation of niche research attempts by many different entities, whereupon small, nearly incremental, steps are taken by each. Yet the sum of these efforts, when successfully combined, can lead to newly developed, inexpensive methods of fabricating competitive devices.

Contemporary solid-state devices were both devised and implemented using the knowledge and know-how of condensed matter physics, developed in the early to mid- 20<sup>th</sup> century. An extensive library of information regarding the chemical, crystalline order and configuration of bulk material was both researched and catalogued to an extent that nearly all essential properties of bulk materials are now well known. Of these materials, the development and usage of semi-conducting (SC) materials, particularly silicon, has until now spearheaded research in the world of electronics, sensors and micro-electro-mechanical systems (MEMS). The efficiency, affordability and expertise at handling silicon have made it the material of choice in these fields. Despite some of the apparent shortcomings of silicon when compared to other SC materials, it has remained the foremost substrate material in the field of integrated circuit (IC) technology. The usage of silicon has allowed the IC industry to follow the nearly dogmatic adherence to Moore's Law, which states an informal scaling law that the number of transistors on a chip doubles approximately every two years (see Figure 1). However, the race to double the capacity on a single chip will soon be hitting a critical size limit, where the theoretical physical models used until now will no longer be applicative – when the critical dimensions (CDs) of the essential components reaches the atomic level.

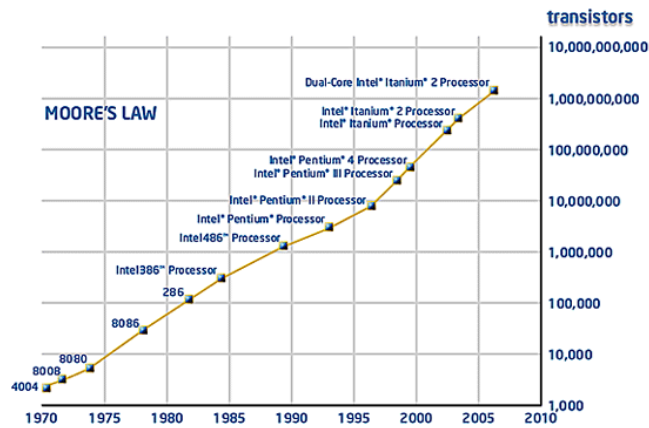


**Figure 1: Moore's Law**

The doubling of the number of transistors on a chip approximately every 24 months.  
Taken from Intel's website.

The end of the 20<sup>th</sup> century foresaw the endpoint of this high-speed development race, and a completely new methodology and mentality would be required to overcome these distinct physical boundaries if the advances in the IC realm are to continue. Thus, the field of Nano-electronics was envisioned, with the fundamental concept that the future will comprise of structures built at the nanometer scale, a billionth of a meter, with a shift of the physical laws pertaining to these structures to the molecular and atomic scale.

## 2.2 Top-Down vs. Bottom-up

Until the last few years of the 20<sup>th</sup> century, the bulk of solid-state device fabrication was limited to large scale manufacturing methods, involving colossal machinery and capital. The concept involved creating perfectly crystalline materials as a base substrate, such as slabs of crystalline silicon created using the Czochralski method. These substrates are then used as templates for all types of machining processes, in a method known as top-down machining. In this methodology, one starts with a bulk slab of material, and then uses multiple fabrication processes (such as photo-lithography, dry and wet etching, and deposition methods) that were especially designed to create large scale integration of an enormous number of identical devices, simultaneously. This process has proved itself in the IC realm, with all current devices in the market today based on these methods. Progress in enhancing and developing the processes and machinery involved has reached commercial levels of ubiquity. However, the cutting-edge techniques used by industry leaders, which have allowed companies such as Intel and AMD to achieve nanometric scaled features, are of such intricacy and cost, that they are only available in a few locations around the world. The top-down methods developed for the IC industry has pushed research expansion to such an extent that it has percolated into other fields as well, such as MEMS. This has allowed the diffusion of knowledge pertaining to mass-producible fabrication methods to a wide range of fields.

Despite the intense effort poured into improving these top-down techniques to conform to nanometric-scaled fabrication, these methods are physically limited due to a slew of reasons. For example, photo-lithography utilizes light waves to define the

CDs on a chip, which is fundamentally limited by the wavelength of the light source involved. Although a number of tricks can be used to compensate for smaller features, such as those used in the latest generation of chips, these wavelengths are usually in the hundreds of nanometer range, limiting the CDs definable.

In response to these limitations, the bottom-up approach concept was developed: Instead of starting with a bulk material and carving it down to individual device architectures, one could instead use ready-made, nanometer sized objects, to build devices from the bottom up, using these objects as fundamental building blocks. Rather than trying to narrow one's view down to the nanometer, when viewed in this respect, there is plenty of room at the nanometer scale, starting from the bottom up. This concept was originally predicted by Richard Feynman, in 1965 [1], who hypothesized creating a succession of miniaturized manipulators to handle and fabricate things at the molecular scale.

The bottom-up approach was transformed from the theoretical realm into reality in the latter part of the 20<sup>th</sup> century, with the discovery of nanometric sized materials, which could be fabricated in large quantities with nearly identical properties. These objects could then be used as building blocks for the bottom-up approach, but more importantly, as they inherently lie in the realm of nanometric scaled objects, their physical properties are completely distinct from those of bulk materials. In many examples, one of which will be expounded in the next section, the physical properties of these nanometric objects surpass those of processed bulk materials. The bottom-up approach is therefore more than just a solution to the insurmountable difficulties that plague the top-down approach at the nanometric scale, but rather open the possibilities of both an entirely new world of physics and chemistry, as well as the development of faster, cheaper and better device architectures, unattainable using the top-down approach.

While the field of nanotechnology encompasses methods employed by the top-down and bottom-up approaches, knowledge of both methods is essential since typically, an integration of the two methods is required. The bottom-up approach is advantageous for creating mass quantities of ready made nanometric objects, but top-down approaches are essential in integrating such objects in mass-producible architectures. Nevertheless, some methods utilizing the bottom-up approach try to circumvent as much of the top-down approach as possible, such as the formation of self-assembled monolayers (SAMs) to guide large numbers of molecules to specific locations. Furthermore, the handling of objects at the nanometer scale entails a complication that is not relevant to the macroscopic world: a nanometric object comes into contact with another object (of any size), the close-range forces between the two objects causes them to "stick" to each other, though their effective range is only a few single nanometers. This problem, defined by Prof. Richard E. Smalley as the "sticky finger problem" [2] poses a seemingly insurmountable obstacle for realizing some of the more fantastic molecular engineering designs, yet its implications are of double importance to the work described in this thesis.

The bottom-up approach consists of a wide array of newly discovered materials, with an even wider array of differing characteristics. The choice of material for a specific application can then be nearly custom made to fit the required specifications. In terms of electronic/solid-state device architectures, one of the most astounding



materials discovered are carbon nanotubes (CNTs), whose particulars will be described in the next section.

## 2.3 Carbon Nanotubes

CNTs were discovered over a decade ago [3-5] and are one of the allotropes of carbon, a set that includes diamond, graphite and  $C_{60}$  (fullerenes). CNTs are thus highly stable molecules of nanometric diameter, with an array of unique electrical, thermal and mechanical properties [6-9]. A brief description of the structure and properties of CNTs follows.

### 2.3.1 Carbon Nanotube Structure

CNTs can be demarcated into two distinct groups, single-walled carbon nanotubes (SWCNTs), and multi-walled carbon nanotubes (MWCNTs). The description here will begin with the former. A SWCNT can be visualized by taking a strip of graphene (i.e. a single layer of graphite), and rolling it up into a tube. The caps of these tubes are theoretically closed off by fullerene like balls. Figure 2 displays images of SWCNTs. Figure 2a displays a rendering of two nanotube sections: Each hexagon corresponds to an aromatic ring, with a carbon atom at each vertex. Figure 2b is a transmission electron microscope (TEM) image of a single nanotube, with the closed, fullerene-like tip. The length of the nanotube can range up to few millimeters [11], but the diameter of an individual SWCNT ranges from 0.7 – 5 nm [12]. A MWCNT can then simply be described as a number of nested SWCNTs, each with a diameter larger than the one within.

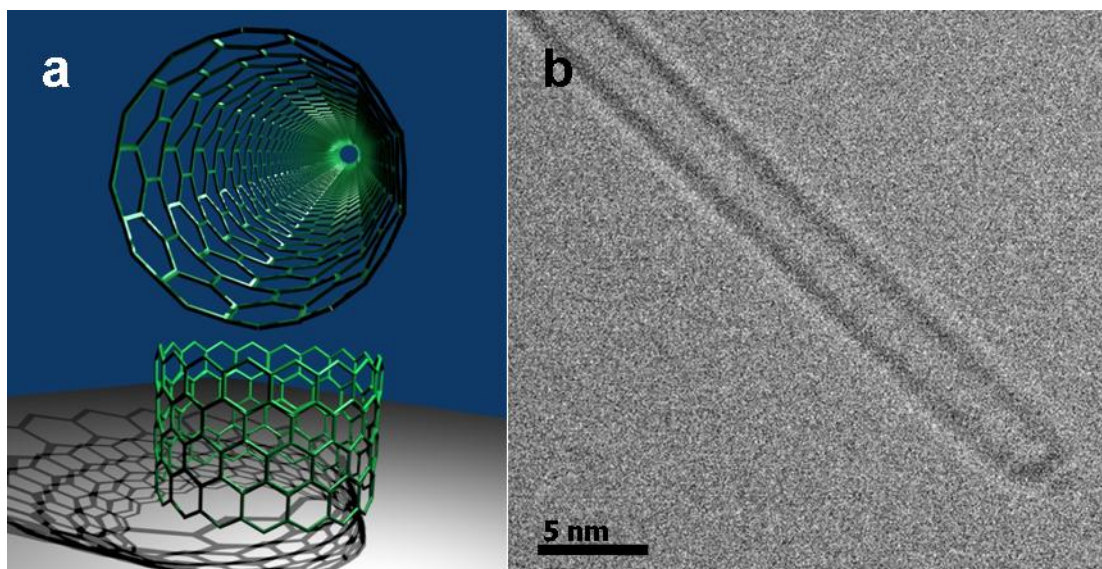


**Figure 2: Carbon Nanotube Structure**

(a) Renderings of single-walled nanotubes, showing the carbon rings. (b) A TEM image of a nanotube, including the closed fullerene-like tip.

The atomic structure of a CNT can briefly be defined by taking a sheet of graphene, dividing the aromatic rings (carbon hexagons) into a set of integers (as defined by the

unit vectors of the graphene sheet), then, cutting the sheet, and rolling it up along a specific angle known as the *chiral angle*. Figure 3a shows the allocation of sets of integers for each benzene ring. The unit vectors of the graphene layer are also defined in the image. Using this notation, the *chiral vector* of the tube, being the angle about which the graphene sheet is rolled, can be defined by the integer set (n,m) by:

$$\vec{C} = n\vec{a}_1 + m\vec{a}_2 \quad (1)$$

This chiral vector also defines the circumference of the tube, since the length of the chiral vector is simply that of the two (cut) edges of graphene layer that are connected to each other. Using this knowledge in conjunction with the length of each C-C bond ( $a_{CC}$ ) comprising the aromatic ring walls, the circumference of a SWCNT can be given by:

$$c = |\vec{C}| = \sqrt{3}a_{CC}\sqrt{n^2 + nm + m^2} \quad (2)$$

The value of the carbon-carbon length in a CNT is a bit shorter than that of a graphene: The value of the C-C length in the flat sheet of graphene is typically: 0.144 nm, however, due to the curvature of the sheet in a SWCNT, the value has been experimentally found to be reduced to 0.1421 nm [10]. A MWCNT can be described using the same notation. Each nested layer of the MWCNT's walls is a SWCNT, with a distance of ~0.344 nm between each layer. This distance is the distance between graphene layers in graphite, and has been empirically measured using TEM.

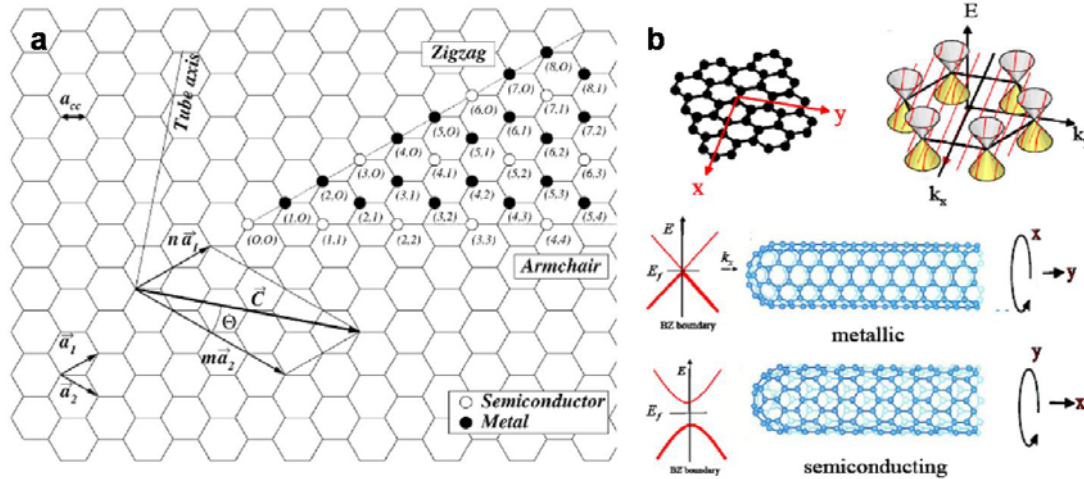


**Figure 3: Internal Structure of a single-walled nanotube**

(a) Graphic showing the correlation between the roll-up vector, and the (n,m) coordinates defining the nanotube (Ref. [10]). (b) Electronic structure of a nanotube. Different roll-up vectors (x,y) produce different line-up between the atomic locations and the first Brillouin zone (Ref. [8]).

Due to their unique structure, SWCNTs have a wide array of electrical, chemical, optical and mechanical properties. Since there are so many unique properties [13], only a very brief description of some of them will be given here.

As stated beforehand, and as listed in Figure 3a, b, the choice of indices (n,m) define not only the structural makeup of a SWCNT, but also its electrical properties. For a given set of integers (n,m), a SWCNT can range from being metallic (with a band gap of zero), to semi-conducting, with a band gap ranging from a few mV (semi-metallic) up to a little over 1 eV. The general rule defining whether a tube is semi-conducting or metallic is as follows: if the set (n,m) of integers gives the relation:

$$n-m=3\times q \quad (3)$$

with q being an integer value, then the tube is metallic. This band-gap is diameter dependant, and has been empirically evaluated giving the approximate formula:

$$E_g \cong 0.9eV / d[nm] \quad (4)$$

A SWCNT is a *one-dimensional system*: The electrons are confined to the plane of graphene, as well as the closing of the graphene sheet upon itself, which creates a ring-like quantum well (the confined axes), thus the electrons can only travel along the axis of the tube (the free axis). As such, the 1-D density of states (DOS) has what are known as *Van Hove singularities* defined by the coincidence of the possible Fermi energy with the DOS ( $\sim 1$  over the square root of the energy for a 1-D system). Therefore, as can be seen in Figure 4, there are additional energy band-gaps possible. In effect, only the innermost pairs of singularity bands contribute at room-temperatures (since the population of electrons in respect to the Fermi energy is temperature dependant). The sets of energy band singularities are given names, and are usually connoted by:  $E_{ii}$  with  $i$  being the index number of the singularity set: e.g., for the innermost band (which is usually the band gap of the SWCNT), the inner band-gap is connoted  $E_{11}$ . The matching  $ii$  is due to quantum selection rules.

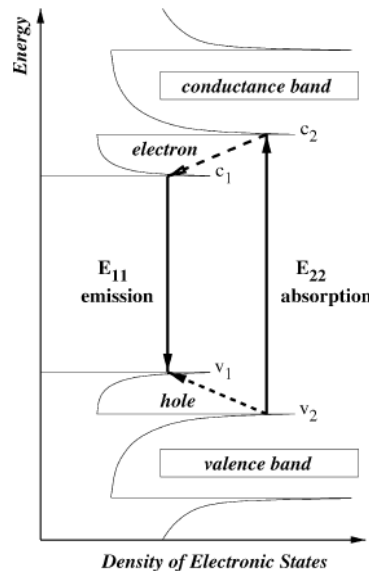


**Figure 4: Density of states of a single-walled nanotube**

The peaks in the density of states for a one-dimensional system are called Van-Hove singularities (Ref. [ 10]).

The optical properties of a SWCNT are also defined by these energy gaps [14]. A SWCNT will emit/absorb photons in the infra-red (IR) regime. This can easily be seen by plugging in an approximate energy gap of a SWCNT, and using the relation:

$$\lambda_{\text{photon}}[\mu\text{m}] = 1.24/E_{\text{gap}}[\text{eV}] \quad (5)$$

Returning to the electronic structure, the 1-D structure of CNT systems also implies that their conductance will be quantized. Therefore, a single channel system, comprising of a single SWCNT will have a total conductance of:

$$G = N(e^2/h)T \quad (6)$$

with  $T$  being the transmission co-efficient of the system, and  $N$ , the degeneracy of the system. This has been demonstrated experimentally [15]. For some purposes, we can assume a transmission of near unity, and a total degeneracy (degeneracy and number of sub-bands) of four, thereby obtaining:

$$G = 4e^2/h \quad (7)$$

Moreover, it has been both theoretically calculated and experimentally measured that SWCNTs can provide charge carrier mobilities of several orders of magnitude over currently used materials.

Due to the fully-connected carbon bonds of the CNT's outer wall, a CNT is relatively inert, in the chemical sense. Studies of adherence of particles to a CNT's walls, or of material within a CNT are based on the imperfections of the CNT walls which lead to dangling bonds, allowing particles to attach themselves to the carbon atoms. However, van der Waals forces, which are dominant in the case of CNTs (since they are in essence long chains of carbon) are difficult to measure, and complicate these analyses.

Finally, the stable structure of a CNT, with all the carbon atoms in the graphene plane being covalently bound, lends to CNTs being one of the strongest materials today. Furthermore, they are mechanically flexible, with a Young's modulus of a single SWCNT is in the order of  $\sim 1$  TPa [16]. This has lead to a massive attempt in integrating CNTs in materials sciences, as well as their integration in MEMS devices, and has even been described as a material for connecting cables to space.

### 2.3.2 Carbon Nanotube Growth

CNTs can be created today using various methods [6]. The three main modes of production are laser ablation, arc discharge, and chemical vapor deposition (CVD). In addition, there are numerous variations of these methods, such as plasma enhanced CVD (PECVD).

Laser ablation and arc discharge work according to the same principle whereupon a large pulse of energy is created on a carbon electrode that has been impregnated with metallic catalysts. Under the right conditions (catalyst density, temperature and pressure), the discharge/laser pulse will cause carbon particles to evaporate off the

electrode, and self-assemble into CNTs. These CNTs must then be collected on a cold finger, and purified using a medley of chemical solutions. While the laser ablation method can produce CNTs of nearly the same diameter, it is not easily integrated in IC compatible processes.

The CVD growth of CNTs allows the nanotubes to be grown directly onto a substrate, permitting their patterning and/or alignment. It must be noted, however, that the high temperatures required during the growth of CNTs prohibits the use of many materials as substrates, depending on their melting point. Such is the case for many thin-film metals (whose melting point is lower than that of their bulk counterpart), as well as the inclusion of IC chips (since at high temperatures, the implanted regions diffuse into each other). Nevertheless, the CVD method is the most promising for integration with IC compatible technology due to the relative control one has over aligning and distributing the nanotubes on a surface, as will be described in the next chapter. Additional information and details regarding the CVD process will be dealt with in a later chapter, with the other growth methods not listed in detail, due to their limited relevance to the objectives of this thesis.

The distinction between each type of CNT growth described is most apparent when it comes to integrating them into device architectures. CVD growth theoretically allows one to pre-design and orientate CNTs directly onto a surface, with no further complications, as long as the surface is able to withstand the CVD process itself. In contrast, the laser ablation and arc-discharge methods require one to collect the manufactured CNTs in a separate receptacle, purify the nanotubes, and then develop a method of dispersing the CNTs on a surface. This last step can further introduce impurities that can stick to the nanotubes, as well as requiring a great deal of expertise in preventing individual SWCNTs from bunching up into bundles. The bottom line, however, is that regardless of the method employed, the production of CNTs on a large scale has become both technologically standardized, and therefore relatively simple.

## **2.4 Carbon Nanotubes and Nanocircuitry**

CNTs were one of the first molecules to be designated as building blocks for the field of nanotechnology. Since their discovery, they have already been integrated in a multitude of different devices and materials. Therefore, while the field of nanotechnological devices, with an emphasis on bottom-up design, includes a plethora of different methods and materials, the subset of devices based only on CNTs holds its own ground in terms of technological prowess and ambition. As a result, when the editors of *Science* magazine decided to name the field of "nanocircuits" as their *Breakthrough of the Year*, in 2001 [17], it was carbon nanotubes that they designated as the forerunning technology that would spearhead future developments, and as depicted on their cover art (presented in Figure 5).

The basis for the claim that CNTs will lead the forefront of progress in terms of nanocircuitry is that they had already been shown to be suitable as nanoelectronic devices, as will be described in the next section. Proof-of-concept CNT devices have been designed and demonstrated for a host of different purposes. Moreover, of all the elements useable as building blocks for nanotechnological devices, CNTs provide

some of the most unique and robust properties, compared to almost any other material in the field of molecular engineering.



**Figure 5: Cover of Science, December 2001**

Cover art depicting nanocircuits which consist of well ordered carbon nanotubes.

The major issue remaining is that of *engineering*. To produce a single device that utilizes a certain property of a CNT is one thing, especially one that requires an inordinate amount of fabrication processes. However, to produce actual devices, with an emphasis on the plural form, is quite another. As much effort has been poured into creating proof-of-concept devices as there has been in developing methods of batch processing that would integrate CNTs into actual devices. The major complication is one that affects the *entire* field of nanotechnology, namely: How to assemble all these building blocks in a deterministic method?

Controlling the placement and orientation of these building blocks in a fully integrative method that would allow one to fully utilize the specific properties of each individual molecular element has been one of the Holy-Grails of nanotechnology. This issue lays at the core of this thesis: The creation of a method to utilize individual SWCNTs arranged in a predetermined array.

### 3 Literature Review:

The following section will summarize some of the existing work in the field. The field of CNTs has become one of the more saturated ones in the overall field of nanotechnology. As a result, a short summary such as this will only touch upon a mere sampling of the volume of existing research in the field. For other references, one can turn to references [6,10]. This chapter will be divided into sections ranging from some of the more general applicative and experimental research done on carbon nanotubes, to more specific work that has direct implications regarding the work done in this thesis. The review will begin with nanotube characterization, followed by a short review of some SWCNT-based devices. Following that is a section describing some of the contemporary methods of controlling the placement of nanotubes, and then a section on the growth of nanotubes between micro-fabricated pillars.

#### 3.1 *SWCNT Characterization*

When working with SWCNTs, the first thing to realize is that, being nanoscaled objects, they are only visible to the eye. This being the case, numerous microscopic and spectroscopic methods are employed to view and characterize nanotubes. A brief description regarding each of the characterization methods used is essential before further delving into the research on CNTs since, like all work at the nanoscale, the characterization and implementation are so closely intertwined. As will be described later, some of the microscopic methods can act as an active source of information, and are not merely passive instruments. The characterization of CNTs is a fundamental part of this work, yet as there are currently an abundance of such techniques [10], only those methods used in this research will be described. Furthermore, a detailed description of each method, including a brief physical description of the working process, will be described in the Experimental section of this thesis.

The main microscopy devices used to analyze SWCNTs include transmission electron microscopy (TEM), scanning electron microscopy (SEM), atomic force microscopy (AFM) and scanning tunneling microscopy (STM). The first two (TEM and SEM) were used in the work appearing in this thesis. AFM and STM (and their similar ilk) were not used, for a specific reason that will be described presently. Each form of nanometric imaging has its advantages and disadvantages, as well as the fact that each one of the four aforementioned techniques relates to different scales of imaging. For example, the STM has sub-nanometric resolution, as does the TEM (Figure 6), yet to scan samples at that resolution limits amount that can be scanned simultaneously. An AFM can scan large areas with nanometric precision, yet scanning a  $10 \times 10 \mu\text{m}$  area takes quite a while. The SEM can give the greatest spatial scanning dimensions in the most time-efficient way.



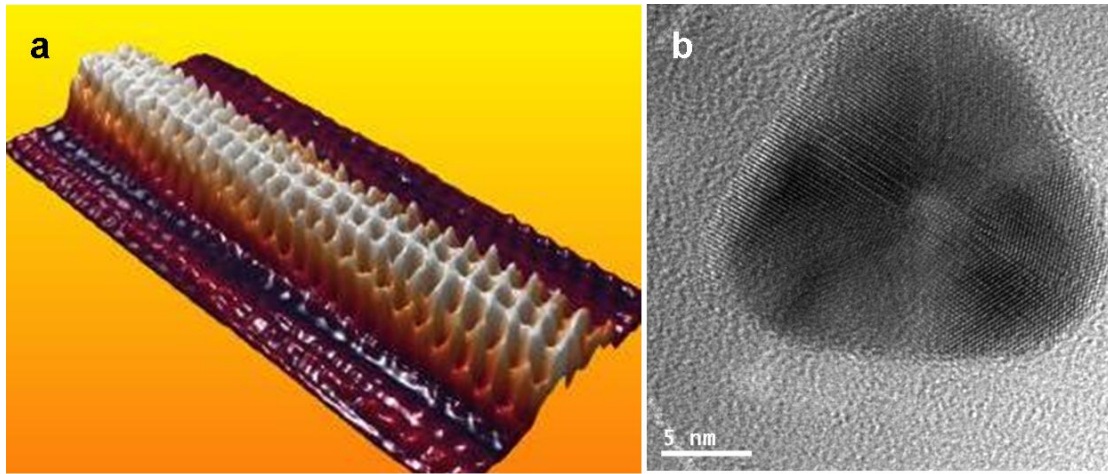


**Figure 6: STM and TEM images**

(a) An STM image of a nanotube taken from Omicron's website (Omicron is a leading STM manufacturer). (b) A pyramidal gold nanoparticle viewed with a TEM, the individual atoms can be seen in the bottom right.

### 3.1.1 TEM Analysis

The TEM is the instrument that was initially used in the discovery of CNTs [3,5] (Figure 7a). Samples with CNTs are easily inspected once they are placed on a suitable TEM grid. Typically, the CNTs are grown, by whichever means, and then transferred onto the TEM viewing grid. TEM grids are typically small, thin discs consisting of copper (~3 mm in diameter, ~0.1 mm thick), with a mesh of copper wires holding a thin layer of amorphous carbon, onto which samples are dispensed. To view CNTs, one must first transfer the CNTs into a solution, then dispense the solution onto the grid, and wait for it to dry. With CNTs, there is little to no control over the density of the nanotubes, or the prevention of aggregates and bundles from forming. Nevertheless, the TEM is the primary tool for viewing CNTs after their preparation, since the amount of time from growth to viewing, using the TEM, can be implemented in a considerably short amount of time (ranging in a few hours).



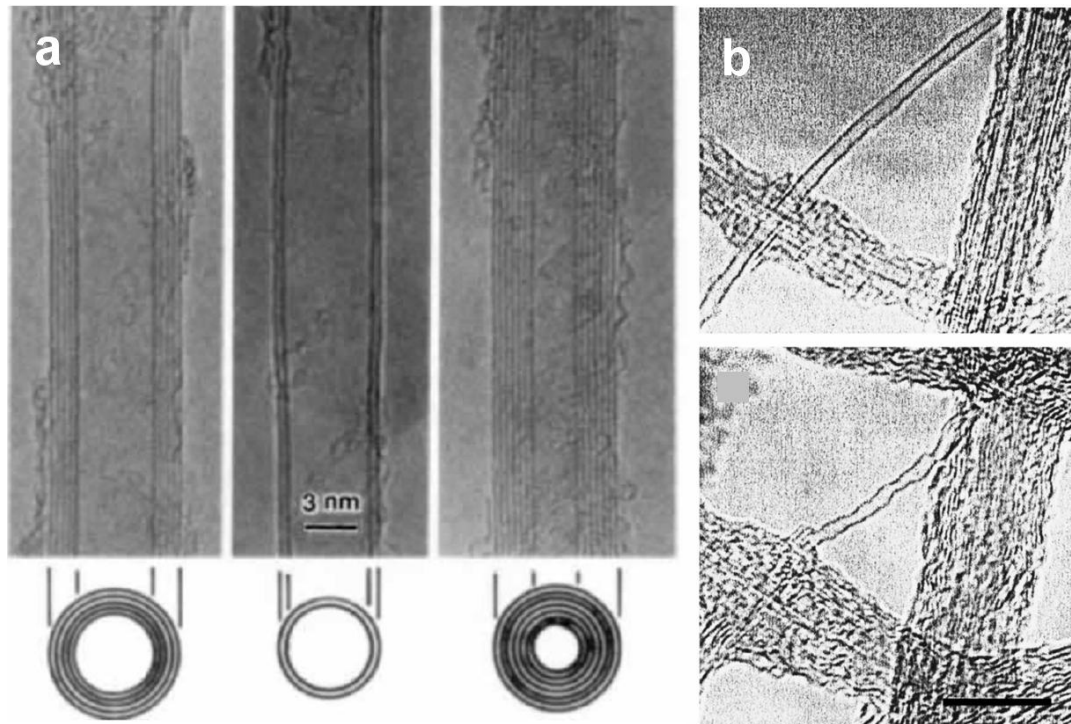


**Figure 7: TEM images of nanotubes**

(a) The first images of single and multi-walled nanotubes (Ref. [4]). (b) Effects of irradiation of the TEM electron beam on a single-walled nanotube (Ref. [24]).

TEM analysis also enables one to quickly view the internal structure of a CNT. A short period after being discovered, CNTs were shown to be capable as acting as vesicles for other materials [18]. These other materials can be added either after growth, or even during their growth, and include metals, metallic salts, and even fullerenes [19-21]. The TEM is essential in order to view the inner structure of these filling materials [22].

Analysis of CNTs with a TEM is in no way completely passive: When viewing a single SWCNT over a hole, with no background carbon film, the TEM electron beam itself can harm the atomic structure of the tube by way of “knocking off” some of the carbon atoms [23], causing the destruction of the nanotube structure (see Figure 7b). This limitation is especially poignant the longer you view a SWCNT in the TEM, and can cause their complete destruction after merely a few minutes of viewing. It was found, however, that keeping the electron beam acceleration voltage below 86kV prevents the knocking off of carbon atoms [24].

TEM analysis of CNTs can thus be summarized as one of the most ubiquitous methods of analyzing CNTs on the fine scale, in the most time-efficient manner. However, it is generally limited to analyzing CNTs *only* on a TEM grid, and the analysis of CNTs on any other type of structure is severely restricted.

### 3.1.2 AFM Analysis

For CNTs lying upon a substrate, TEM analysis is inadequate, as the surface must be “transparent” to the electron beams, therefore, viewing CNTs with an AFM was the first method approached to view CNTs on a surface [25]. The AFM allowed reasonably large viewing areas to be scanned, albeit with the price of long periods of time per scan. When viewing a CNT on a surface, it was quickly determined that they would deform when in contact with the surface, due to the van der Waals interaction between the tube walls, and the surface [25,26]. Even twisted nanotubes on a surface were measured using the AFM [27].

Using the AFM was found to be quite useful in mapping out the locations of CNTs on a surface for further analysis, or, more importantly, for locating specific tubes for device integration. For this purpose, a substrate is marked with (typically metallic) alignment marks, and then scanned using an AFM. Individual CNTs can then be identified by the coordinate system defined by the alignment marks. Furthermore, devices can then be built on these specific nanotubes using e-beam lithography (as will be described below).

Yet another useful engineering aspect of AFM analysis of CNTs, other than their structural analysis and mapping on a surface, was found to be that of actively using the tip of the AFM to drag a CNT to a specific location and orientation [28,29]. The AFM tip can manually pull and twist a CNT such that it can be completely isolated from other tubes (Figure 8). This is crucial for device fabrication, as one requires that a single SWCNT device would consist solely of a single, individually isolated SWCNT.

Using the AFM, one can then not only map a large number of SWCNTs on a substrate, but one can furthermore isolate individual SWCNTs for device fabrication. This use of an AFM for both imaging and manipulation purposes was the first real attempt at creating a method for individual SWCNT device fabrication. However, the major limitation of AFM usage, for both mapping and manipulation, is that it is an extremely tedious task, requiring many hours of painstaking work for each nanotube that is to be isolated and mapped. This severely hampers the use of this method in terms of mass production.

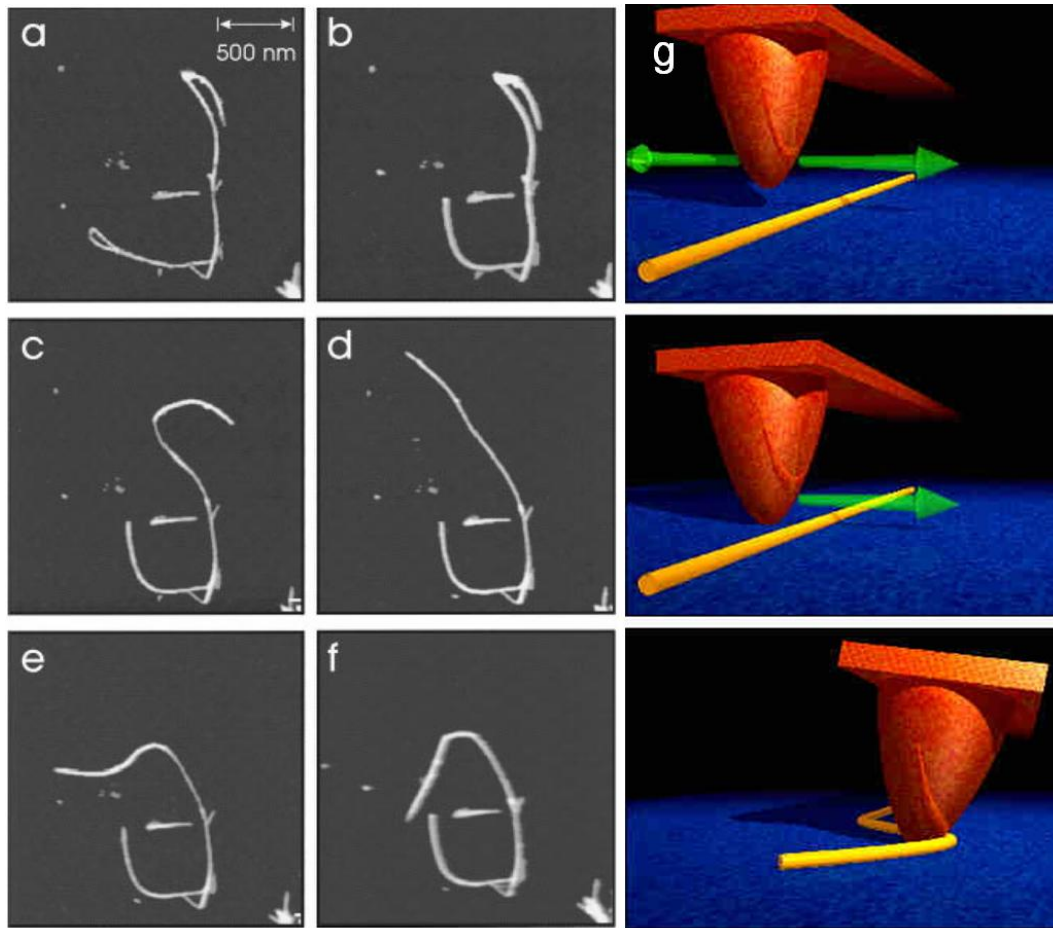


**Figure 8: AFM manipulation of a nanotube**

These images (a-g) demonstrate the manipulation of a single-walled nanotube, by an AFM tip, to create the Greek letter theta (Ref. [29]). Image (g) is from IBM Research's website, describing this work.

### 3.1.3 SEM Analysis

It took over ten years from their discovery until individual SWCNTs were viewed using the SEM. The SEM is most valuable in *device* microscopy since the viewing capabilities of a SEM range from a few hundred nanometers, to several hundred millimeters, as well as the SEM's ease of use and sample preparation. In fact, other than the constraint that the sample be conducting (a limitation that is irrelevant for AFM studies), there is nearly no sample preparation involved. This means that an entire device can be analyzed with a SEM. However, in order for a nanometer scaled nanotube to be viewed in a SEM, the type of SEM that must be used is the high-resolution variant (HRSEM), which operates at lower working voltages (as will be described later). It was found that viewing SWCNTs on silicon dioxide surfaces was possible only when working at approximately 1 kV [30], over which the SWCNTs become "transparent" to the detector, and are engulfed as part of the surface signal. This form of rapid imaging of large areas using the HRSEM has become the dominant method of viewing SWCNTs on a surface. Furthermore, it has been integrated with the aforementioned mapping technique, whereby the HRSEM is used to map the locations of individual SWCNTs. The devices with the SWCNTs can then be viewed with the HRSEM, in a very short amount of time, as in Figure 9.

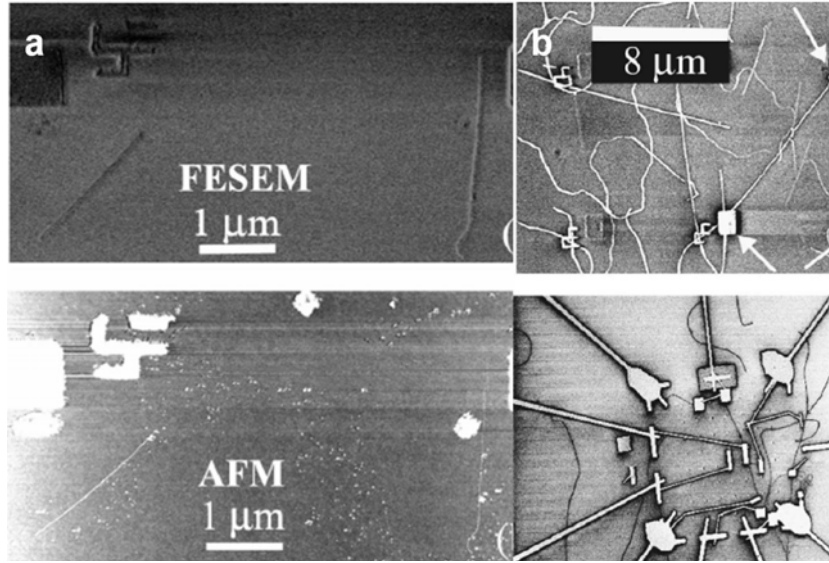


**Figure 9: HRSEM imaging of nanotubes**

- (a) The comparison of HRSEM (or, field emission SEM) to AFM. The top image can be taken within minutes, whereas the bottom one takes hours. (b) SWCNT devices fabricated using HRSEM mapping, with the HRSEM images displaying both the nanotubes, as well as the electrodes. Both images from Ref. [30].

Using HRSEM imaging, one can image SWCNTs on a variety of three-dimensional substrates, at low magnification. However, other than providing a visual scan of a sample, HRSEM imaging is limited in its structural information capabilities. This type of information is best attained through spectroscopic methods.

### 3.1.4 Carbon Nanotube Spectroscopy

Spectroscopic methods are ideal for probing specific properties of materials. In terms of carbon nanotubes, there are a number of compliant spectroscopic methods [10]. One of the most useful spectroscopic methods for SWCNT probing, as well as being one of the methods used in this work, is that of Raman spectroscopy (RS). RS is a method of analyzing the vibrational modes of a molecule, which imparts important structural information regarding its chemical bonds. A description of the mechanism involved will be detailed later, in the Experimental section (as well as in Appendix 1). RS analysis of CNTs has become nearly standardized by numerous studies [31-32], which have managed to correlatively ascribe the spectroscopic Raman signal to the exact structure of the SWCNT; specifically, a correlation between the peaks appearing in a RS signal and the (n,m) set of the SWCNT in question. Formulas relating the diameter of a SWCNT to that of the location of a specific peak have been empirically found to be of the type:

$$\omega = \frac{A}{d^n} + B \quad (8)$$

with  $\omega$  being the frequency of the peak in the RS signal,  $d$  the diameter of the SWCNT,  $n$  an empirical exponent and  $A$ ,  $B$  empirical constants. An example of a RS signal is presented in Figure 10a, with each peak in the spectrum given a specific

name. The reviews in references [32] and [33] provide a detailed description of the RS spectrum of an individual SWCNT, and a short explanation will appear in a later section. Furthermore, a few of the tables appearing in those references appear in Appendix 1. Figure 10b displays some of the parameters that can be used to correlate between a measured RS spectrum, and a specific SWCNT. Not only can the diameter of the SWCNT be known, but also its chirality and (n,m) values. A table listing some of the (n,m) nanotubes and their respective peak locations is supplied in Appendix 1.

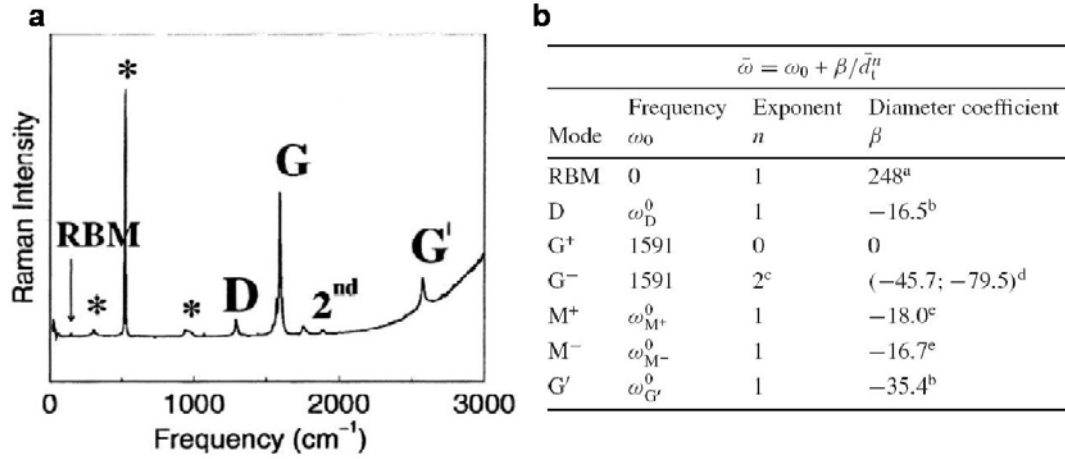


**Figure 10: Raman Spectroscopy of Carbon Nanotubes**

(a) A typical Raman signal from a SWCNT on a silicon dioxide surface. Each peak in the spectrum is given a name, such as RBM, D and G. The asterisks denote peaks resulting from the substrate. (b) A table correlating the shifts in the spectrum and the structure of the nanotube, using an empirical relation. Both images are from Ref. [33].

Further utilization of the RS spectral information can be realized by *spatially* mapping the peaks of the RS signal. To do this, one can define each pixel of an area to be scanned to portray information regarding a specific peak only. For example, one can define that the “brightness” of a pixel is in direct correlation to the intensity of the G spectral band of a RS spectrum, and then spatially raster a sample [34]. This enables RS-information supplied imaging, and example of which is in Figure 11a. Furthermore, it was found that the Raman signal is substantially increased when the SWCNT is suspended [35], and as can be seen in Figure 11a, where the suspended segment is much brighter than the non-suspended part. As a final point, the intensity of the peaks was also found to be directly linked to the metallic or SC properties of the SWCNT.

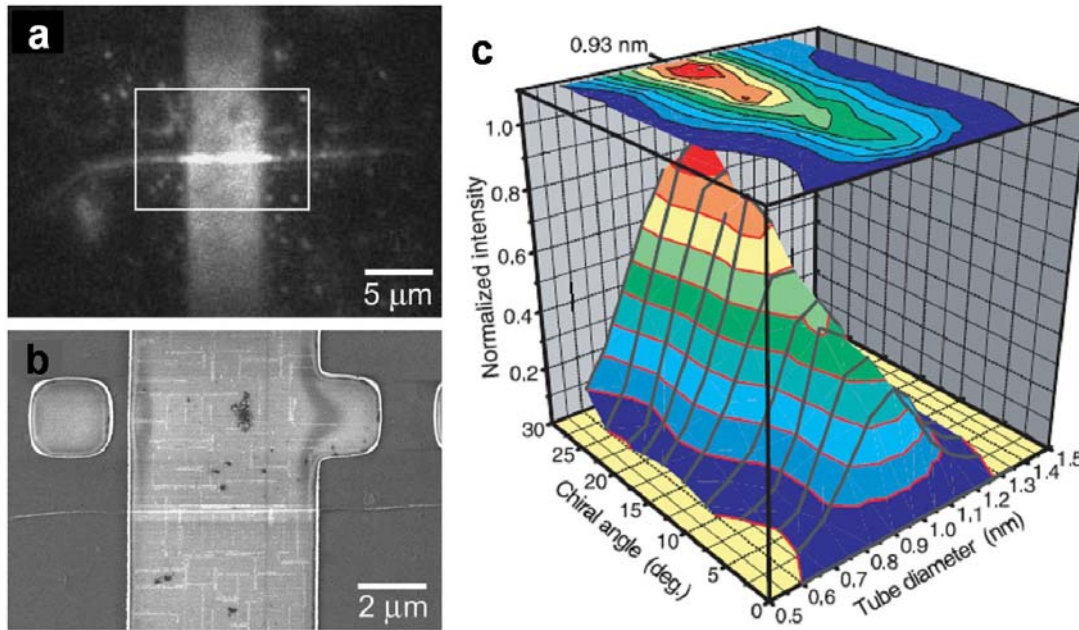


**Figure 11: Global Raman Mapping and Fluorescence of Nanotubes**

(a) A Raman spectroscopy produced mapping of a suspended nanotube. The bright section in the center was created by focusing on the G-band of the nanotube. (b) An HRSEM image of the same nanotube in (a). Both images from Ref. [34]. (c) Structural assignment of SWCNTs by fluorescence spectroscopy (Ref [14]).

In addition to RS for analyzing SWCNTs, there are a number of other methods for ascertaining the structural makeup of a single nanotube. Among these are a number of photo-based methods, such as fluorescence [14] and photo-luminescence [36], as well as STM imaging. These methods can also provide information regarding the electronic properties of a SWCNT, as can be seen in Figure 11c, where information from RS and fluorescence was combined to obtain a graph correlating the fluorescent signal to the SWCNT structure. More similar to the method of RS is that of Rayleigh spectroscopy. In Rayleigh spectroscopy, structural information can also be garnered, in much the same way that RS information is [37]. The Rayleigh signal is even more sensitive to the background noise, due to the intensity of the central laser peak (creating the signal) of the Rayleigh spectrum. Therefore, while RS could be used to detect SWCNTs suspended over small, shallow trenches in a substrate, Rayleigh spectroscopy is limited to SWCNTs grown over deep trenches, usually ones that were cut through the entire thickness of the substrate, in order to minimize substrate signal reflection.

### 3.2 SWCNT Devices

Devices based on SWCNTs are the prime motivator for the abundant research on CNT's properties. Specifically, the ability to create both metallic and SC nanotubes, with an emphasis on the large range of band-gaps possible with the varying diameter nanotubes, is of crucial importance in the field of nanoelectronics and nanocircuitry. While there is, as of yet, no single method of generating nanotubes of a given type, researchers have proven that SWCNTs can provide the next-best-thing in terms of device size and capabilities. The two major fields that can be delineated in terms of

SWCNT nanoelectronics are actual transistors for replacing current transistor technology, and that of nanoelectronic sensors utilizing a CNT based field effect transistor (CNTFET) at its core. The two technologies are currently interwoven, with the current push for sensors based on CNTFETs. Furthermore, the time frames for both technologies are reasonably different, with the conceptual replacement of current transistor technologies, notably metal oxide silicon FETs (MOSFETs), using CNTs a long way off, when compared to the current possibilities of much smaller, simpler CNT based devices.

### 3.2.1 CNT Transistors and Nanowires

To prove that CNTs are realistically capable of enhancing current technology, it was first necessary to prove that some of the claims made by theoreticians regarding the unique properties of CNTs would hold. The first major technological breakthrough was made when it was proven that CNTs truly act as one-dimensional quantum wires [38]. An AFM image of that device, showing a SWCNT deposited over metallic electrodes is shown in Figure 12d. It was shown that, at low temperatures, a single SWCNT displays a discrete change in current as a function of the bias voltage, as displayed in Figure 12a, due to quantum Coulomb charging of the nanotube. Furthermore, the current was found to be a function of the gate voltage, supplied from below the SWCNT, so that current would flow only discrete, periodic, intervals of gating voltages, as shown in Figure 12b. This proved that the charge transfer through the nanotube was influenced by coulomb blockades, with electrons passing from the electrodes to the SWCNT only when the discrete energy level of the SWCNT lined up with the Fermi level of the electrodes, as in Figure 12c. The discrete levels are at a periodic distance of  $\Delta E$ , with the energy spacing equal to that of a one-dimensional quantum well, i.e:

$$\Delta E = \hbar v_f / 2L \quad (9)$$

With  $\hbar$  being Planck's constant,  $L$  the length of the quantum well, and  $v_f$  as the Fermi velocity, which was found to be approximately  $8.1 \times 10^5$  m/sec.



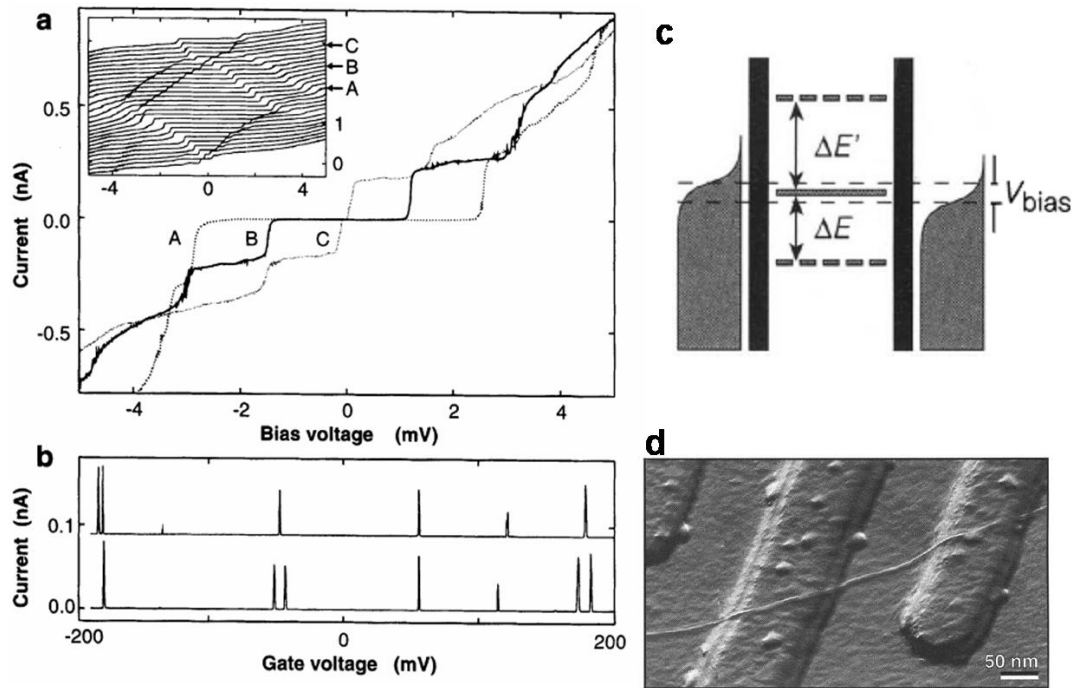


**Figure 12: Single Walled Nanotubes as Quantum Wires**

(a) Step-like current in a nanotube due to the energy blockade caused by Coulomb charging. (b) Discrete and periodic peaks of current, as a function of the gate voltage, signifying a Coulomb blockade. (c) A schematic of the band diagram of the system, displaying the discrete energy levels of the SWCNT. (d) AFM image of the device.

All images from Ref. [38].

Having shown the capabilities of the one-dimensional quantum wire, the next step was to prove that SWCNTs can act as FETs. In 1998, two papers showed that a single SWCNT would act like a p-type transistor, at room temperature [39,40]. The reason that it acts like a p-type transistor is still somewhat controversial. It is widely accepted that the p-type characteristic is a function of the Fermi pinning of the nanotube to the electrodes, and thus a function of the electrodes themselves [41]. However, by “doping” the nanotubes, one can also obtain n-type transistors. As a result, shortly thereafter it was shown that one can create a complementary MOS (CMOS) device [42], which is the backbone of the IC industry. By annealing a CNT in vacuum, it was found that the CNTs were transformed to “n-type” transistors, thereby creating an *ambipolar* device, wherein both electrons and holes are injected into the device. To do this, a procedure to passivate, or cover, part of the device was needed, so that one side remained p-type, while the other became n-type, during a vacuum annealing process (Figure 13a). Using this technology, more complicated device architectures can be envisioned. Figure 13c displays a ring-oscillator created on a single SWCNT [43]. The device encompasses many parallel complementary CNTFETs. Creating this type of device may seem extremely tedious and complicated, yet the technology used to create it is relatively mainstream, consisting of high-resolution e-beam lithography and other micro-fabrication techniques. It is important to note that the major problem in building these devices is in the placement and isolation of the single SWCNT, as will be discussed below.



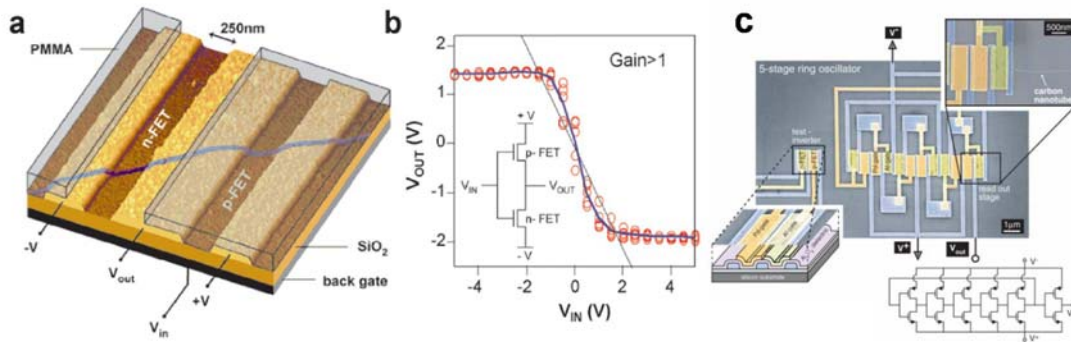


**Figure 13: The IBM Nanotube Complementary Transistors**

(a) A nanotube complementary transistor, with both p- and n-type segments. The n-type transistor was annealed in vacuum, with the p-type segment protected by a layer of photo-resist. (b) The device in (a) acting as an inverter. Both images from Ref. [42]. (c) A complicated ring-oscillator created using a number of parallel complementary nanotube transistors (Ref. [43]).

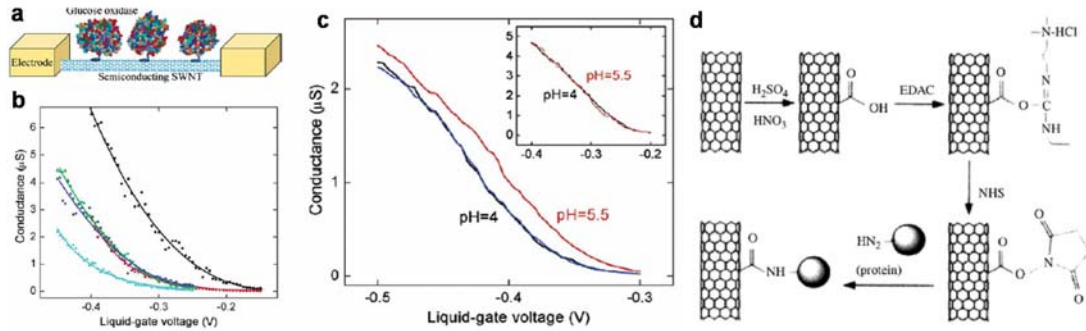
Transistors based on CNTs have become well adapted to many uses, and their characteristics have become well examined. SWCNT transistor physics exist in published reviews [44,45], and their properties have been rigorously tested, such as mobility through the CNTFET [46] and four-point probing of a SWCNT [47]. Perhaps the most important characteristics of all CNTFET properties, and the ones that hold the most promise in terms of the IC industry, are the high mobility of the CNTFETs, and their *ballistic* charge transfer [48]. If a CNTFET is created using a single, pristine SWCNT as its channel, the mobility of such a device has been shown to exceed  $10,000 \text{ cm}^2/\text{V s}$ . This value by far exceeds the current values attained using silicon technology. Moreover, since the carriers are ballistic within a nanotube, the frequency at which the CNTFET can operate should be extremely high. 50 GHz mixers using top-gated CNTFETs have been produced [49], proving that the CNTs capabilities are far beyond those of current IC technology. The integration of CNTs in MOSFET technology is probably a few years down the road [50], but the rush of research towards their full-scale integration is still at its peak. A detailed summary of some of the important formulas for CNTFETs can be found in Appendix 2.

### 3.2.2 SWCNT Sensors

Beyond the realm of CNTFETs acting merely as transistors, lays their potential use as sensors. Many different sensor applications have already been proven using SWCNTs [51]. They range from chemical, mechanical motion and flow sensing. The two major concepts used for most applications today consist of either CNTFETs acting as the sensor element, or of suspended nanotube based devices.

The concept of the CNTFET sensor is simple: Since the SWCNT is a one-dimensional channel, any chemical/physical disturbance to the outer plane of graphene will immediately influence the carriers within the nanotube. Therefore, by merely being in the presence of other molecules, the conductance of the channel should be affected. This was first discovered to be the case with gasses, and the use of a single SWCNT CNTFET as a toxic gas detector [52]. Since then, numerous other methods [53,54] have been used for detecting chemicals, such as the pH level, as well

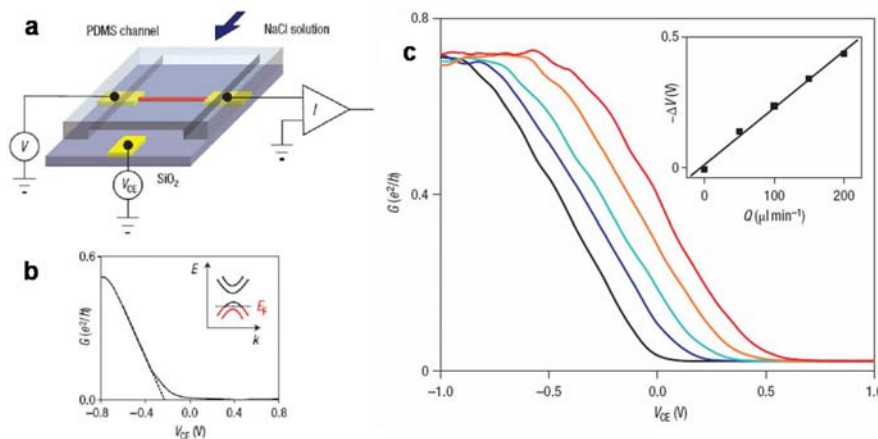
as more specialized detection, whereby a specific molecule is made to attach to the SWCNT, which can then bind to another molecule. Figure 14a presents a typical schematic of such a device that was used to detect both proteins (Figure 14b) and pH levels (Figure 14c). Using such functionalization methods, protein and DNA detection using CNTFETs have been devised [55] with CNTs covered with specific molecules that bind to the CNT on the one side, and the protein to the other (as in Figure 14d).



**Figure 14: Nanotube Based Sensors**

(a) A schematic of a nanotube based sensor, with a CNT between two electrodes, and a functionalization protein adhering to the nanotube. (b) The detection of proteins on the device by influencing the conductance of the channel. (c) Detection of pH using a nanotube sensor. All three images from [53]. (d) Schematic representation of the functionalization of a nanotube's wall by a specific molecule (Ref. [55]).

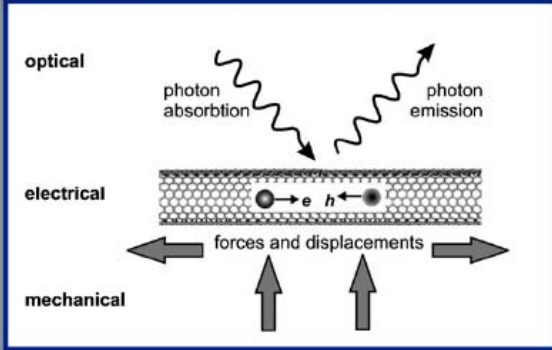
Other than these chemical sensors, CNTs have been shown to work as flow sensors as well. CNT based flow sensors would be ideal in MEMS based microfluidic channels, where one of the key issues involves knowing what the flow rate is in these miniscule channels. The first work done in this field showed that when a liquid flow was placed through a large bunch of CNTs, a voltage was detected via two electrodes on either side [56]. However, a more interesting device was recently reported, with a single SWCNT CNTFET used as a flow detector [57]. In this device, displayed in Figure 15, the actual ionic flow over the SWCNT caused a change in its conductance, thereby enabling the detection of the flow rate, as shown in Figure 15c.



**Figure 15: Nanotube Flow Sensor**

(a) Schematic of a nanotube transistor within a fluidic channel. (b) Conductance of the device before introduction of a flowing medium. (c) Change in conductance as a function of different flow rates. Images from Ref. [57].

There are many other forms of CNT based sensors, especially in the field of nano electro mechanical systems (NEMS) and MEMS [58], as well as in optics. Reference [59] well summarizes the existing work in the field of integrating nanotubes in NEMS devices. The image in Figure 16 is taken directly from Ref. [59], with many of the possibilities listed in a tabular form.

| <div> <div>OUTPUT signal →</div> <div>INPUT signal ↓</div> </div> |  | electrical   | mechanical   | optical   |
|---|--|--|--|---|
| electrical  |  | shifting of fermi level; e.g. [23]<br>single-walled carbon nanotube field effect transistors [36,37]   | piezo effect [38]<br>nanorelays [13,39]<br>nanotweezers [40]<br>artificial muscles [41]<br>cnt based rotor [28,42]<br>mechanical memory cells [28] | photon emission [43]<br>localized infrared emission [43]<br>bright infrared emission from induced excitons [44] |
| mechanical  |  | piezoresistive effect [45]<br>band-gap opening [46,47]<br>field assisted tunneling [48]<br>pressure sensor [14,35]<br>force sensors [49]<br>displacement sensors [50]<br>mass sensors [15]<br>tunneling assisted electron shuttle [51] |   |   |
| optical   |  | photon absorption<br>nanotube optoelectronics [52]<br>infrared sensor [53]   |  |   |

**Figure 16: Nanotubes in NEMS**

Table summarizing the possibilities of integrating nanotubes in NEMS devices. References listed are those from Ref. [59].

A final device of particular bearing to this work to be described is that of infra-red (IR) CNT devices [60]. The principal investigators of these IR related devices are at IBM Research, and nearly all the referenced sources on this matter come from this group. Since it was shown that CNTFETs are ambipolar, using particular sets of electrodes, or different relative voltages between the gate, source and drain, one can obtain the simultaneous injection of both holes and electrons into a SWCNT, from either end [61]. This means that a CNTFET can either be used as a detector of IR photons – where incoming light generates an electron-hole pair, which are then “detected” as a change in current in the CNTFET (Figure 17a); or as an IR source, where both electrons and holes are injected simultaneously into the CNT, and their recombination creates an IR photon (Figure 17b). These types of device prototypes have been developed, and IR sources from single SWCNTs, such as in Figure 17c, have been fabricated. Further developments in this field have produced even better IR sources [62]: For example, it was found that when a SWCNT is placed over a trench, and then electrodes are attached to it, an even brighter IR signal is achieved through the avalanche-like generation of excitons in the suspended SWCNT segment (Figure 17d). A final interesting phenomenon that was discovered regarding these devices is that in ambipolar device architectures where the injection of holes and electrons is dependant upon the relative voltage between drain-gate and source-gate, one can change the gate voltage such that the electrons/holes are accelerated at different rates, thereby changing the location of recombination [63]. This gate-dependant

recombination localization is displayed in Figure 17e, where each number is associated with a different gate voltage, shifting the location of the IR emission.

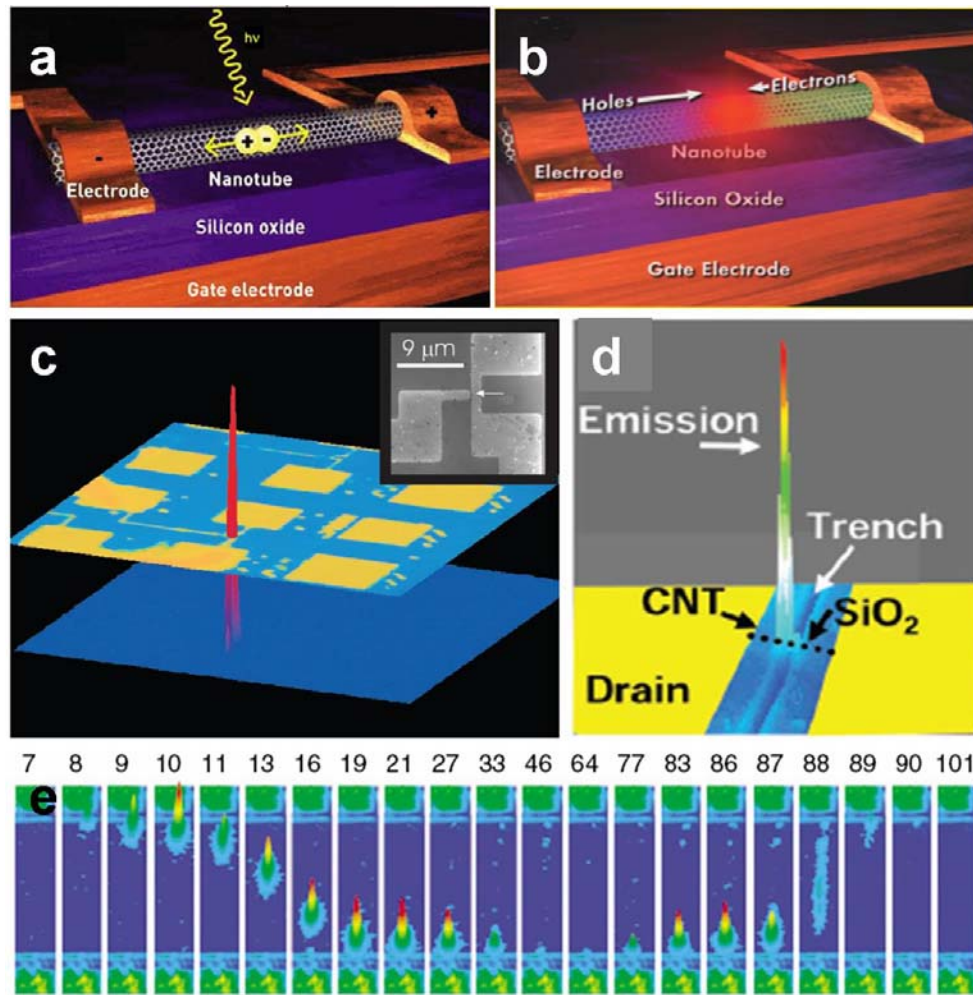


**Figure 17: Infra-red Nanotube Photonics**

(a) Absorption of a photon in a nanotube generates an electron hole pair, each moving toward different contacts, as defined by the bias voltage (field). (b) Emission of a photon, created by the simultaneous injection of both electrons and holes into the nanotube. Both images from IBM Research. (c) Actual emission of IR light from a SWCNT CNTFET (Ref. [61]). (d) Ultra bright emission of IR light from a SWCNT located over a trench in silicon dioxide (Ref. [62]). (e) Moveable emission location as a function of different gate voltages (Ref. [63]).

These IR detectors and emitters may provide a basis for more advanced display units or detection systems that can work with less expended energy, due to the nanoscale building blocks used. This advantage of lower energy use, as well as lower heat expenditure, is yet another of the many advantages attainable using nanotechnology based architectures.



### 3.3 Nanotube Placement

Despite the abundance of devices mentioned in the previous section, the main obstacle remaining between the full integration of CNTs in devices and in mass productive methods is that there is little to no control over their placement. As stated earlier, and as will be elaborated later, this is an easily definable task: presenting a reproducible method that will put nanotubes exactly where one wants them, including their orientation and location. For the last ten years, many attempts have been made at CNT controlled placement, some of which will be described here.

#### 3.3.1 Nanotemplates

When dealing with nanotubes created by arc discharge or laser ablation, the most common way of trying to position the produced nanotubes is to simply pour the solution onto a surface. Of course, this means that all the nanotubes are then randomly orientated and positioned. A method of avoiding this challenge is to modify the surfaces with a nanotemplate beforehand, usually using a SAM that has an affinity towards nanotubes. Moreover, the nanotubes can be coated with a material that has an affinity towards the SAM, producing the same result. Figure 18 presents some of the work done in this field [64-66]. Using this method, some positive results have been achieved, yet the major complication involved with this method is the need for creating nanometer sized CDs for the deposition of the SAMs. This somewhat tautological circumstance is a limiting factor for this technology. When the templates were created to be sub-micron in size, as in Ref. [66], the nanotubes were found to completely conform to the SAM, even forcing some of the nanotubes to create rings, as in Figure 18d. Yet, when the template's thickness were much larger than the SWCNTs, as in Figure 18c, then the orientations of the SWCNTs on the template itself are completely random, and the straightness of the SWCNTs is affected.

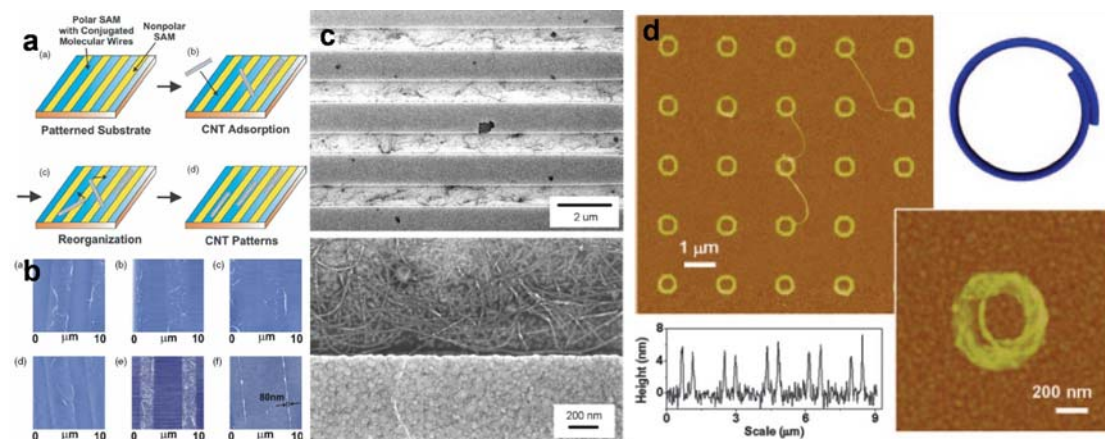


**Figure 18: Nanotemplates for Nanotube Deposition**

- (a) Conceptual schematic of the nanotemplate method. Affinity layers are patterned, after which the nanotubes are dispensed onto them, and orientating themselves according to the template. (b) Results using such a method, with templates ranging in the tens of nanometers in thickness. Both images from Ref. [64]. (c) Another result of nanotemplates for nanotube assembly, showing the lack of control on the template itself (Ref. [65]). (d) Nanotubes conforming to sub-micron sized SAMs, even forming rings (Ref. [66]).

Though the results presented here may seem poor, this is in fact one of the main methods used by some of the largest research groups [67]. The method's primary and unique advantage is that it does *not* require the CNTs to be grown directly onto the surface. This is crucial for CNT integration in MOSFET technology, which cannot survive the high temperatures of the CVD growth of CNTs.

### 3.3.2 Catalyst Patterning

The next method to be described uses the patterning of small islands of catalyst, from which the CNTs are then grown using the CVD method, on the surface [68]. This is similar to the nanotemplate method as it still requires high-resolution lithography to define the catalyst islands, yet the methods employed are far more compliant with current manufacturing techniques. Once the catalyst islands are created, the substrate can be placed in a CVD furnace, and the growth is somewhat dependant on the geometry of the islands. For example, as seen in Figure 19, one can pattern small islands on the tip of electrodes, and then hope that the CNTs will grow from one island to the other (or, rather, from one island to the other electrode). This process has achieved some promising results, but, being a random process, one can never be sure that there will be a CNT between the two electrodes. Nevertheless, these results were among the first to marginally pattern CNTs “where you want them”, while grown directly onto the surface using the CVD process.

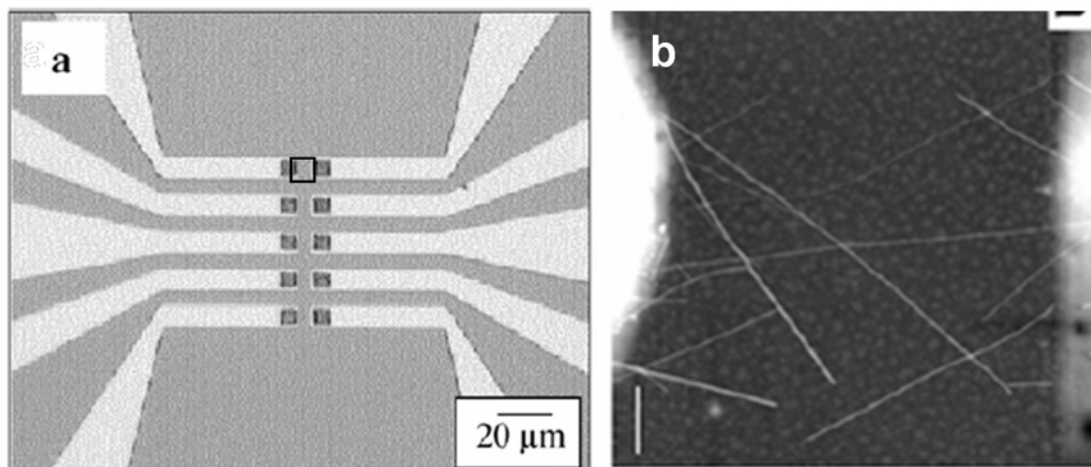


**Figure 19: Catalyst Island Nanotube Growth**

(a) Image of an electrode assembly with small islands of catalyst at the tips of each electrode. (b) Close up of the box in (a) showing the nanotubes bridging off each electrode. Both images from Ref. [68].

### 3.3.3 Field Alignment

Utilizing the previous method's advantages, a more controlled method for aligning the grown CNTs along a certain direction was created, which would negate the statistical process of the CNTs growing in all directions. Since nanotubes can be considered as a partially dielectric material, they are affected by an applied electric field. When in the field, they will align themselves to it so that they orient themselves parallel to the field lines [69, 70]. This can be done either before or after their growth.

In the latter case, nanotubes are deposited from their suspension between metallic electrodes, at which point an AC field is placed between the electrodes [71]. The CNTs will then align themselves between the electrodes, as seen in Figure 20a. The lines between the electrodes (top and bottom) signify that hundreds of nanotubes were aligned simultaneously between the electrodes.

When growing the nanotubes in the presence of an electric field (by connecting wires into the CVD furnace and attaching them to electrodes on the substrate), one can achieve nearly complete control over the direction of the growth [70], as seen in Figure 20b. The electrodes must be placed and positioned prior to growth, which requires them to be made of a material that can withstand the high temperatures of the CVD process, such as Mo. In addition, one can utilize the trapped surface charges on a material such as alumina, which creates a local electric field, to align nanotubes along the field lines, as in Figure 20c. The major limitation with these methods is that only the orientation in a single direction can be obtained, that of the direction of the electric field. Moreover, no control over the distance between parallel CNTs can be obtained using just this method.

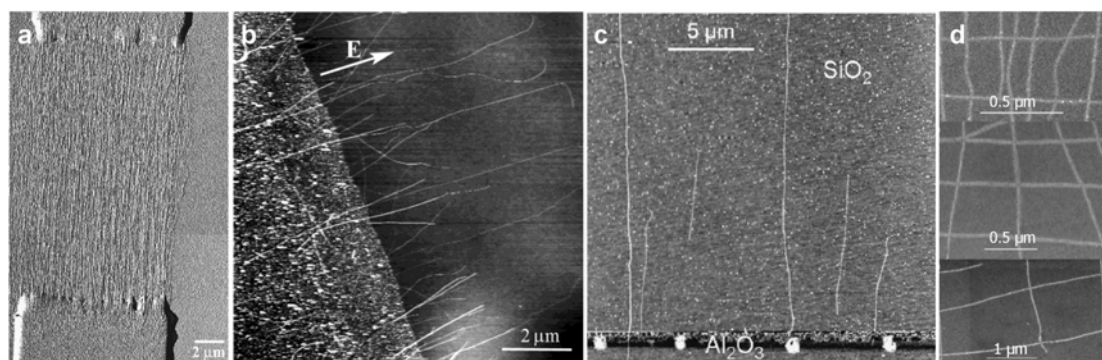


**Figure 20: Electric Field Alignment**

(a) AFM image of the alignment of deposited nanotubes between two electrodes and applying an AC field (Ref. [71]). (b) Active electric field alignment of the nanotubes during the CVD growth (Ref. [70]). (c) Static charge induced electric field alignment (Ref. [72]). (d) A two step process that involves depositing nanotubes and aligning them in one direction, using an electric field, and then aligning others in the perpendicular direction (Ref. [73]).

To further enhance the method described, a two step process can be used whereupon nanotubes are first orientated in one direction, and then another. For deposited CNTs in a suspension, this was accomplished by depositing the SWCNTs between two electrodes followed by the application of an electric field, and then taking the substrate, depositing more SWCNTs on the surface, and placing a field on another set of electrodes in the perpendicular direction [73]. The results of this process are shown in Figure 20d. The reticence exhibited towards the results presented in this image stem from the fact that the images are so small, and that they were not reproduced by the group any more. The problem lies with a number of issues. The first is that the images shown here only represent the center of the entirety of aligned tubes: none of the other sections displayed such alignment. A second problem (mentioned by the authors), is that there is far less control over the spacing between the SWCNTs than as presented in the image. A final issue is that the process itself, consisting of two steps, including the deposition of a second solution of SWCNTs on the surface, followed by

their alignment. When the second solution is placed on the surface, it affects the already aligned set, and therefore the second step slightly ruins the effect of the first. In fact, since it is also known that nanotubes can be partially aligned using a jet of nitrogen when on a surface [74], the pouring of a solution on top of the original set of aligned CNTs should obviously affect it, especially when the solution consists of reagents that are supposed to prevent the SWCNTs from sticking to each other.

### 3.3.4 Epitaxial Growth

An interesting development in nanotube alignment consists of a CNTs alignment to the atomic steps of a surface. This was discovered on substrates of high plane-index sapphire [75] (Figure 21a), as well as on specific planes of oxide/quartz [76] (Figure 21d). In such growth models, the nanotubes align themselves to atomic steps on the surface of the substrate, during the CVD growth, as shown Figure 21b, c. This is a form of “epitaxial growth” in that the nanotubes, which are molecules, align themselves to the crystalline surface. By placing islands of catalyst in specific locations, one can further define where the CNTs will grow. Using this method on quartz, extremely dense arrays of CNTFETs were fabricated (Figure 21e, f), and due to the parallel nature of the CNTs between each set of electrodes, the transistors were able to operate at high power; some of them running milliamps of current through them. Nevertheless, the technique is limited to both a single atomic plane direction, as well as relying on non-standard substrates, which are not preferred in the IC industry. While the first issue can be resolved by integrating this method with the previously described method of field alignment, the second issue remains inherently problematic to the entire technique.

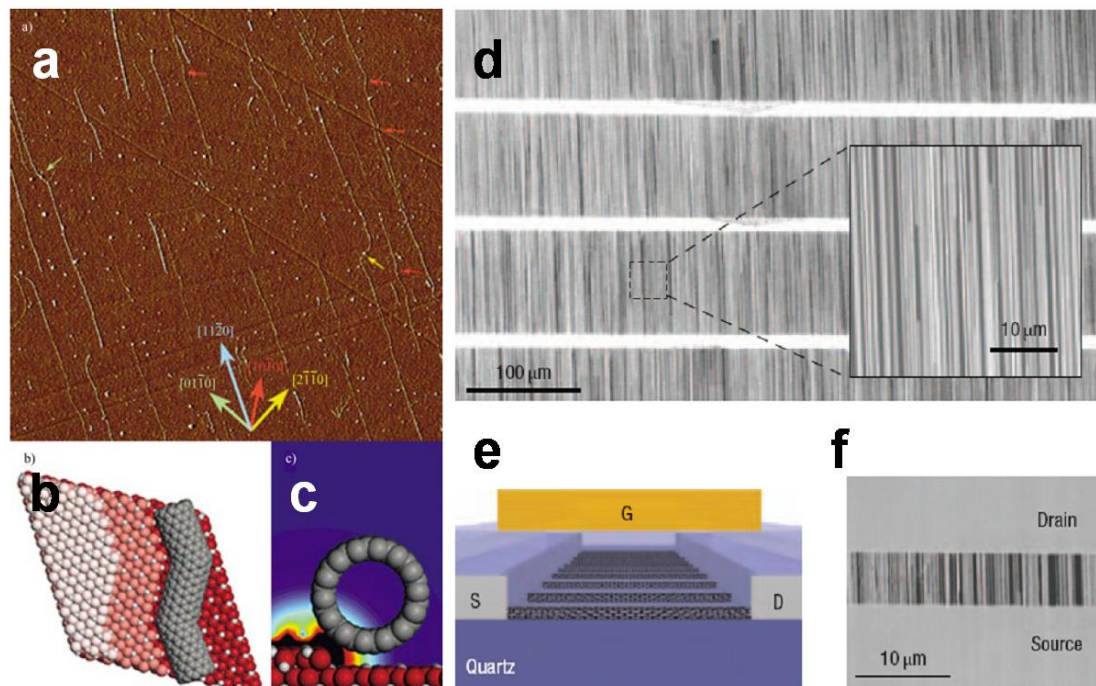


**Figure 21: Atomic Step Nanotube Growth**

(a-c) Nanotubes aligning themselves to the atomic steps on a substrate of off-axis sapphire (Ref. [75]). (d-f) Extremely dense arrays of parallel nanotubes, grown on an off-axis quartz substrate, along with strips of electrodes, defining large scale, parallel transistors (Ref. [76]).



### 3.3.5 Soft Lithography

A recently innovated method of producing small features on just about any substrate, without the need for regular photo-lithography methods is the technique of soft lithography. This technique can be described quite simply as a stamping mechanism, with a pre-fabricated mold, covered with a “dye” to be transferred onto another surface. Of course, what makes the method interesting and useful is that the “dye” may be a liquid, but can also be any other transferable material. This is ideal for micro- and nano-fabrication, where the idea is to imprint SAMs or other molecules. The theory behind this technique is simple. For a medium to be transferred,  $A$ , which is attached to a stamp,  $B$ , and required to be transferred to a second substrate,  $C$ , the surface energy,  $E$ , must fulfill the following relation [77]:

$$E^{AC} > E^{AB} \quad (10)$$

with  $E$  being the surface binding energy. For example, Au can be transferred from a polar oxide  $\text{SiO}_2$  surface, to which it has very low adhesion, onto a dispersive material, using this method [77], and as appearing in Figure 22c, where both Au and Pn were transferred to another surface in this manner. Yet, more important and pertinent is that nanowires and nanotubes have been transferred using this method [77-79].

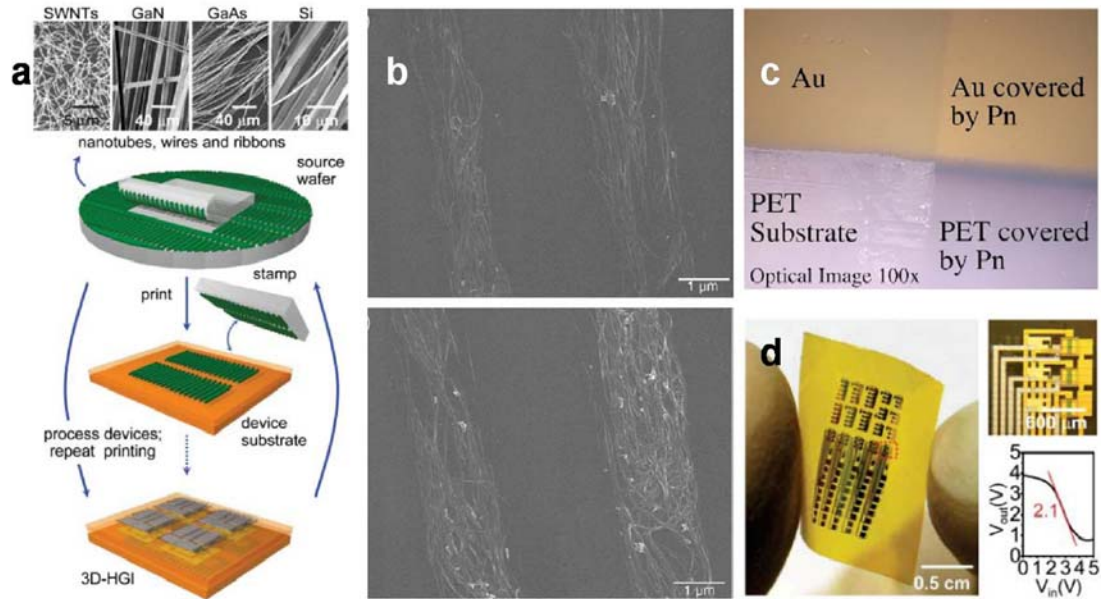


**Figure 22: Soft Lithography Transfer Printing**

(a) Schematic of a method of creating large-scale electronics on flexible surfaces using soft lithography. The materials transferred range from nanotubes to nanowires (Ref. [78]). (b) SWCNTs transferred using the same method, resulting in well aligned strips of nanotubes (Ref. [79]). (c) Transference of metallic thin films onto other substrates (Ref. [77]). (d) A large scale electronic device, using the method in (a), generating hundreds of inverters based on nanowires (Ref. [78]).

Figure 22 displays some examples of transfer printing. The method is described in Figure 22a, where the underlying principle is to use a pre-patterned stamping mold to pattern the transferred medium (in this case, nanotubes and nanowires) onto other substrates that can then be patterned using standard lithography methods. In this case, the real advantage of the system can be seen in Figure 22d, where the substrate was chosen to be a flexible, transparent film, demonstrating the robustness of the transfer technique. Figure 22b shows similar results with SWCNTs. The SWCNTs were transferred by using a polydimethyl-siloxane (PDMS) stamping substrate covered with functionalized SWCNTs. The target substrate (Au) was then modified with a molecule (alkane-thiol) that binds to the functionalized SWCNTs better than the SWCNTs bind to the PDMS. The results of this transfer technique are quite similar to those created using the nanotemplate method described above and appearing in Figure 18. The main advantage of this method is that, once the stamping template has been fabricated, by whichever means, it can be reproduced using the same template in a reusable fashion.

### 3.3.6 Exact Positioning Patterning

There are currently two methods of patterning nanotubes in a nearly fully controllable manner: The rapid-annealing method and the direct stamping method. These two methods are currently the “cutting-edge” in terms of exact patterning. The first method [80] utilizes what is known as the rapid annealing method to grow straight and long nanotubes, in which the sample is quickly heated to the growth temperature. The nanotubes then grow along the orientation of the gas flow within the CVD furnace. By properly positioning the catalyst islands, using lithographic methods, one can control the orientation and positioning of the SWCNTs. Furthermore, by taking the substrate, adding more catalyst islands, and then inserting back into the CVD furnace, one can create nanotubes in a perpendicular array, as in Figure 23a and b. These results may seem quite similar to those presented in Figure 20d, but there is an obvious difference between the methods. The first is that the arrays created here are much larger, and better defined throughout the array. Additionally, since the SWCNTs were created using the CVD method, directly onto the surface, the SWCNTs themselves are not covered with chemical solvents needed in dismantling the bundles created when using other methods. Finally, unlike the method described in Ref. [73], here, the spacing between nanotubes can be well controlled by the initial placement of the catalyst islands. Nevertheless, this method still requires a multiple step process to achieve more than one direction, as well as requiring the sample to be placed in the CVD furnace, at temperatures that will ruin most IC compatible materials. Moreover, as can be seen in the images, the straightness of the nanotubes is limited by the rapid annealing process.

The second method [81], involves the direct stamping of a single, well defined, SWCNT, exactly where one wants it, using optical alignment. First, SWCNTs are grown over a trench in a silicon based substrate. Then, using Rayleigh spectroscopy, all of the nanotubes over the trench are scanned and a particular nanotube is chosen. The rest are burned away using a laser; thus, a specific, individual (n,m) SWCNT can be chosen. Next, using an alignment procedure, the single nanotube is stamped onto a separate surface. To cause the nanotube to be transferred from one substrate to the other, photo-resist was poured through the bottom of the now upside-down trench,

and then cured. This step was taken to ensure that the SWCNT was “held down” to the new surface. At this point, the source substrate (with the trench) could be lifted off, with the suspended segment of nanotube remaining on the target substrate. This process is described in Figure 23c, with a single SWCNT positioned in a well defined location. The transferred nanotube can then be contacted using lithographic methods, such as e-beam lithography, to obtain a large number of parallel transistors on the same, extremely straight, segment of SWCNT [82]. The method described seems quite complete, in that it achieves the goal of putting a specific nanotube exactly where one wants it.

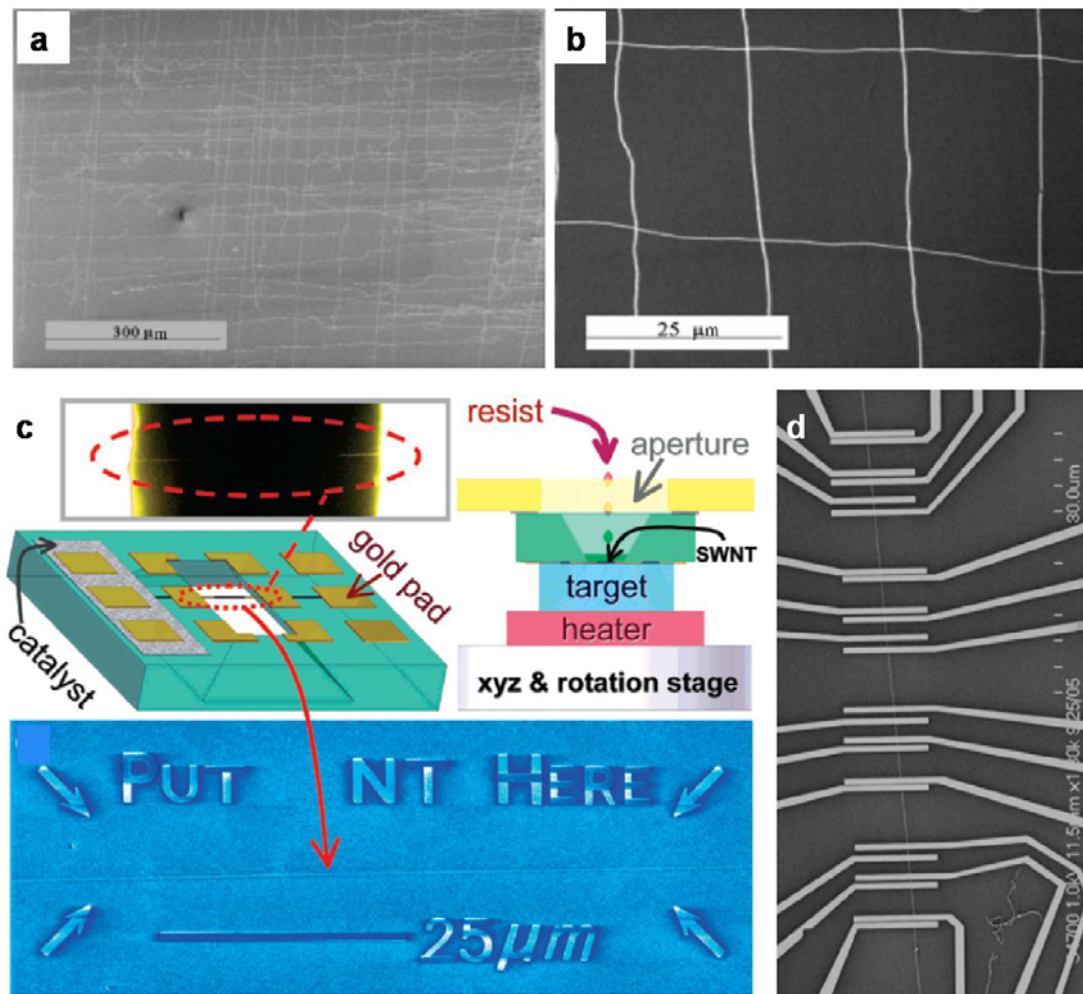


**Figure 23: Cutting-Edge Controlled Placement Methods**

(a) and (b) Well aligned and spaced nanotubes using a two step, rapid annealing process (Ref. [80]). (c) Controlled placement of a single, long, nanotube, showing the schematic method involved. A nanotube grown over a trench is stamped directly onto another surface, and can then be contacted using lithographic methods, as in (d). From Refs. [81] and [82], respectively.

Unfortunately, while the results presented in Figure 23 are undeniably good, the method suffers from a few drawbacks. The first is that only a single nanotube can be transferred at a time, if the location of the transferred SWCNT is to be well-determined. This is especially critical when one realizes how many parallel SWCNTs grow across the trench, all of which must be burned away after choosing a specific nanotube using the Rayleigh spectroscopy. In addition, while the perpendicular

arrangement of nanotubes can be created using this method (not shown), each stamping requires all the abovementioned steps, complicating the process, and making it untenable for mass-production techniques. Finally, the subtle problem not mentioned by the authors is in the alignment process: in order to optically align the nanotube, it was first covered in a thick layer of Au, so that it could be seen in a microscope. This can be seen in the upper left of Figure 23c. What this means is that one is no longer dealing with a SWCNT, but rather a SWCNT Au-covered nanowire. Needless to say, to obtain CNTFETs using this method, one must randomly stamp the nanotubes onto the surface, and then find them with an HRSEM, as was done later by the group, in Ref. [82].

### **3.4 Nanotubes between Pillars**

Moving to a tangential subject that is essential to the work described in this thesis, is an interesting way of patterning CNTs via their growth between micro-fabricated silicon pillars. Initially demonstrated in 1999 [83], it was shown that if silicon pillars (capped with  $\text{SiO}_2$ ) were created, and then their tops were coated with an appropriate catalyst, nanotubes would grow between nearest-neighboring pillars, creating a neatly arranged, suspended network (see Figure 24a-c). It was also found that long segments of SWCNTs can bridge between adjacent pillars, creating a long straight individual nanotube, in the direction of the pillars [84], as in Figure 24d. Creating such pillars utilized standard microfabrication techniques, and the coating of the pillar tops was implemented by placing a complex, block copolymer based catalyst on a PDMS stamp, and then stamping only the pillar tops with the catalyst. The network of suspended SWCNTs then formed spontaneously during the CVD growth process. This work on suspended nanotubes was then taken up by another group, which reported even smaller knit networks on 100 nm high silicon pillars [85], defined using e-beam lithography, as in Figure 24e.

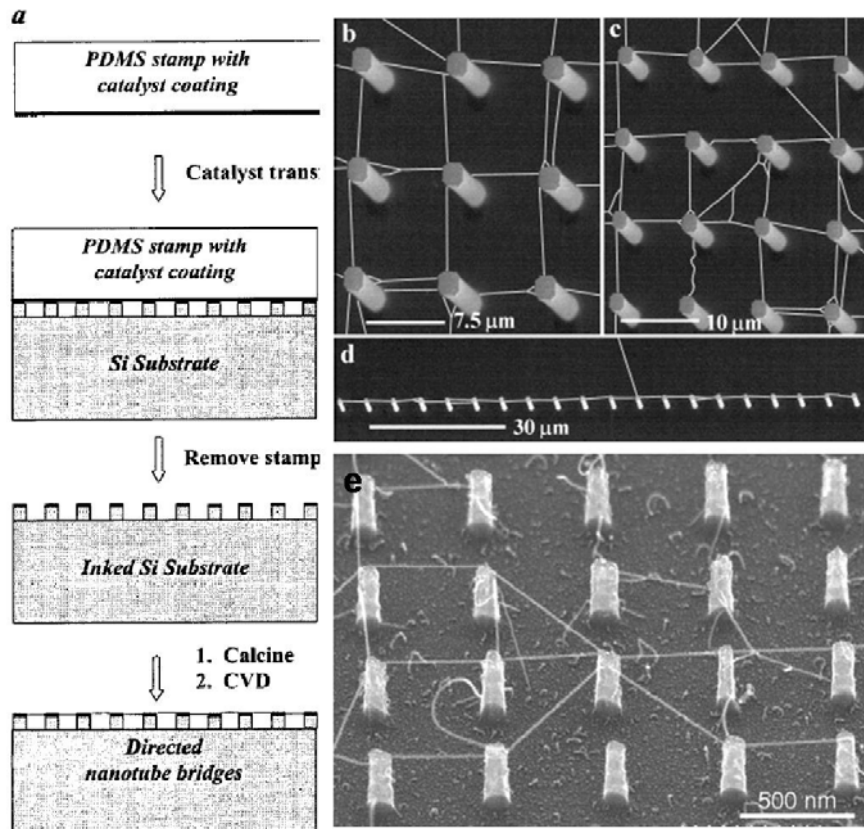


**Figure 24: Nanotubes Between Silicon Pillars**

(a) Schematic of the fabrication process used to create suspended nanotubes between silicon pillars (Ref. [83]). (b-d) Results of the suspended growth method, displaying nanotubes bridging between neighboring pillars, including an extremely long (~100 μm) nanotube (Ref. [84]). (e) Nanotubes between 100 nm high pillars exhibiting the same taut network (Ref. [85]).

In all instances of suspended nanotube growth, including those created by field alignment as above, it was found that the nanotubes create an extremely straight, or taut, network. In the instance of nanotubes grown between pillars, it was found that the nanotubes connect between the pillars, and then somehow retain their straightness. It was initially postulated that bridging nanotube growth was caused by the SWCNTs growing horizontally from the pillar surface tops, and swinging in the air due to thermal vibrations [69,84], whereupon they would stick to neighboring pillars upon contact. Nanotubes were modeled as vibrating cantilevers, wavering as much as 6 μm at a length of 20 μm, according to the formula [69]:

$$\delta = \sqrt{\frac{0.846L^3k_B T}{YdG(d^2 + G^2)}} \quad (11)$$

with  $\delta$  as the vibrational amplitude,  $L$ , the length of the nanotube,  $k_B$ , the Boltzmann constant,  $T$ , the temperature (900° C),  $Y$  the Young's modulus of a nanotube,  $d$ , the diameter of the nanotube, and  $G$ , the van der Waals distance in graphite. It was also initially assumed that the nanotubes wavered as a result of the gas flow, however, the perpendicular orientation of the nanotubes, as seen in Figure 24b, c and e, demonstrate that this influence may only be partial.

Further analysis of these pillar growth structures were implemented, mostly by the same group and its affiliates [86,89]. They included HRSEM, TEM and RS analysis, as well as attempts at physically affecting the grown network. For example, as shown in Figure 25a, it was found that by irradiating the pillars with an electron beam, one could remove some of the stray nanotubes not bridging between pillars [86]. In addition, the correlation between the density of catalyst deposited on the pillars (in this case, using e-beam evaporation) and the density of suspended nanotube growth was also analyzed, as in Figure 25b [87]. Higher densities of catalyst produced higher densities of SWCNT growth, with an upper deposition rate limit of  $7.2 \times 10^{14}$  atoms/cm<sup>2</sup>, after which the thick catalyst layer produced only MWCNTs.

The source of the tautness was also analyzed in Ref. [88]. To analyze the growth, a special gas chamber was built and inserted into a modified HRSEM chamber. Gas flow was permitted into the chamber, and the growth was investigated *in situ*, as shown in Figure 25c. The slow formation of the network was discernable, and a theory was formulated, which will be discussed again further on, due to its relevance to the results presented here in this thesis. Finally, TEM analysis of the suspended tubes was carried out by slicing an incredibly thin slice out of the pillared substrate, and then placing it perpendicularly to the TEM beam, allowing the visualization of the SWCNTs [89], as in Figure 25d. The authors found that there were occasionally bundles of nanotubes, but that the vast majority of bridging nanotubes were, in fact, individual SWCNTs.

As a final note, despite the abundance of work done on the field of suspended SWCNT growth, no application was found for this type of unique growth.

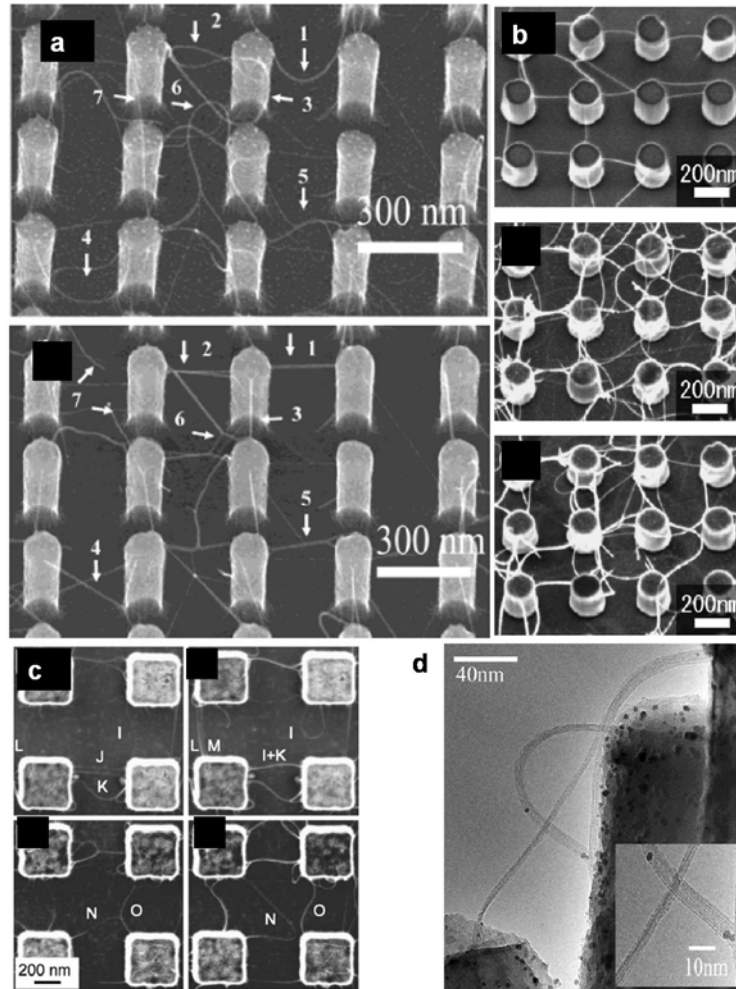


**Figure 25: Bridging Nanotube Growth Analysis**

(a) Removal of stray nanotubes (top to bottom) by irradiating them with an electron beam (Ref. [86]). (b) Change in density of suspended growth as a function of catalyst deposition: top to bottom correlates with higher density of catalyst (Ref. [87]). (c) Viewing the nanotube growth *in situ* with a modified SEM. These images tried explaining the origin of the suspended growth (Ref. [88]). (d) TEM analysis of the suspended nanotubes between pillars (Ref. [89]).

## 4 Research Goals

The objectives of this research can be briefly described as follows:

- Creating bridging networks of suspended SWCNTs, emulating previously published results. This was to be implemented at a much larger scale than previously reported results, with pillar diameters and spacing ranging from a few microns, to tens of microns.
- Investigating the origin of the tautness of the nanotubes seen in the network formation. This puzzling feature of suspended nanotube growth was repeatedly seen, but seldom was there any regard or interpretation for why such tightly bound networks would be created by the nanotubes between the pillars.
- Devising a way of utilizing this unique network formation for use in nanoelectronic devices.

As the aim of any cutting-edge research is to investigate the unknown or unachieved, therefore, the final objective was initially obscure, since there was no assurance that this goal would be met. This is especially the case when considering the fact that research on suspended nanotube growth has been in continuous progress by a number of top research groups for a number of years (specifically, the Dai and Homma groups), with no definitive results. Yet, as will be shown in the subsequent chapters, these goals were met, and so the shift in goals was made more apparent. Therefore, the goal of this thesis inevitably became to: *“produce a method of creating well defined, pre-patterned arrays of single-walled carbon nanotubes, such that they can be well integrated in current IC technology”*.

In the realization of this goal, a stamping method was developed that transfers the suspended nanotubes grown between the silicon pillars onto another surface. This method fully utilizes the unique network assembly of long and taut nanotubes, which retain their straightness after transfer. This also enables the capability of placing the patterned nanotubes onto a wide array of surfaces so that the arrangement of patterned and isolated single-walled carbon nanotubes can be utilized in complex device architectures.

The primary results of this work are currently in publication [90] or in press [91]. Furthermore, during the course of this research, two other papers were published [92,93], which relate to the TEM characterization of suspended nanotubes and their analysis. These papers will be summarized in the Results section, with an emphasis on the first two papers, which more directly relate to the core of this thesis.



## 4.1 Significance and Context of this Project

As stated in the Abstract to this thesis, the work presented described the ability to imprint large arrays of isolated and patterned, individual SWCNTs, in a one-step process, onto a wide variety of material substrates. One of the main objectives was also to retain the IC compatible aspect of the approach, since all current CVD reliant growth method positioning techniques require high temperatures.

Work in the field of nanotube patterning has been shown to be quite extensive and substantial, with some of the best research groups around the world investigating methods of CNT alignment. As a result, it is quite difficult to approach the field without full knowledge of the contemporary competing methods, as well as acquiring the appropriate fabrication capabilities. The trick is then to try doing something new, that has not been tried (successfully) before. In the context of the review in the preceding section, the final two sections regarding CNT placement and growth between pillars seemed quite unrelated. However, the beauty of the images of suspended nanotubes between pillars, as well as the quality of some of the formed networks, which inherently hold the capability of a well-defined array of SWCNTs, would seem to be a missed opportunity if they were not put to good engineering use. Furthermore, the extremely taut network formation is composed of long, straight segments of nanotubes, which are ideal if one is to envision the fabrication of multiple, parallel, complementary CNTFETs on a single strand of SWCNT, as rendered in Figure 26. Being connected to the same SWCNT, each CNTFET would exhibit the exact same device characteristics. This property of straightness, which was emphasized in the preceding section as well, is a crucial factor in the fabrication of such parallel CNTFETs, since every small kink in the nanotube is essentially a mechanical strain, which is accompanied by a drastic change in the electronic properties of the SWCNT [94].

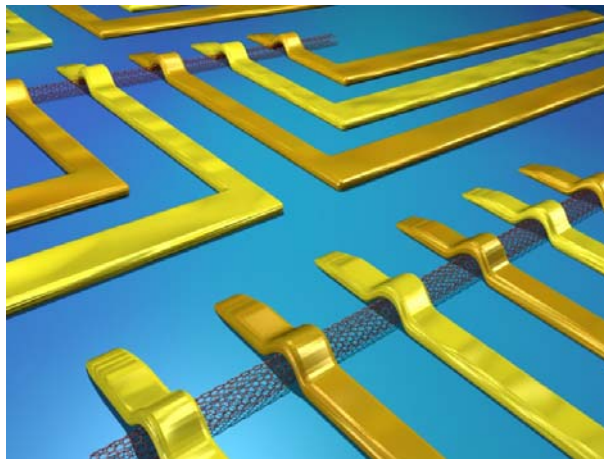


**Figure 26: Multiple Parallel Complementary CNTFETs on a Single Nanotube**

An additional aspect to this work is the ability to imprint the nanotubes onto a variety of substrates. As mentioned in the preceding sections, one of the major obstacles in CVD SWCNT growth is that the nanotubes cannot be grown on substrates that include temperature sensitive elements, such as MOSFETs or even thin electrodes. The imprinting methods described are ideal for such materials, with the work described here falling into a distinct niche of nano-imprinting.

## 5 Experimental Materials and Methods

The following chapter will describe the materials and methods used in this research, followed by the results, which, once the materials and methods are well understood, are easily described. The subjects described here encompass the entirety of the work described in this thesis, which included the fabrication of devices and CNT growth, as well as their analysis. All processes were carried out on 4" silicon wafers ( $\sim 450\text{ }\mu\text{m}$  thick), covered with a 500 nm thick thermal oxide layer. The oxide layer was crucial for both electrodes (where the electrodes must be isolated from each other) and the pillars (where the CNTs grow only off the  $\text{SiO}_2$ , and not the Si).

### 5.1 Fabrication Processes

Fabricating the pillars for CNT growth, as well as the electrodes for CNTFET analysis required many standard micro-fabrication techniques. The method of creating the silicon pillars is a well known procedure, requiring the use of photo-lithography, reactive ion etch (RIE), and deep reactive ion etch (DRIE, otherwise known as the Bosch process). The fabrication of electrodes required photo-lithography or e-beam lithography, followed by the e-beam evaporation of metals (Cr/Au). An extremely brief description of each of these techniques (viz. photo-lithography, e-beam lithography, RIE and DRIE) follows. A more in depth summary of the fabrication devices is not given, as they are merely tools, and their description can be found in any standard micro-fabrication book. All micro-fabrication devices used here are on-campus, either at the Tel Aviv University Micro-Fabrication Facilities, or at the Tel Aviv University Center for Nanoscience and Nanotechnology. Images of these devices can be found online, at their respective websites.

#### 5.1.1 Photo and E-Beam Lithography

To define the locations of both the pillars used for CNT growth, as well as large scale ( $>1\text{ }\mu\text{m}$  CD) electrodes, photo-lithography was used. For the smaller electrodes used, e-beam lithography was used. Photo-lithography uses various types of organic, photo-sensitive coatings, called photo-resist (PR), which change their properties when exposed to specific wavelengths of light. The photo-lithography in this work utilized a Karl-Suss MA-6 mask aligner for photo-lithography, operating at  $11\text{ mW/cm}^2$ . The PRs used consisted mainly of Shipley S1818 positive PR, for the pillar fabrication, and both TI35ES as well as AZ5214E negative PRs. The fabrication protocols for these PRs can be found in Appendix 3, 4. Variations on the protocols were also used, mainly in the alternation of the spin cycle, which directly affects the PR height (As a rule, the higher the spin cycle, the thinner the PR layer).

The masks used during the course of this research varied in size and resolution. Many different configurations of pillar and electrode masks were created. All masks were designed using the DesignCAD software in our lab. Low-resolution masks were produced by Suron Inc., with minimal feature sizes of a few microns ( $\pm 10\text{ }\mu\text{m}$ ),

whereas higher-resolution masks were produced with the laser-writer on campus. Both bright field and dark field masks were used, depending on the design and PR. In general, bright field masks were used in almost all instances (pillar and electrode design).

E-beam lithography was used for making contacts to individual CNTs. E-beam lithography works in a similar way to regular photo-lithography in that a resist is spin-coated onto a surface and then exposed and removed away in selected regions, with two major differences. The first difference is that instead of being sensitive to light, the resist is sensitive to the ionization of an electron beam. Polymethyl-methacrylate (PMMA) was used as the resist for the e-beam work described here. The second difference is that no set masks are used for the lithography. Instead, a substrate containing metallic alignment marks (usually, Au crosses in the corners of the chip) is placed in a specialized HRSEM (RAITH 051), and then coordinates are created using the alignment marks and the lithography software. One can then manually design electrodes that will be placed in the appropriate areas. The substrate can then be covered in PMMA, and re-inserted into the RAITH. The easily seen alignment marks are then used as the coordinate origins for aligning the drawn pattern to the substrate. An electron beam (i.e. the HRSEM) then exposes all the PMMA in the precise regions defined by the schematic drawing. The e-beam lithography method is far more complex than regular photo-lithography; while it is ideal for aligning contacts to objects that cannot be optically seen (e.g. CNTs), it also means that every time a new device is to be made, it must go through the entire process of mapping, drawing and exposure, which is time consuming. It also limits the manufacturing capabilities of the process, since every device is inherently custom-made.

### 5.1.2 RIE and DRIE

The etching processes used to dig out the pillars required a two-step process (after photo-lithography, as will be described below). Since the pillars were fabricated on a  $\text{SiO}_2/\text{Si}$  substrate, two different etching procedures were needed for the two materials, since, in order to achieve high aspect ratio pillars, the DRIE process was a necessity. The protocols used for the pillar fabrication process are standard, and the recipes used, (which can be found in Appendix 6, 7) were standardized processes in the devices used: namely, the Nextral NE 860 RIE, and Plasma-Therm SLR-770 Inductively Coupled Plasma Etcher DRIE.

The RIE process first requires that the areas to remain as pillars be protected by PR using standard photo-lithography. After the substrate is placed in a high-vacuum, the RIE bombards the material to be etched with highly energetic chemically reactive ions using an RF source for ion dissociation. Such bombardment with energetic ions dislodges atoms from the material in effect achieving material removal by sputtering. The RIE etches away part of the protecting mask (i.e., photo-resist) as well, and therefore, care must be taken in making sure that the *selectivity* of the RIE process is maintained. The process ends using an end-point detector that uses a laser interferometer, which constantly measures the index of refraction of the surface ( $n=1.46$  for  $\text{SiO}_2$ ). When the index changes (due to the underlying Si substrate), the process stops. Furthermore, a 5% over-etch was used to ensure that the entirety of

SiO<sub>2</sub> has been etched away. The RIE process used for SiO<sub>2</sub> etching utilizes a mixture of CHF<sub>3</sub> and O<sub>2</sub> gasses, at a high RF power of 200 W.

The DRIE process is similar to the RIE process, except that it ensures complete anisotropic etching for obtaining straight walls for the pillars. For the DRIE process, the PR layer usually does not provide enough protection for the harsh etching process, instead, SiO<sub>2</sub> is used as a “hard mask”, ensuring that only exposed areas of Si are etched. In the DRIE process, the etching of silicon is done with SF<sub>6</sub> plasma, followed by a coating of “Teflon”-like material, all at high-vacuum. This is done iteratively, so that between each etch, the side-walls are protected by the Teflon coating. By running through these iterations multiple times (e.g., ~40 for 20 microns), one can etch to large depths, while retaining nearly straight-lined walls.

### 5.1.3 E-Beam Evaporation and Sputtering

Creating metallic contacts using IC fabrication techniques are plentiful, but the evaporation method was primarily employed here. In evaporation, a crucible containing the metal to be deposited is “scanned” using an electron beam (i.e., heated). The metal, near its melting point, is then evaporated into an enclosed, vacuum-locked chamber containing the target substrate. The evaporated material adheres to the target substrate. Layer deposition thickness can be accurately controlled at thicknesses as low as ~1 nm. The metal must be chosen such that it adheres well to the target substrate. A Chrome (Cr) layer is usually deposited before a Gold (Au) layer on SiO<sub>2</sub> substrates, to ensure adhesion. The design of the electrodes (or other deposited layers) is controlled via the lithographic techniques described above, with the resist layer acting as a sacrificial shielding for the substrate. After the deposition, the resist can be lifted-off, using acetone, leaving the shielded areas clear of metal. E-beam evaporation was carried out using the evaporator in the TAU micro-fabrication facilities, as well as the evaporator in the Nano-center.

Sputtering of materials was also implemented in a number of experimental processes. Sputtering uses an RF source to bombard a target metal so that the ejected atoms are sputtered onto another substrate. Sputtering of metals (Ni, Co) and ceramics/dielectrics (TiN, Si<sub>3</sub>N<sub>4</sub>) was implemented for many experimental attempts (most of which do not appear in this thesis).

### 5.1.4 Nanostrip and Oxygen Plasma Substrate Cleaning

After etching the SiO<sub>2</sub>/Si substrate to create pillars using the DRIE, the residual PR on the pillar tops was completely removed before catalyst deposition. The PR is hard to remove due to the heavy “baking” of the substrate during the DRIE etching process. To ensure that not even a monolayer of PR remained on the surface, a rigorous cleaning procedure was performed. The cleaning process consisted of washing the substrate with acetone (the standard PR removal solvent), followed by sonicating the substrate in N-methyl-2-pyrrolidone (NMP), which removes the vast majority of the PR. To completely remove the residual PR, the substrate is then placed in Nanostrip for 10 minutes, on a hot plate at 60-80° C. Nanostrip is a ready to use solution of H<sub>2</sub>SO<sub>4</sub> and peroxide (H<sub>2</sub>O<sub>2</sub>), and etches away nearly all organic

compounds. The substrate is then washed with de-ionized (DI) water, and then further cleaned in both NMP and acetone, and finally IPA. This process was carried out in a chemical hood in the clean-room.

A final cleaning process that is used on both the pillars and on post-lithography substrates before electrode deposition is oxygen plasma. Oxygen plasma simply generates an ionized oxygen gas, under low vacuum conditions, that is highly reactive with carbon-based molecules. Therefore, it is useful for the removal of both monolayers of PR, as well as burning CNTs off a surface. The plasma process is easily carried out in a matter of minutes, and a plasma device exists in both the micro-fabrication facilities, as well as in our lab.

## 5.2 CVD Nanotube Growth

The following is a description of the CVD system used in our lab. It is relatively standard in comparison to other CVD nanotube growth systems existing in other labs across the world. The setup consists of a 1" quartz tube furnace (LindbergBlueM Minimate 1100) connected to gas flow controllers, and a computer. A completely automated program controls the temperature and gas flow, thus controlling the growth protocol. An image of the setup can be seen in Figure 27. The program's interface, programmed in LabVIEW 7.0, can be seen in Figure 27c. A newer, larger CVD system is currently being constructed.



**Figure 27: Computerized CVD System**

- (a) Schematic of the CVD system, consisting of a tube furnace, gas flow meters, and control box. (b) Actual image of the original CVD system in our lab, including the computerized control. (c) Screen-shot of the control panel for the CVD growth program.

The CVD protocol used can be found in Appendix 8. The growth of high yields of SWCNTs between the pillars was highly dependant upon the precise parameters shown in the protocol in the appendix, especially regarding the liquid catalyst deposition (as will be discussed in the results section). A complete description of the *finalized* growth procedure follows.

The first step required in the production of nanotubes was the growth catalyst. A few granules (approximately 2-5) of iron nitrate ( $\text{Fe}(\text{NO}_3)_3$ ) was dissolved in 20 cc of IPA. This solution was then sonicated for 40 min, and centrifuged for 10 min, to obtain a slightly yellowish liquid solution of nanoparticles. The solution was then deposited on flat sections of PDMS that had been pre-cleaned using oxygen plasma. After a short adsorption period, the liquid was blown off using a nitrogen jet. The

PDMS with the adsorbed nano-catalytic particles was then placed directly onto the pillared substrate, similar to the method described in Ref. [83]. In addition, a small amount of nanoparticle solution was dispensed upon the entire substrate, and then washed off in hexane. This seemingly contradictory final step relies on the nanotube's predilection to grow only off the SiO<sub>2</sub> pillar tops, and not the Si substrate and was empirically found to improve the growth yield. The substrates could then be placed in the tube furnace for CVD growth. Care is taken when placing the samples in the furnace, since their orientation in the tube affects the resulting SWCNT network growth.

The CVD growth process contains the following steps: First, a purging step consisting of hydrogen gas (1000 sccm – standard cubic centimeters per minute) at room-temperature is implemented, to assure that no oxygen (destructive to CNTs during growth) remains in the quartz tube. Second, the furnace is heated to 860° C, over a period of 20-25 min, while still having hydrogen gas flowing through the tube. Third, at the target temperature, ethylene gas (C<sub>2</sub>H<sub>4</sub>, the active carbon gas carrier) is added to the hydrogen flow at 20 sccm, for 9 min. After that, the ethylene is turned off, and the furnace is allowed to cool to room temperature, all the while with hydrogen gas flowing through it (at a lowered rate of 500 sccm). The samples are then removed from the tube furnace.

The combination of temperature, gas flow and catalyst type that resulted in the best growth was described. However, during the course of this research, multiple combinations were tried in order to fine-tune the process. They included various temperatures (800-900° C), gas types (mixtures including argon and methane), catalyst deposition methods (liquid vs. evaporated) and liquid catalyst types (including solutions of ferrocenes). The growth protocol described here took nearly two years to perfect, as will be described later.

This growth process was also used for the TEM grids (described later), however, the PDMS stamps were not used, due to the fragility of the thin nitride membranes, which would break off and attach to the PDMS upon contact. Therefore, they were only coated with the liquid catalyst solution, and cleaned in hexane. In addition, attempts at using solid-based catalysts, such as Co sputtered catalyst allowed the direct insertion of the substrate into the furnace, without the complicated liquid-catalyst dispersal process.

Finally, it should be noted that a newer, larger CVD system is currently being built in our lab. This CVD furnace will be able to accept substrates up to 3" in diameter, as well as allowing the placement of over half a meter of samples, in tandem. The larger furnace already has a computerized CVD system installed.

### **5.3 Suspended Nanotube Process Flow**

The following is a description of the entire fabrication and growth process, beginning with a single wafer of silicon, covered in 500 nm thick thermal oxide, and as visually described in Figure 28a. The wafer is covered with S1818 PR, and islands are created at the locations of the eventual pillars (Figure 28b). After exposure and development, the substrate is placed in the RIE for SiO<sub>2</sub> etching (all 500 nm, Figure 28c), followed by the etching of the underlying Si (15-20 μm, Figure 28d). The



substrate is then cleaned in the acidic and oxygen plasma cleaning process described above to remove residual PR. The pillar tops are then coated with the Fe based catalyst (Figure 28e) and placed in the CVD furnace, with the resulting formation of suspended nanotubes between the pillars (Figure 28f).

The Results section describes the cause for this network formation, as well as describes the advantages in the process flow described.

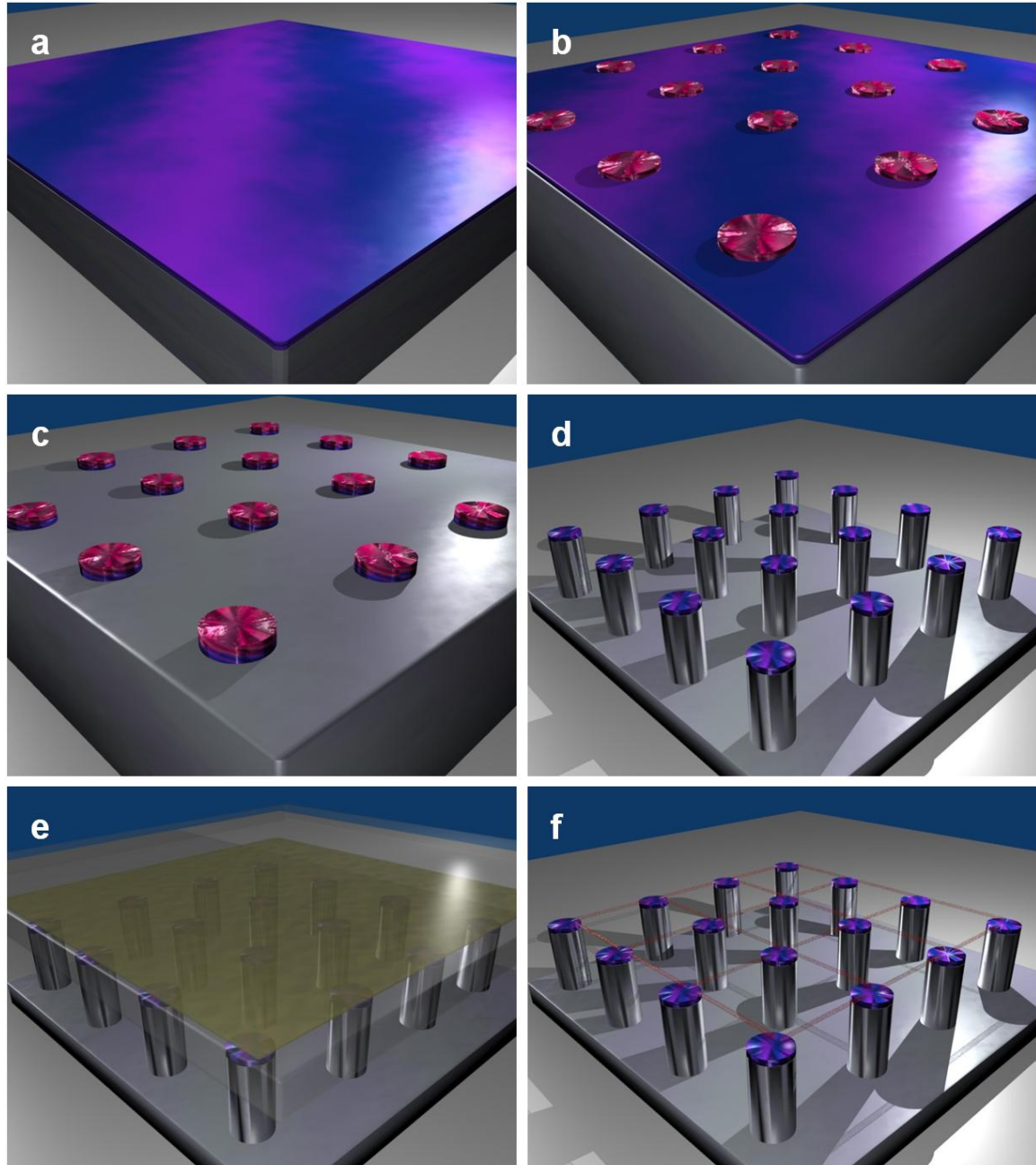


**Figure 28: Suspended Nanotube Process Flow**

(a) Slab of SiO<sub>2</sub> on Si. (b) Photo-lithography designation of the pillars. (c) RIE etching of the oxide. (d) DRIE etching of the Si (including residual photo-resist cleaning). (e) Catalyst stamping with PDMS. (f) Suspended network of nanotubes after CVD growth.



## 5.4 Imaging and Spectroscopic Techniques

A short physical description of the three major analysis techniques follows (HRSEM, TEM and RS). HRSEM and TEM work under the similar principal of emitting high energy electrons into a sample. The major difference is the working voltages, with TEM using higher voltages to attain both higher resolutions, as well as direct, transmitted electron imaging. Both HRSEM and TEM used at TAU were of the Field Emission Gun (FEG) type, obtaining higher brightness and coherence. RS uses a laser to detect vibrational modes in molecular structures, and therefore uses photon-“atom” (or, phonon) interactions instead. More emphasis on the mechanics of RS will be described here due to the complexity of the method, as compared to HRSEM and TEM.

Both HRSEM and TEM imaging rely on accelerating an electron via sets of electrically charged plates, with a voltage,  $V$ , between them, thereby achieving electron velocities in of over a million m/sec. Using deBroglie’s theorem, and correcting the velocity for relativistic energies, we can obtain the wavelength of an emitted electron from the correlation between wavelength,  $\lambda$ , and momentum,  $p$ :

$$\lambda = \frac{h}{p} = \frac{h}{\sqrt{2m_0eV\left(1 + \frac{eV}{2m_0c^2}\right)}} \quad (12)$$

with  $m_0$  being the electron mass,  $c$ , the speed of light and  $e$ , the charge of an electron. For accelerating voltages of, for example, 200 kV, which is the working voltage of the TEM used here, we can obtain wavelengths of 0.0023 nm.

### 5.4.1 HRSEM

The HRSEM works under the principal that “low” energy electrons (at voltages  $\leq 30$  kV) will only scanty penetrate a surface, and in doing so, emit secondary electrons that can be detected by a detector near the substrate. In fact, the acronym “SEM” could also stand for *secondary* electron microscopy. The added prefix HR- to the SEM signifies that the device is especially designed for working at extremely *low* voltages, down to even 1 kV. As related in the Literature Review, it was found that viewing SWCNTS was only possible at voltages  $\leq 1$  kV, which is why the HRSEM is necessary for viewing SWCNTs. The reason is that when the electrons are emitted into the substrate, the accelerating voltage correlates with the “depth” of penetration of the primary electrons. These primary electrons will then ionize nearby atoms, emitting secondary electrons in an “onion” like region around the initial penetration point. The size of this “onion” is greatly dependant upon the impact electron energy, and thus, the depth from which the secondary electrons are emitted (from the “onion”) rises as the primary electrons are given higher energies. When viewing SWCNTS on a surface, since their diameter is only a few nanometers, the penetration depth must be kept as low as possible, to obtain secondary electron emission from the nanotubes, limiting the use of only the lowest energies attainable with the HRSEM.

Two other imaging artifacts must be taken into account when viewing SWCNTs with the HRSEM, in the context of the work described here. The first involves the charging of the surfaces that the SWCNTs are viewed upon [95], and the second involves the change in brightness of a suspended nanotube when compared to that of a nanotube on a surface [96]. HRSEMs require the samples imaged to be conductive, so that the primary electrons can be grounded. Otherwise, the sample is quickly charged, and no distinction can be made regarding the secondary electrons. The SiO<sub>2</sub> surface is problematic in that it is an insulating layer, despite having a conductive underlying substrate of Si. This is especially poignant when using the low voltages of the HRSEM (1-2 kV), making the imaging of SWCNTs on a surface sometimes difficult. This is somewhat offset by the unique property of SWCNTs to emit high numbers of secondary electrons, and/or upon the electron beam induced current [95], which highlights long SWCNTs along their entire length (see Figure 29b). The second limitation lies in the contrast of suspended SWCNTs in comparison to those lying upon a surface. The suspended segments are always far less bright than the segments lying upon the pillars (see Figure 29a). This may simply be the result of the primary electrons passing through the suspended segments, but may also be due to surface plasmons created only on the suspended segments, which prevent the emission of secondary electrons [96]. Both of these artifacts in the imaging are crucial in understanding the limitations inherent in HRSEM imaging of SWCNTs. In addition, the change in contrast has the appearance of a change in dimensions, which is another reason why HRSEM imaging can *not* reliably be used to measure the diameters of single SWCNTs.

The HRSEM used in this research was the JEOL 6700 FEG-HRSEM, at the TAU Nano-center.

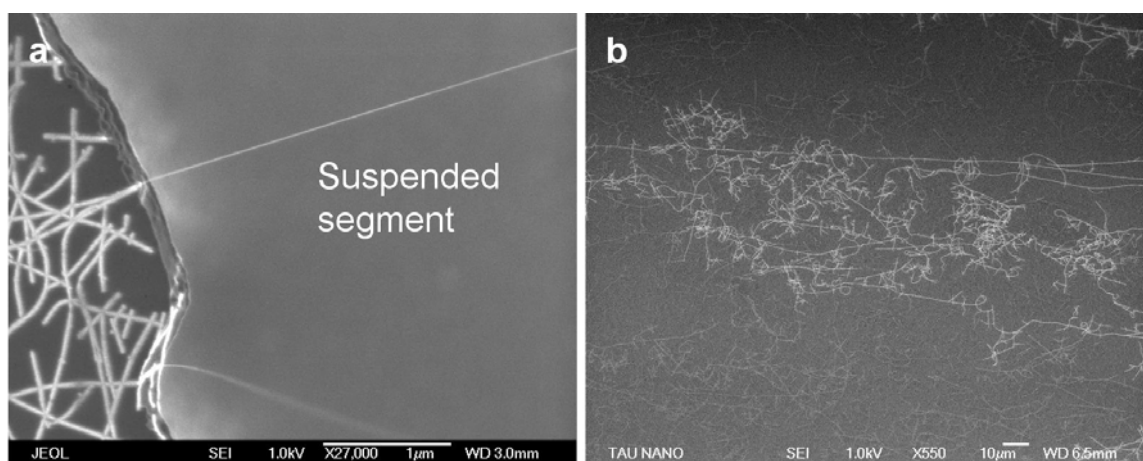


**Figure 29: HRSEM Artifacts**

(a) Change in nanotube contrast as it is suspended from a pillar. (b) Electron beam induced charging of sections of the nanotubes on a SiO<sub>2</sub> surface.

## 5.4.2 TEM

TEM analysis enables a much higher resolution, as can be inferred from the use of higher operating voltages (200 kV). In terms of imaging, the TEM uses the *transmitted* electrons, therefore enforcing the use of thin film samples only. It also requires an entirely different conceptual outlook of SWCNT imaging. Instead of

imaging ready-made samples, the TEM samples must be especially prepared for use in the TEM. This is mainly due to size restrictions as the TEM sample holder can hold a 3 mm<sup>2</sup> sample (typically a 3 mm disc), which must also be less than 1 mm thick. A major part of this research was implemented on specially designed TEM grids that consisted of 450  $\mu\text{m}$  thick Si substrates, with a large, etched hole in the center (see Figure 30). The Si grid substrates are coated in a thin, 200 nm thick, silicon nitride film (Figure 30c), which itself contains holes of varying diameters (DuraSiN TEM grids, Protochips Inc.). The grids used in this work mainly consisted of 40  $\mu\text{m}^2$  square holes (6 $\times$ 6 holes on the viewing area), and 2-4  $\mu\text{m}$  diameter holes, with a 12  $\mu\text{m}$  pitch. The advantage of these grids in comparison to standard copper grids is their robustness in the harsh conditions of the CVD growth. Thus, these grids were placed *directly* into the furnace after catalyst deposition, with the nanotubes grown directly onto them. This technique was developed and used by us in Refs. [90,92,93].

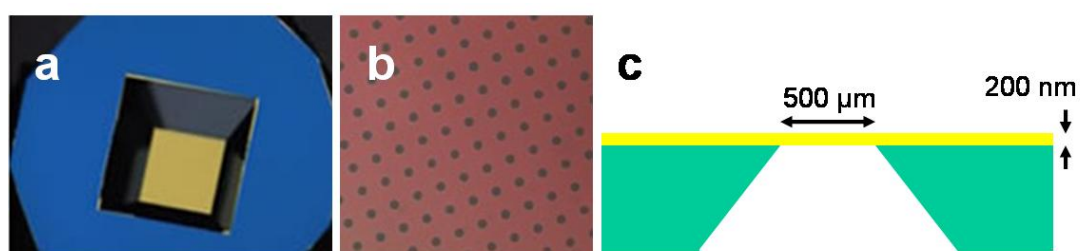


**Figure 30: TEM DuraSiN Grids**

(a) Optical image of the backside of the grid. (b) Close up of the imaging window in the center, with arrays of 2  $\mu\text{m}$  holes in the nitride film. (c) Schematic cross-section of the grid.

TEM imaging does not include the artifacts described above concerning the HRSEM. TEM imaging is ideal for measuring the exact diameter of SWCNTs, as well as viewing the multitude of structural deformities occurring in individual SWCNTs. However, as described in the Literature Review, there *are* limitations in TEM imaging, mostly involving the destruction of the nanotubes at high operating voltages. This limits the amount of time that can be spent on viewing suspended nanotubes. The TEM used in this work was the Philips Tecnai F20 FEG-HRTEM located in the Wolfson Materials Research Center at TAU.

The TEM image analysis was done using the Motic Images Plus software package in our lab. This included the measuring of diameters of individual SWCNTs.

### 5.4.3 Raman Spectroscopy

Raman Spectroscopy is ideal for analyzing the particular characteristics of an individual SWCNT, as described in the references of the Literature Review, as well as appearing in Appendix 1. A brief description of the physics of RS is provided in Appendix 1, whereas here, only the aspects involving CNTs are described.

In CNTs, the Raman spectrum is more complicated than that of a simple molecule due to the various vibrational modes possible. However, over the past decade, much research has been done on analyzing all of the vibrational modes in SWCNTs, and on demonstrating a correlation between a CNTs structure, to its Raman spectrum. A fairly comprehensive report on the relationship between CNT diameter and its Raman

spectrum can be found in Ref. [32]. Figure 31 displays some of the vibrational modes of a SWCNT, with the numbers below each figure corresponding to the specific peak in the Raman spectrum. The units of measurement in RS are in  $\text{cm}^{-1}$ , which correspond to the reciprocal of the wavelength. For these specific numbers, the most important vibrational modes in RS of CNTs are those denoted by the “165” and “1584, 1585” in Figure 31a. The “165” Raman peak is known in RS of CNTs as the Radial Breathing Mode (RBM), and the frequency at which this occurs is denoted as:  $\omega_{RBM}$ . From the figure, it is easily understood where the name RBM comes from, as it depicts the case where all the atoms in the unit cell (which is depicted in the upper left of Figure 31a) stretch out of the tube, essentially acting as if the CNT were taking a deep breath. In addition, the “1584-5” modes are known as the G-band, which comes from the graphite-like structure of the un-rolled CNT wall.

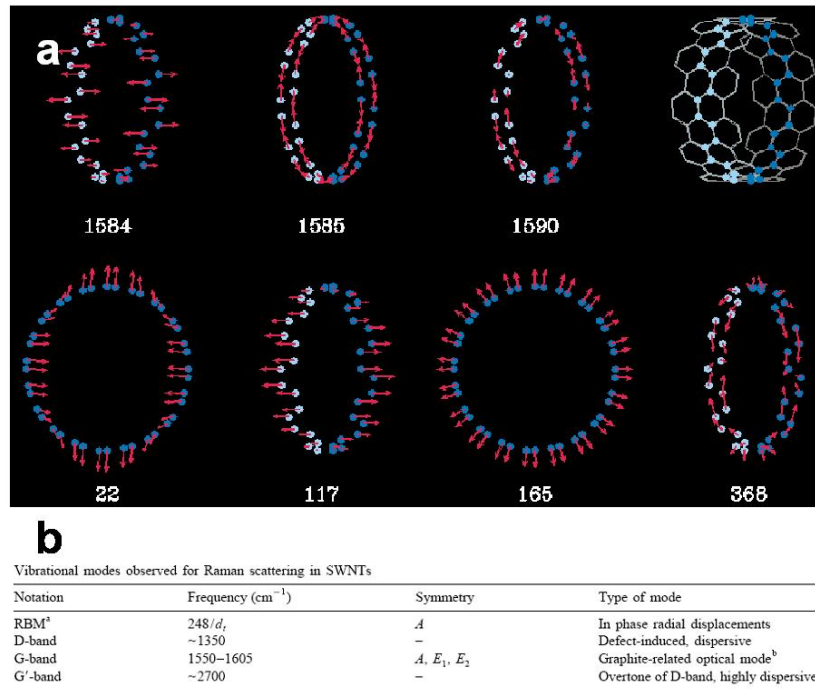


**Figure 31: Raman Bands from a Single Nanotube**

(a) Vibrations in a nanotube and their specific spectral bands (Ref. [31]). (b) Corresponding names given to some of these spectral bands (Ref. [32]).

In general, much of the knowledge regarding RS of CNTs originates in RS of graphite. Since the basic structure of both materials are nearly the same, many of the peaks concerning the phonon modes in graphite usually occur in CNTs as well, with the expectancy that the curvature of the graphene sheet will affect the line-shape and location of the peaks. In order to simplify discussions regarding RS of SWCNTs, the field has come to use supplementary terms for the RS peaks, such as the term  $\omega_{RBM}$  mentioned beforehand. Therefore, it is unnecessary to understand the types of symmetry groups usually discussed in RS, and one can usually look at a Raman spectrum, identify the peaks, and use the various references for CNT RS. The most important bands, namely, the RBM and G-band are the most important in CNT analysis, however, the D- and G'-bands are also important. The frequency range of these bands is also given in Figure 31b. As has been described previously in the Literature Review section, these values are structure related, which is why there is a range of frequencies for each band, as seen in Figure 10. However, this structural

dependency is *precisely* the reason RS of CNTs is so useful, as it gives information regarding the exact structure of a CNT.

Resonant Scattering is possible only if a tunable laser is used, in which case the Raman signal is amplified. While the Raman signal is weak when compared to the Rayleigh signal (which is at the frequency of the input laser), at the same angle, when the laser signal is exactly in tune with the “band gap” defined by the  $E_{11}$  bands, resonance occurs. Unlike semi-conductors, it is not only required to surpass the band-gap of a 1-D material, but rather, perfect resonance is achieved at exactly the Van Hove singularities. Since the  $E_{11}$  set of bands in the DOS of a SWCNT is known (see, e.g., Figure 4), then by tuning the laser frequency, one can find the band gap of the specific SWCNT, and compare it to a specific (n,m) simulation of a SWCNT. Such a table appears in Appendix 1. From these tables (and others existing in the literature), information regarding the structure of a specific SWCNT can be derived. The chiral angle is deduced by the values of (n,m) found for each tube, and as related by the formula given earlier.

In addition to the Resonant Scattering condition, and RBM mode, the other bands in the Raman spectrum, *viz.* the G-, G'- and D-bands, also have radial dependencies. Each of these bands can provide further information regarding the structure of a SWCNT. For example, as shown in Figure 31a, there are two vibrational modes that are distinct, yet give peaks at nearly the same location (1584-1590  $\text{cm}^{-1}$ ). This *G-mode* is actually made up of *three* peaks, which can be shifted in respect to one another, depending on the CNT. The third peak is that of the vibrational mode listed as “1590” in Figure 31a. This vibrational mode is *independent* of the tube diameter, and is connoted by  $\omega^+$ . The other two peaks comprising the G-band (1584, 1585  $\text{cm}^{-1}$ , which, for all intensive purposes, create a single peak), are shifted in relation to this, relatively constant, band. An empirical relation between the  $\omega^+$  band and the  $\omega^-$  band (i.e., the composite of the other two bands) is given by:

$$\omega^-_G = \omega^+_G - C / d_t^2 \quad (13)$$

where  $C = -47.7 \text{ cm}^{-1} \text{ nm}^2$  for semi-conducting nanotubes, and  $C = -79.5 \text{ cm}^{-1} \text{ nm}^2$  for metallic nanotubes. Therefore, detecting the difference between these two peaks can also give a measurement of the diameter of the SWCNT.

The RS used in this research was done in conjunction with Prof. Ori Cheshnovsky and Zvi Ioffe from the Chemistry Department, using a custom-built system. This system also included the ability of spatially mapping a substrate by combining the Raman laser with an optical microscope. Using this system, pixelized mappings of the RS signal were created.

Raman mapping equipment entailed an in-house designed RS system, consisting of Andor Shamrock 303i spectrograph combined with Andor Newton/iDus cooled CCD camera, 532nm laser (B&W Tek), and a custom-made confocal optical microscope with a computerized control system, which allows the user to move the sample and analyze the received spectrum simultaneously, thus scanning and raster-mapping the desired area.

Minimal pixelization was limited by the piezo-motor setup driving the sample chuck (minimal step 0.1  $\mu\text{m}$ ), as well as the spot-size of the input laser, at  $\sim 0.5 \mu\text{m}$ . Mapping consists of creating “spectral windows” around each peak desired to be mapped in the spectrum. Each spectrum per pixel can also be saved in the computer for further analysis. Furthermore, every such “spectral window” can be mapped simultaneously, creating different “Raman maps” of the same region, corresponding to different vibrational Raman modes of the molecule of interest.

## 5.5 Stamping Method

The full details of the stamping method, an integral part of this research, will be further described in the Results section. However, here is described the final method used for stamping the pillared substrates containing the suspended nanotube network to a target substrate.

The source substrates containing the pillars are cut into individual dies, using a diamond scribe. The target substrate is also pre-cleaned using IPA, acetone and oxygen plasma (where applicable). A hot plate is then heated to 150-200° C and a thin aluminum foil sheet is used to cover the surface, in order to prevent contamination of the samples resulting from previous use of the hot plate. The *target* substrate is then placed on the hot plate, and allowed to reach the hot plate temperature. The *source* substrate (i.e. the pillars) is then placed, upside-down, on the target substrate manually, using a tweezers. After placement, pressure is applied from above (manually again, using the back end of the tweezers), and a few small drops of DI-water are injected (using a standard hypodermic needle) nearby, preferably on the target substrate, so that the near-boiling water quickly evaporates around, and in between, the source and target substrates. After complete evaporation of the DI-water, the source substrate is then removed from the target. This process usually leaves an identifiable “water stain” on the target substrate such that, using an optical microscope, one can see the exact pattern of the stamping pillars on the target substrate. This latter effect is sometimes crucial for later locating the stamped tubes in the HRSEM, as it provides visible coordination markers.

## 5.6 Electrical Measurement Systems

Measuring the CNTFETs created in this work utilized the equipment available in our lab. All measurements were implemented in a closed probe station (Karl-Suss PM5), in conjunction with a pico-amperimeter (Hewlett Packard 4140B). These measurements were done using a basic LabVIEW created program, and the data was analyzed using Igor Pro. Measurements consisted primarily of transistor I-V curves, changing the gate voltage and measuring the drain-source current, while measuring the gate-source leakage current via a large, 1 M $\Omega$ , resistor in series with the gate voltage.

## 6 Results

This chapter presents all the major points relevant to the central project constituting this thesis. The primary results have been published, or are currently in publication. As the primary goals of this thesis have been in terms of fabrication, the results will be presented in the order of fabrication of the CNT networks, from the creation of pillars, to the CVD growth of SWCNTs, their analysis and then the crucial stamping method and the analysis of the stamped array. Preliminary conclusions will be placed in the text, in the appropriate location as necessary, with a final summary and conclusion section following in the next chapter.

### 6.1 Pillar Design and Fabrication

The first step necessary for this project was the fabrication of arrays of pillars, following the example of Ref. [83]. Many different designs were used in this thesis, with various geometries and sizes, as well as resolution and quality of the photo-lithography masks employed. As is in many other instances, some of the seemingly capricious decisions lead to interesting, unexpected results.

The main rule initially used for the design of the pillars was that their height had to be at least as large as the distance between them, so that the bridging nanotubes would reach a neighboring pillar before reaching the ground. The height of the pillars was to be determined during the DRIE process, and the spacing, via the masks employed in the photo-lithography process. The first masks designed were created using a low resolution plotter, which limited the pillar diameters to a minimal CD of 10-20  $\mu\text{m}$  ( $\pm 5 \mu\text{m}$ ). This also limited the spacing between pillars, i.e. the pitch, to a lower limit of 10-20  $\mu\text{m}$ . These seemingly innocuous facts actually lead to the findings that the bridging network growth could even occur at such large distances, after CVD growth of the CNTs. This was a surprise, as the previously published works on this type of growth only used much smaller spacing, from 500 nm to a few microns, as described before. This drove us to continue our attempts at creating large scale networks of CNTs.

However, a major limitation eventually turned out to be the DRIE process. Initially, the obvious design would be to create an array of pillars on a surface, which would be etched using the DRIE process, leaving only the pillars. However, due to the nature of the plasma during the DRIE process, creating isolated arrays of small pillars turned out to be quite difficult, as the isolated pillars were usually etched away as well, leaving behind small stumps, as displayed in Figure 32a. It was quickly determined that placing too many open spaces, either between dies, or even within each die itself, lead to the inadvertent destruction of the pillars. A solution was quickly found to both increase the density of pillars within each die, as well as place each die within an etched “well”, meaning that the area *between* dies would not be etched. An optical image of such a design (from an early, low resolution mask) is presented in Figure 32c. The areas surrounding the pillars are darker, as they are  $\text{SiO}_2$ , as opposed to the lighter (shiny) Si bottom.



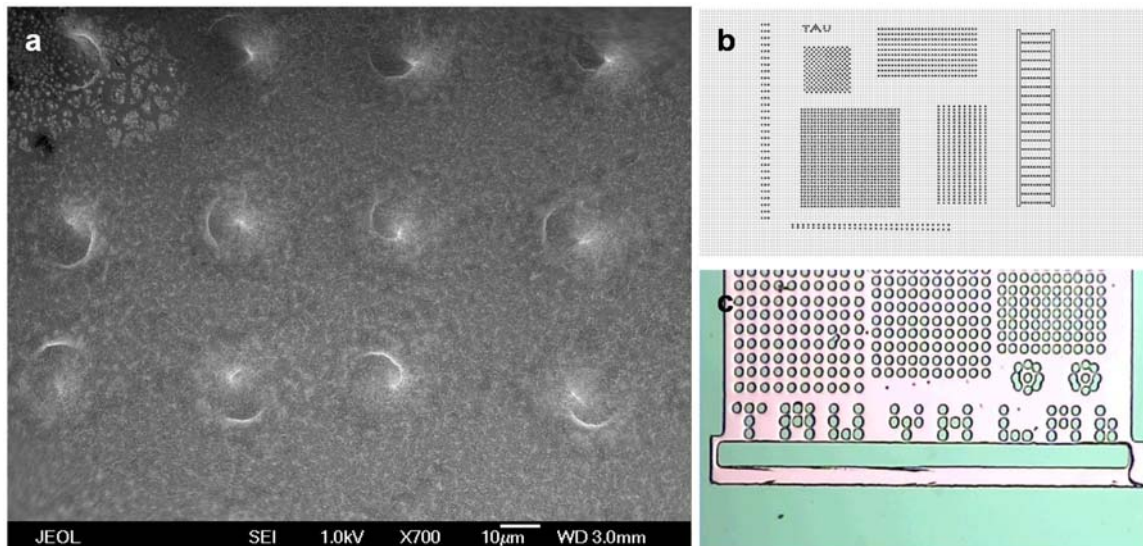


**Figure 32: Pillar Designs and Bad Etching**

(a) HRSEM image of pillars etched away during the DRIE process, leaving small stumps behind. (b) Original mask design (DesignCAD) of a single die, with large arrays of pillars, completely isolated, with large spacing. (c) Optical image of pillars placed in a well.

From these conclusions, we created better designed masks, especially with the introduction of the higher-resolution laser-writer at TAU. Since the better results, especially the stamping results, concern these higher quality (chrome) masks, the discussion here will be confined to them: Circular diameter pillars were created in a wide range of diameters, pitch and geometries, with the major geometry tested that of a square array. Other shapes were used, however, due to the tube-surface interactions (TSI) it was found that the circular pillars were, in fact, the best design (as will be explained later). Spacing between pillars ranged from 4 to 25  $\mu\text{m}$ , once the resolution was improved, and some other interesting geometrical combinations were also tested, as is evident from the pillars at the bottom of Figure 32c, and Figure 33a. The latter part of this work also included teeth-like designs, as will be shown later, and as can vaguely be seen in Figure 33b. In addition, by placing the pillars in a well, trenches were created around each die, to facilitate the dicing of each die with a diamond scriber. These trenches are also connected to well itself, as can be seen in the long trench at the top of Figure 33b.

While the placement of the pillars within the wells solved the problem caused by the DRIE etching, it also created a problem concerning the stamping process described later. This is due to the bordering areas being the same height as the pillar tops, meaning that nanotubes on those regions are stamped as well. It also causes additional problems that will be addressed in a later section. A final note regarding the strength of the Si pillars: While during the stamping process, a large amount of pressure is placed on each die, and consequently, dispersed over all the pillars, they almost never tend to break. Thus, small pillar diameters could also be included in the design, despite the large aspect ratio (e.g. 2  $\mu\text{m}$  diameter vs. 20  $\mu\text{m}$  height). Nevertheless, it should be noted that if too much force is exerted onto the pillars, there is a chance that they will fracture, as displayed in Figure 33c.

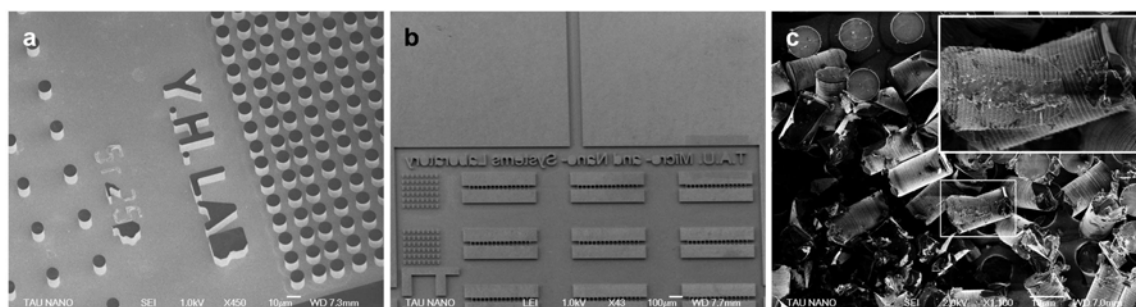


**Figure 33: Additional Pillar Designs**

HRSEM images. (a) Different arrays of pillars with 10  $\mu\text{m}$  diameters and a pitch of 5 (right) and 25 (left). (b) Design displaying a combination of teeth-like boxes and pillars (on the left edge). A trench is shown leading from the well to the edge of the die. (c) Results of extraneous pressure on the pillars. Close up displays the ridges created by the DRIE process.

## 6.2 CVD Growth of Suspended Nanotubes

After creating the pillars, the substrates were coated with catalyst, and placed in the CVD furnace. This step, as described in the previous chapter, took a long time to perfect. To summarize the results, it was found that the initial use of iron nitrate in IPA, deposited using a PDMS stamp, was found to be far superior to the methods described in the literature. In fact, as will be presented shortly, the yields of suspended nanotubes between pillars is of several orders of magnitude higher than those reported in Ref. [84], which also utilized a liquid based catalyst. It is also at least as good as the high yields reported in Ref. [86], which utilized e-beam evaporated catalyst layers. It should also be noted that this former group, (the Homma group, originally at NTT in Japan,) has been working on these suspended nanotube growth structures for over five years, and the yield of SWCNTs reported using their method has changed dramatically over that time period, as described in well over ten journal papers.

The problem of yield lies in the adhesion and adsorption of the nanoparticle catalysts to the  $\text{SiO}_2$  pillar tops. The problem was found to be twofold, with the first being the cleanliness of the sample prior to catalyst deposition, and second with the exact method of deposition and concentration of the liquid catalyst. The solutions were those described in the methods section beforehand, and whose explanation is provided here.

The first problem concerned the residual layer of PR on the pillar tops. This was found to be especially crucial when dealing with the smallest pillars ( $<5 \mu\text{m}$ ), and was not as problematic with the initial, larger pillars. It may also be a function of the age of the PR used, as it occasionally did not pose a problem. The PR would leave a residual layer even after lengthy sonication procedures. Therefore, the substrates were cleaned using the detailed protocol described above. Without this pre-deposition cleaning process, the catalysts would adhere to the residual PR layer, which would then “burn off” during the CVD growth process.

The second problem lies at the heart of the deposition process, and is that of placing the needed amount of catalysts upon the pillar tops. Here, it was found that the

smaller the pillar top, the harder it was to obtain a high yield of suspended nanotubes. This is most probably a result of the surface binding energy on the pillar tops, which is amplified by the edges. Smaller pillar tops thus have larger surface forces. Hence, the deposition of catalyst particles on small pillar tops is more difficult. The other groups working on such structures used other methods to deposit the catalysts, including the use of complex chemistry to bind the catalyst to the pillar tops, as described previously. Consequently, for pillar diameters of even 5-10  $\mu\text{m}$ , initial attempts at obtaining high yields of suspended SWCNT growth were usually unsuccessful. As a result, the process was carefully modified until the optimal protocol was obtained. Two of the changes made to the original protocol that appear to be decisive are the plasma cleaning of the PDMS and the heating of the substrates prior to stamping the PDMS. The first issue may improve the adsorption of the IPA-catalyst solution, due to the PDMS alternating its hydrophilic properties (although IPA is non-polar). Improved results were initially found with “old” PDMS, which was created at least over a month before its use as a catalyst stamp, lending to the possibility that the PDMS needed to undergo a transition in order to be viable for stamping (e.g., additional curing). The second issue, that of heating the substrate, is similar to the singe process used in photo-lithographic recipes, where the objective is to prevent water molecules – intrinsic to the humidity rich TAU atmosphere – from adsorbing onto the surface, and preventing catalyst adhesion.

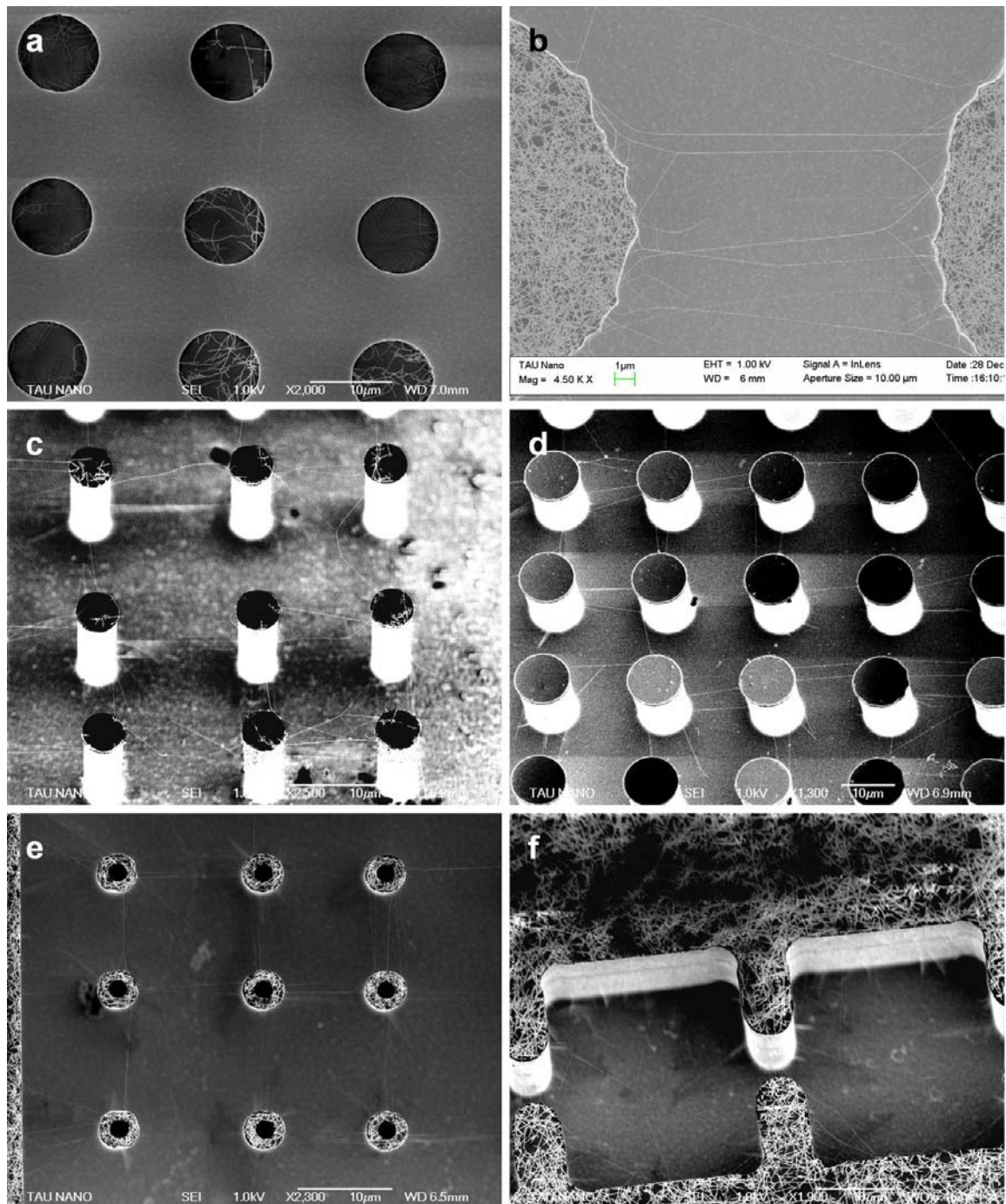


**Figure 34: Suspended SWCNT networks**

Images taken from above, and at an angle, using the HRSEM. (a) An older result showing low yield both on the pillars, and in between. (b) Extremely high yield between large pillar tops. (c-f) Typical yields using the improved protocol. Images show both pillars, of various sizes, and teeth-like structures. Image (d) was taken after sputtering a thin layer of Cr on the substrate, for improved visual contrast.

Figure 34 displays some of the results of suspended SWCNT formation. Figure 34a displays an older, negative result, where very few SWCNTs appear both on the pillars, or suspended in between. The rest of the images used the improved growth protocol, with high yields of SWCNT growth. The difficulty in imaging suspended SWCNTs, as described before, manifests itself in the difficulty in seeing some of the suspended nanotubes. In order to improve suspended nanotube imaging, one substrate

was coated with a thin sputtered layer of Cr, as shown in Figure 34d. While the contrast is improved, the downside to this method is that the nanotubes could no longer be used for stamping. A short note regarding the black “holes” seen in Figure 34e: these are in fact holes, created by the DRIE process, and are a result of non-uniform thickness of the PR patterns on the substrate during both the RIE and DRIE.

It can conclusively be said that the yields reported by us are the highest ever reported for suspended nanotube growth between pillars. In fact, the yield is so high, with sometimes quite a few parallel nanotubes bridging between neighboring pillars, that the transferring of such a large number of SWNCTs poses a problem for their integration in individually isolated CNT based devices. Yet, the most important advantage garnered in using this liquid-catalyst method is that the pillar tops are almost completely smooth after the CVD growth – other than the minute topography created by the nanotubes laying on the pillar top surfaces, as well as stray catalyst particles. This nano-topographic situation is critical in the stamping process, and will not work for suspended nanotube networks created by evaporating thick layers of catalytic materials on the pillar tops.

The suspended nanotube growth, vital to this thesis, is unique in that it forms highly orientated, long, straight SWCNTs, whose position is a result of the geometry of the original pillars. Some gas-flow orientation was seen (as will be described again later), accordingly, the samples were always placed in the tube furnace so that the gas flow was aligned with one axis of the pillar array.

## **6.3 *Suspended Nanotube Analysis***

### **6.3.1 Imaging Analysis**

Viewing the incredibly straight, long and taut nanotube arrays presented both in the images from my work, and in the previous work presented in the literature, one can wonder at the origins of such a finely-knit network. If the previously described growth models are correct, with the nanotubes growing off each pillar, waving around in the thermal breeze, until they hit an adjoining pillar, to which they then stick; then why is there no *slack* in the suspended nanotubes? This question, posed as one of the “objectives” of this research, was answered by us in Ref. [90]. This section is self-contained, and summarizes the cited paper. In addition, further quantitative analysis results are presented here.

The answer to this question, which is described at length in the cited paper, and reiterated below, is that the tubes grow from pillar to pillar, and attach on contact, but then, the short range van der Waals (vdW) forces come into play, causing the nanotubes to “zipper”. These forces were denoted as the tube-tube interactions (TTI), and tube-surface interactions (TSI). These two forces become quite strong at the nano-scale, when the range of vdW is of the same magnitude as the dimensions of the system. The two forces, working in tandem, prevent any slack from appearing in the suspended nanotube after the growth process. In fact, these vdW interactions are apparently strong enough to cause the nanotubes to buckle under the strain.



Analyzing this problem utilizing only the HRSEM images of pillars is very limiting, thus, the growth of SWCNTs on the TEM nitride grids described before was used as well. It was found that suspended networks of taut SWCNTs were also created over the holes in these nitride grids, and therefore, the TEM analysis of these two systems would be equivalent, as demonstrated in Figure 35. These grids were also essential in analyzing the close-ups of the suspended nanotubes, as the resolution of the TEM is several magnitudes higher than the HRSEM, allowing precise measurements of the SWCNT diameters. Furthermore, the ability to view  $\sim 1\text{-}4$  nm diameter nanotubes over the holes in the grid at low magnification in the TEM, as in Figure 35b, simplified the matter of finding the SWCNTs and zooming into the junction points between two individual nanotubes. The reason the SWCNTs can be seen at such low magnification (e.g.  $\times 500$ , which is even better than the capabilities of the HRSEM) is due to the Fresnel fringes caused by the diffraction of the electron beam off each strand of nanotube.

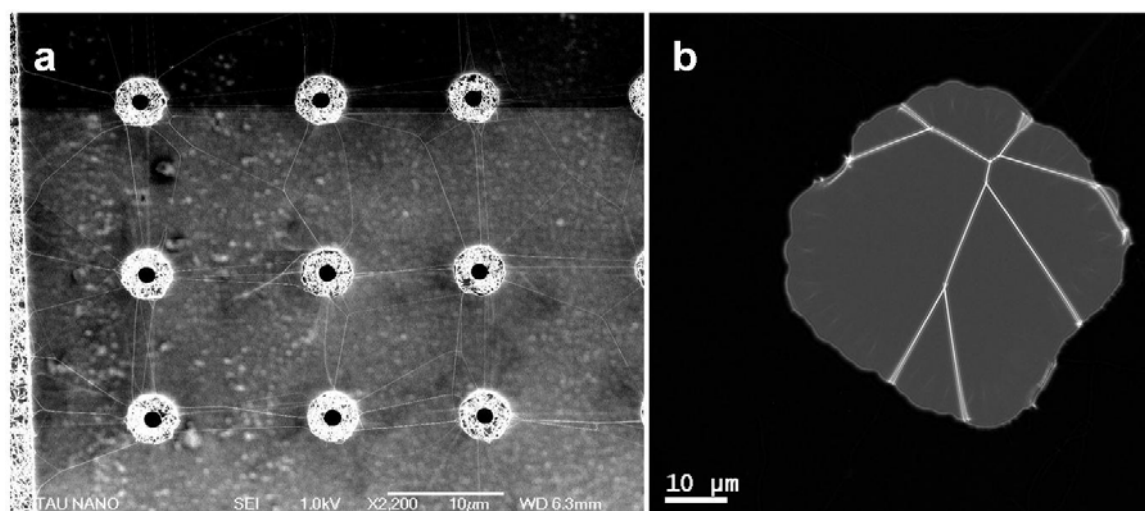


**Figure 35: Comparison of HRSEM and TEM Images of Suspended Growth**

(a) Top-down HRSEM image of a dense network of nanotubes between silicon pillars. Various cross-links can be seen between the pillars. (b) Low magnification TEM image of nanotubes over a  $40\text{ }\mu\text{m}$  hole in a nitride grid. Complex cross-linking can be seen here, too. In both images, the nanotubes are completely taut.

While the two forces/interactions work together to form the taut networks, it is best analyze the two separately. Beginning with the TTI, we will begin with a theoretical case study of two SWCNTs that grew across the gap between two pillars, leaving behind a fair bit of slack, as depicted in Figure 36a. Since this is all occurring at high temperatures, the nanotubes still vacillate due to the thermal energy, and statistically, the two nanotubes will touch at some point along their lengths (this point will of course determine the shape of the resulting bundle). The TTI will cause the pair of nanotubes to adhere (Figure 36b), and then zip-up as much as possible, until a (bundled) length of taut nanotubes is obtained (Figure 36c). Actual HRSEM and TEM images were used to verify this model.

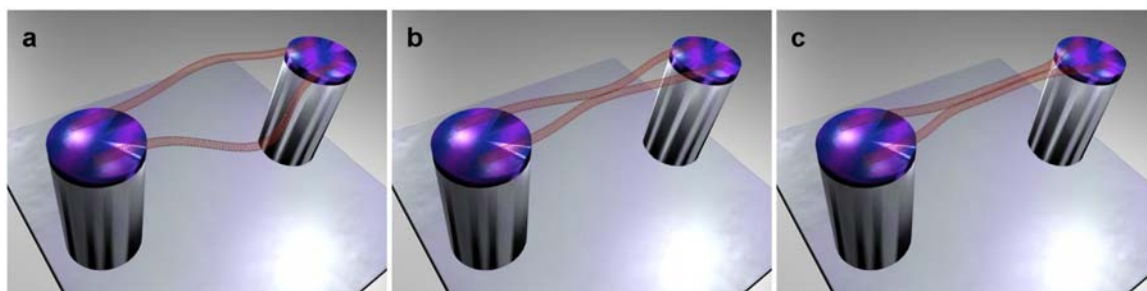


**Figure 36: Tube-Tube Zipper-Effect Model**

Images are renderings only. (a) Two nanotubes bridging between adjacent pillars, with a fair amount of slack. (b) The two tubes come in contact, and bind to each other. (c) The binding energy causes a zipper-effect, removing all slack sections.

At the junction points with the pillars, “Y-junctions” would then be visible in this type of formative process. These y-junctions would only be discernable as consisting of more than one nanotube in the TEM images, while in the HRSEM images they will merely appear as a white line. This is displayed in the two HRSEM images in Figure 37. In Figure 37a, many y-junctions can be seen extending off the top of one of the pillars. The angles between the nanotubes suggests that some of them may have buckled as a consequence of the interactions, however, the HRSEM images do not have the resolution to validate such buckling. Figure 37b displays a much larger configuration with a y-junction appearing in between an array of pillars. Despite the large scale of this y-junction, the nanotubes are visibly taut, with no detectable oscillations. The TEM images have a greater resolving power, thus, the exact nature of some of these bundles could be viewed. When zooming into the intersection points of the cross-linking nanotubes in the grids (as in Figure 35b), the nanotubes comprising the y-junctions could be seen in detail. Sometimes, there were surprising results, such as the configuration presented in Figure 35c, where, from afar, it appeared to be a simple y-junction, but when viewed at higher magnifications, actually turned out to be a conjoining of three SWCNTs, creating a triple-y-junction. This formation is so small, that it would only appear as a pixel in most HRSEM images, hiding the true nature of such a junction. The top SWCNT in this image can be seen to buckle at both junction points (close up shown in Appendix 9), due to the strong interactions of such a configuration. Figure 37d displays a typical y-junction off of the nitride grid. This image is distinct from the one presented in Figure 37a; here as well, it is so small that it would have appeared as a mere pixel in the HRSEM images. The final zipper-effect configuration is distinctly visible in both of these images. Finally, Figure 37e exhibits the complexity of such tube-tube formations, with a single small nanotube wrapping around a much larger one, over the course of several hundred nanometers (actually, over a micron, not shown).



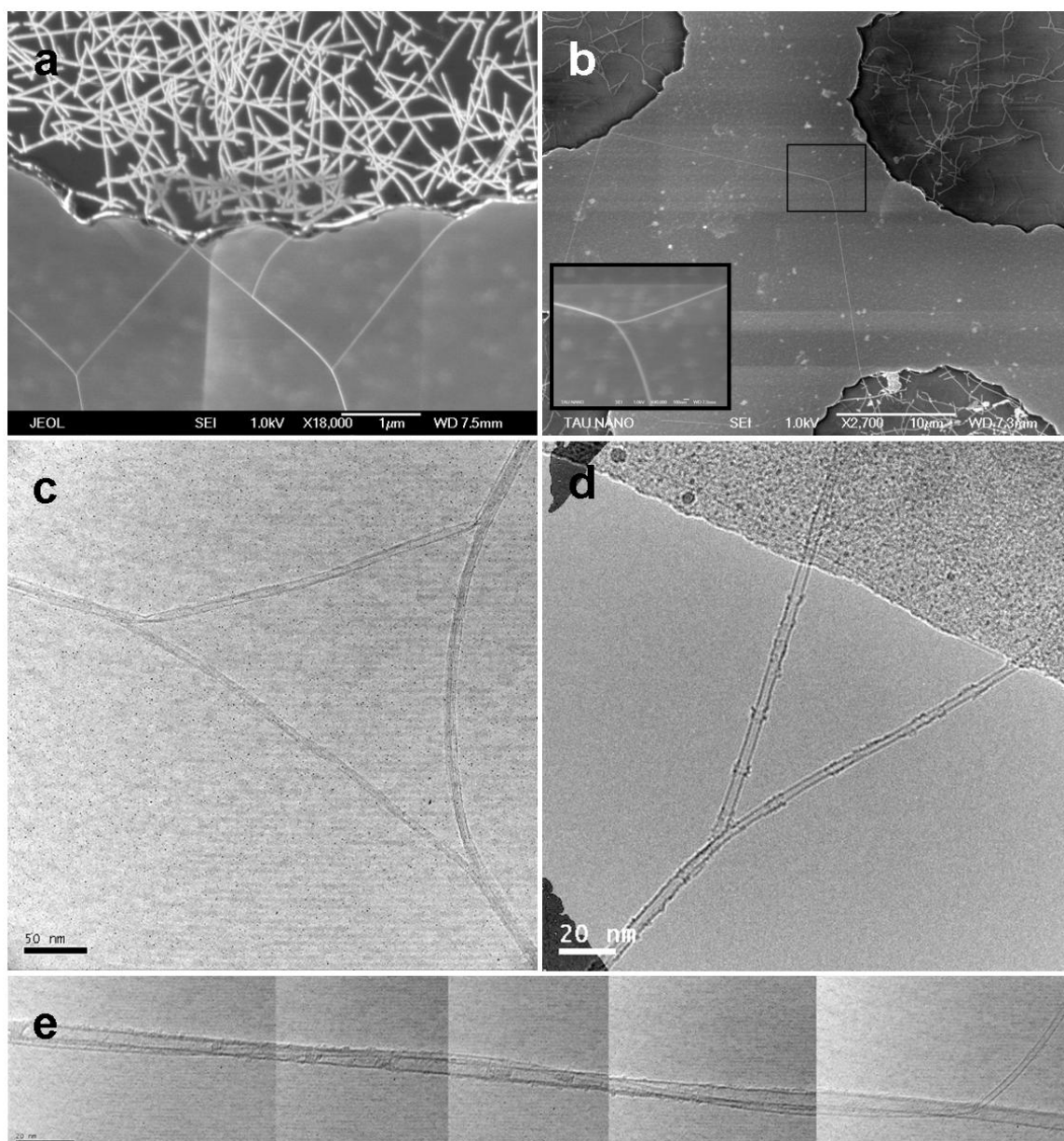


**Figure 37: Tube-Tube Interaction Images**

(a) HRSEM image of many y-junctions leading off a pillar top. (b) An HRSEM image of a nanotube network between neighboring pillars with a y-junction formed in between. Inset is a close up of the y-junction. (c-e) TEM images: (c) A complex triple-y-junction configuration created by three SWCNTs. The top strand of the formation has buckled at the two junction points. (d) A typical, small y-junction leading off the TEM nitride grid. (e) A mosaic of images displaying a tiny ~1 nm nanotube wrapping around a larger one (seen at the far right), creating a periodic twirl over the course of hundreds of nanometers (scale bar here: 20 nm)

The model described above is just one of the models that can describe the resulting formation. Before moving on to the TSI, it should be noted that the model presented in Figure 36 is only a conceptual one. Another model can be used wherein a single nanotube bridges the gap, and then a shorter one binds to it, again causing the zipper-effect, but not actually reaching the other side. Examples of this, with one SWCNT “ending” midway along the length of the bridging SWCNT were seen in the TEM images (an example of which is shown in Appendix 9).

The other force driving the zipper-effect causing the taut network formation is the TSI. The binding forces between the tube and surface are also controlled by vdW. An exemplifying model is depicted in Figure 38. Here, a slack SWCNT suspended between two pillars becomes taut when the slack segments adhere to as much of the pillar tops as possible, leaving a single, taut nanotube. This effect explains the tautness seen in many of the SWCNTs that have no y-junctions at their end.

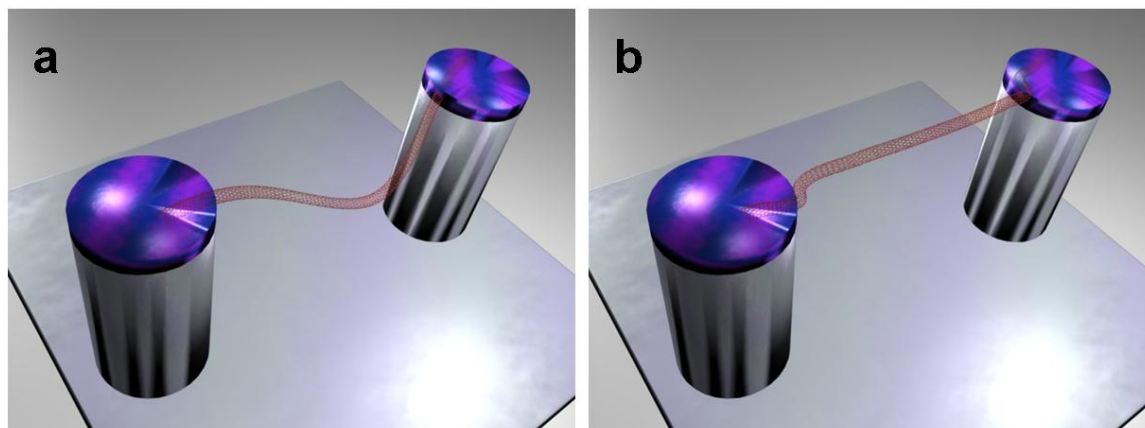


**Figure 38: Tube-Surface Zipper-Effect Model**

Images are renderings only. (a) A single SWCNT suspended between adjacent pillars, with slack. (b) The final configuration, with the spare nanotube slack adhering to the edges of the pillar tops.

Images demonstrating the TSI are presented in Figure 39. Figure 39a displays a typical close up of a SWCNT growing off a pillar top, and following the serrated-like features (an artifact from the low resolution masks used for photo-lithography). Perhaps a more compelling image is displayed in Figure 39b. Here, the pillars were only 8  $\mu\text{m}$  high (one of the earlier attempts), and therefore, the bridging nanotube (over a  $\sim 20 \mu\text{m}$  gap) had enough slack to hit the bottom of the substrate (Si), and adhere to it. While the segments of SWCNT leading from the pillar tops to the substrate may not be visible in this printed version of the image, the segment adhering to the surface (as denoted by the two white arrows) is distinctly evident. This is due to the difference between SWCNTs on a surface, and suspended, as described before, and well demonstrated here. The TEM images (Figure 39c, d) also provide compelling evidence of this interaction, many examples of SWCNTs adhering to as much of the nitride grid as possible, before being suspended over the holes, were seen. Figure 39d provides one of the best examples of this, demonstrating the contour following of the SWCNT.

These two interactions obviously work simultaneously on a SWCNT, creating the taut network formation. Close-up images of most y-junctions will also display TSI parts. The contour following of the SWCNTs due to the TSI lead to the conclusion that *circular* pillar tops were the most advantageous for creating taut networks. Since the nanotubes extend off the pillar tops at random angles, creating a sharply knit suspended nanotube between two adjoining pillars that will best utilize the TSI would require the pillar edges to have the lowest angle possible between the angle extended between the nanotube and the contour of the pillar top. Circular pillar tops thus fulfill this demand for low tangential angles. (An example of a triangular pillar top

arrangement is shown in Appendix 9, demonstrating the lack of tautness in some of the nanotubes).

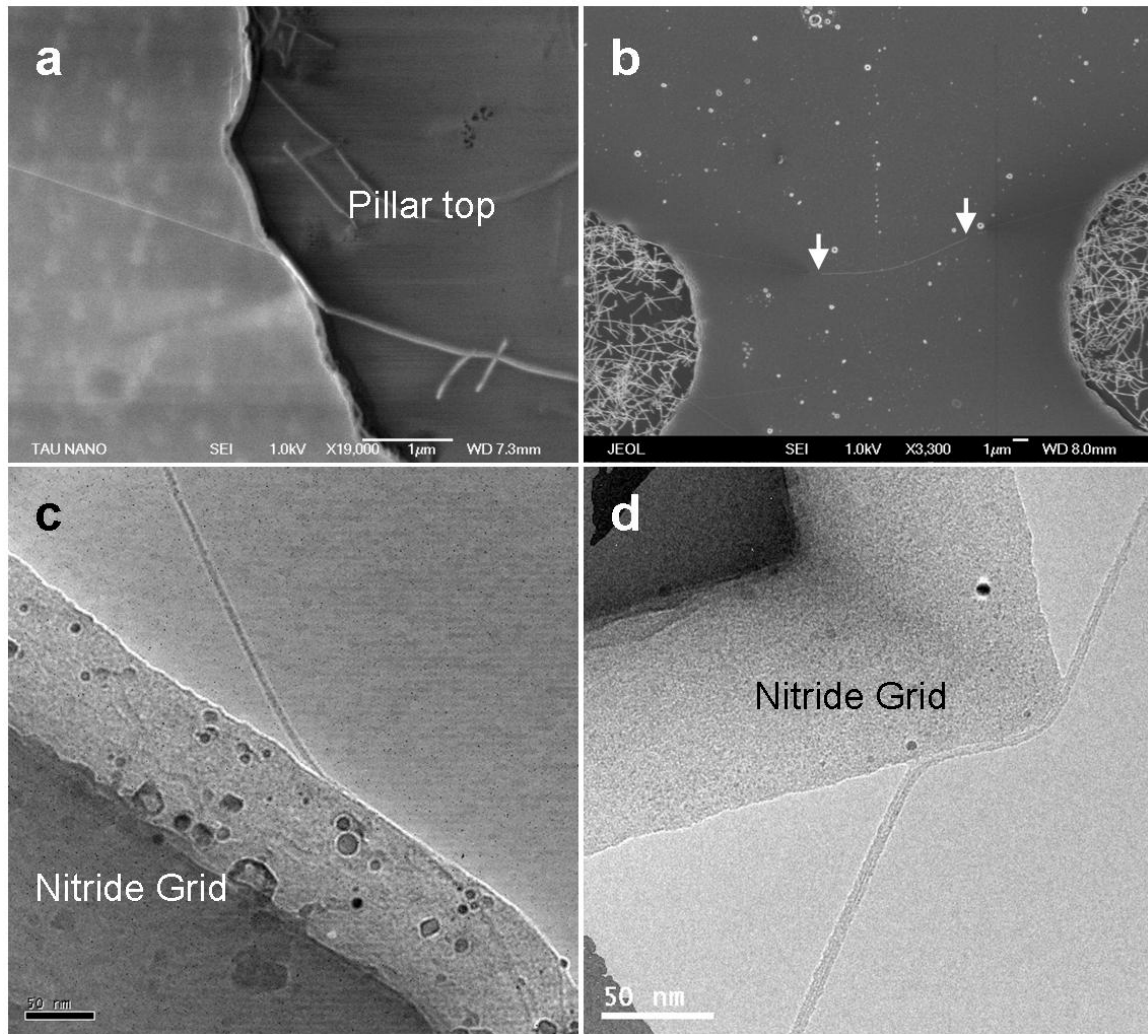


**Figure 39: Tube-Surface Interaction Images**

(a) HRSEM image of a nanotube following the contours of the pillar top, removing slack segments. (b) A nanotube between pillars with enough slack to reach the bottom, and can be seen adhering to the floor (between the two arrows). (c-d) TEM images of SWCNTs adhering to the edge of the nitride grid.

Before continuing to more quantitative analyses of these interactions, it should be noted that there is some discussion regarding the source of the interactions themselves. While I have claimed that these are vdW derived interactions, they may actually be caused by the  $\pi$ -bonds of the graphene sheet, which are already hybridized due to the wrapping of the nanotube wall, interacting with the hybridized  $\pi$ -bonds of a nearby nanotube. This extremely close range interaction is in actuality a form of *covalent* bonding, and not the usual vdW force [97]. Finally, the results presented here should be compared to those published at nearly the same time in Ref. [88], and described previously. The conclusions of that paper and ours are nearly identical in terms of the TTI, but, in Ref. [88], there is no mention of the TSI. In addition, the simplicity of the analysis here is in my opinion preferable, due to the range of interactions viewable, the usage of TEM analysis compared to SEM analysis and in the simplicity of our described method.

### 6.3.2 Quantitative Analysis

The adhesion of the SWCNTs to each other in the formation of bundles has been analyzed by many (see Ref. [90] for citations), however, one particular analyses was found to be quite pertinent to these images, where a single image of a nanotube pair was imaged (TEM), and an attempt at analyzing the binding energy between the nanotubes was made. Chen *et al.* [98] showed how one can take the case of two parallel CNTs being pulled apart to the point where the binding energy between the two tubes is equal to the elastic energy spent on bending the tubes from their straight, "rest position". The CNTs are modeled as tubular beams, as will be elaborated upon presently. The formula used in Ref. [98] for the free energy,  $F$ , of the system is:

$$F = \frac{4EI}{l} \left( \theta^2 - 3\theta \frac{\Delta}{l} + 3 \frac{\Delta^2}{l^2} \right) + \gamma l \quad (14)$$

with  $\Delta$  being the distance between the two bound ends,  $l$ , the distance from the y-junction to the binding site,  $\theta$ , the angle extended between the deflected tubes and  $\gamma$ , the binding energy per unit length. The parameter  $EI$  is the bending stiffness, or, flexural rigidity, of a tubular beam, and is given by the Young's modulus and moment of inertia for a hollow-beam CNT:

$$E \cdot I = E \cdot \frac{\pi}{64} [d^4 - (d - 2t)^4] \quad (15)$$

with  $E$  being the Young's modulus of a CNT (undervalued at approximately 1 TPa),  $I$ , the moment of inertia,  $d$ , the outer diameter, and  $t$ , the wall thickness of the nanotube. A better, more precise formula than that given in the equation for the free energy above would take into consideration the asymmetries in the configuration described (see Figure 40a). If the two nanotubes are not identical, then the formula would be:

$$F = \sum_i \frac{2 \cdot (EI)_i}{l} \left( \theta_i^2 - 3\theta_i \frac{\Delta_i}{l_i} + 3 \frac{\Delta_i^2}{l_i^2} \right) + \gamma_i l \quad (16)$$

The modifications to the formula in the summation index,  $i$ , which takes into account the asymmetry of the situation depicted in Figure 40a, and shown for an actual image in Figure 40b. In the symmetric case, the angles of deflection,  $\theta$ , and deflection  $\Delta$ , are equivalent. In either case, the length,  $l$ , is a constant of the system being measured. The binding energy,  $\gamma$ , is taken as a constant in the case we are to analyze for the simple reason that the two tubes appearing in Figure 40b are of nearly identical dimensions. The measurements on the image were made using the software described before, and allowed the measurements of both angles and lengths.

To find both the binding energy, and the deformation energy, one must differentiate the above equation, in respect to  $l$ , the separation length of the parallel tubes, to get:

$$\gamma = \sum_i \frac{2(EI)_i}{l^2} \left( \theta_i - 3 \frac{\Delta_i}{l} \right)^2 \quad (17)$$

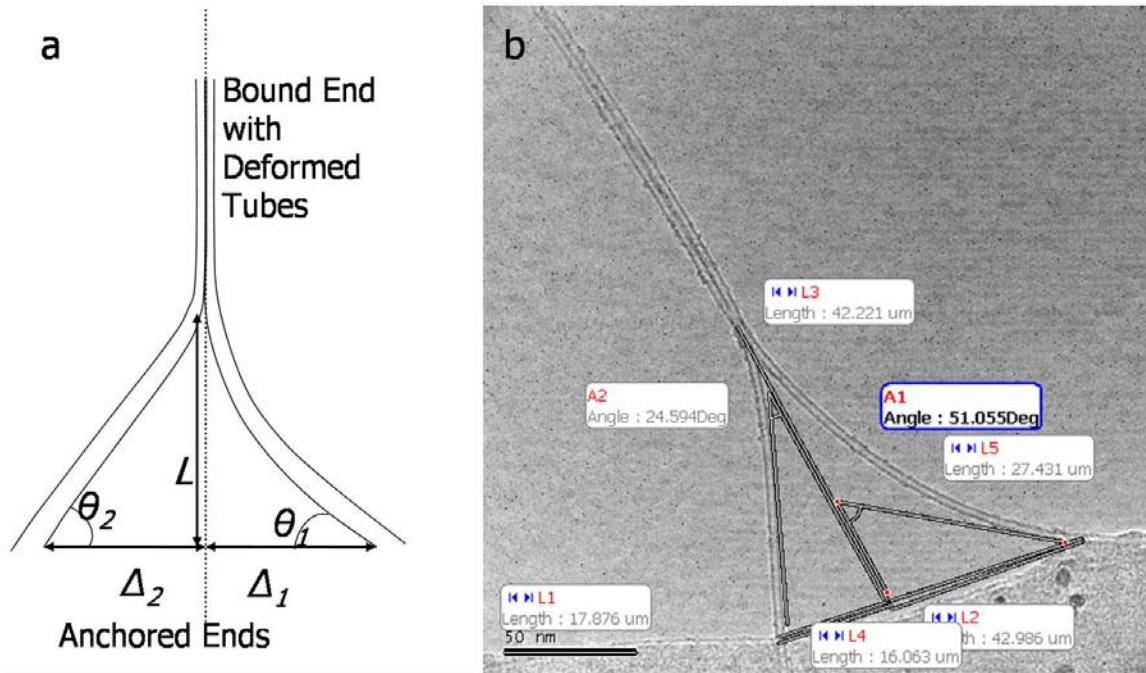


### Figure 40: Binding Energy between Nanotubes

(a) Schematic describing the parameters for the equations in the text, for the asymmetrical case. (b) Image of a y-junction, with some of the measurements, using the software described in the text.

This formula was used by Chen *et al.* to calculate a binding energy of 0.36 nN. Using the sample in Figure 40b, (using a diameter of  $\sim 3.5$  nm, and considering that it is a double-walled nanotube, with:  $t = 2t_{\text{graphene}} = 0.72$  nm) we received a value of  $\gamma \equiv \underline{0.8-1.6 \text{ nN}}$  (the range corresponds to the error value, as will be discussed).

In order to compare these measurements to simulated ones, one must first convert these findings to units of  $\text{eV}/\text{\AA}$  (another standard unit used for Binding Energy), in which case  $0.36 \text{ nN}$  becomes  $0.225 \text{ eV}/\text{\AA}$ , and  $1.6 \text{ nN}$  (the higher of our assessed value) becomes  $1 \text{ eV}/\text{\AA}$ . These will be compared to some simulated results in the literature, specifically, Refs. [99] and [100]. Reference [99] estimates a binding energy of  $\sim 0.6 \text{ eV}/\text{\AA}$  for a SWCNT with a diameter of  $\sim 3.5 \text{ nm}$ . This value should be attenuated by the fact that the nanotube in Figure 40b is a double-walled CNT to approximately  $\sim 0.5 \text{ eV}/\text{\AA}$ . The lowering of this figure is done in relation to their calculation of the lowering of the binding energy of a (40,40) double-walled CNT. This value is comparable to that of Ref. [100], which takes a strongly deformed nanotube's wall as being similar to a layer of graphene, with an adhesion energy of  $W_{flat} = 0.4 \text{ J/m}^2$ , correlating to  $0.025 \text{ eV}/\text{\AA}^2$ . A rough estimate will assume that the contact layer, after deformation, between the two tube walls of  $1\text{-}2 \text{ nm}$ ; multiplying these results gives a value of  $0.25\text{-}0.5 \text{ eV}/\text{\AA}$ . The correlation between two such estimates substantiates the calculated value.

The possible error values in these measurements were not taken into account in Ref. [98]. This is of critical importance when considering the variables of the last three equations. Specifically, the diameters of the tube,  $d$  (whether single or double-walled CNTs), and the separation length,  $l$ , highly affect the calculated value to an extent that even a 10% error value in these parameters can lead to an order-of-magnitude difference in  $\gamma$ , the binding energy. Additionally, the value for the Young's modulus



was taken to be 1 TPa, which is a lower bound. Here, it is assumed that the Young's modulus does not change by more than 25%, to 1.25TPa, as a function of tube diameter [101]. In addition, the calculation in Ref. [98] did not take into account the deformation energy of each nanotube, as will be described in the next section.

A final note regarding the buckling of the nanotubes: As discussed in our paper, the buckling of a nanotube is a matter of the critical stress that can be placed on a tube. This stress is inversely proportional to the diameter of the tube, [ $\sigma_{crit} \sim 1/r$ ], which is precisely what we found after analyzing many of the TEM images. Larger nanotubes were more susceptible to buckling, and bundles of SWCNTs were even less susceptible to buckling, due to the increased strength of the bundle.

The analysis of the TSI and TTI is important not only in understanding the cause for the taut network formation, but also in enabling the capability to control such formations. The conjecture regarding the use of circular pillar tops to obtain the best taut network, instead of other geometries, is such an applicative conclusion. Further research on the binding energy between nanotubes, which include course-graining simulative models involving segments of adhering nanotubes are currently underway in our lab.

## 6.4 TEM Analysis of Individual SWCNTs

The method of using the TEM nitride grids as templates for CVD growth, with the SWCNTs growing over the holes in the grid, also allowed the analysis of several other phenomena that were inspected by us. These were published in Refs. [92] and [93], and a cursory summary of them will be presented here.

The major advantage imparted by the use of these nitride grids is that they both withstand the temperatures of the CVD process, but more importantly, they permit the highest contrast possible with a TEM due to the lack of background noise when viewing over the holes. Imaging the SWCNTs over these holes allowed us to view some well known features of nanotubes that were nevertheless almost never actually seen before. These included the radial deformation of SWCNTs (with the capabilities of measuring the deformations *directly*), many mechanical defects, such as buckling and twisting, as well as actively degrading the tubular structure by electron irradiation.

### 6.4.1 Radial Deformation

The radial deformation of nanotubes caused by their adhesion to another surface or nanotube, was a well documented phenomenon (see cited references in [93]), yet the method of experimentally measuring such a deformation had only been implemented for MWCNTs using the TEM [102], and with an AFM for SWCNTs. Using an AFM tip to measure such minute variations in the diameter of a single SWCNT is problematic, since it includes the actual shape of the AFM tip, and the final measurement must include the deconvolution of the tip shape and the measurement [99]. This *indirect* measurement is problematic in that respect, but is also limited to measuring the deformation of nanotubes on a surface only. SWCNTs lying on a

surface not only deform, but also occasionally completely collapse, leaving a flattened tubular structure. Using our specially prepared CNTs on the TEM grids allows the deformation to be measured *directly*, with sub-nanometer resolution, as well as permitting the measurement of tube-tube deformations.

The images in Figure 41 were taken directly from our cited paper (Ref. [93]). In Figure 41a, the SWCNT can be seen to deform in two different directions as a result of its interaction with the underlying CNT bundle. The direction of the interaction, i.e. from below or to the side, directly corresponds to the direction of the deformation. Note that this 5.1 nm SWCNT is quite large, and from the deformation apparent in this image, it is *not* a collapsed tube. This image is actually one of the only visual presentations of such a large diameter SWCNT. The image in Figure 41b shows a double-walled CNT undergoing a radial deformation, as well as the other tube buckling due to the TTI described before. The buckled CNT undergoes a relatively large deformation, and appears to have flattened out at the right hand side, as described in our paper. Finally the results were compiled and compared to the simulated results of Ref. [99], which described the tube-surface related deformations, and appears as the graph in Figure 41c. This tube-surface interaction provided an upper bound for our experimental measurements, as the surface area between a SWCNT and a surface is larger than between two nanotubes, and the short range vdW forces should therefore be stronger, producing a higher degree of deformation. The fact that all of our data points lay underneath this calculated limit further corroborated our results.



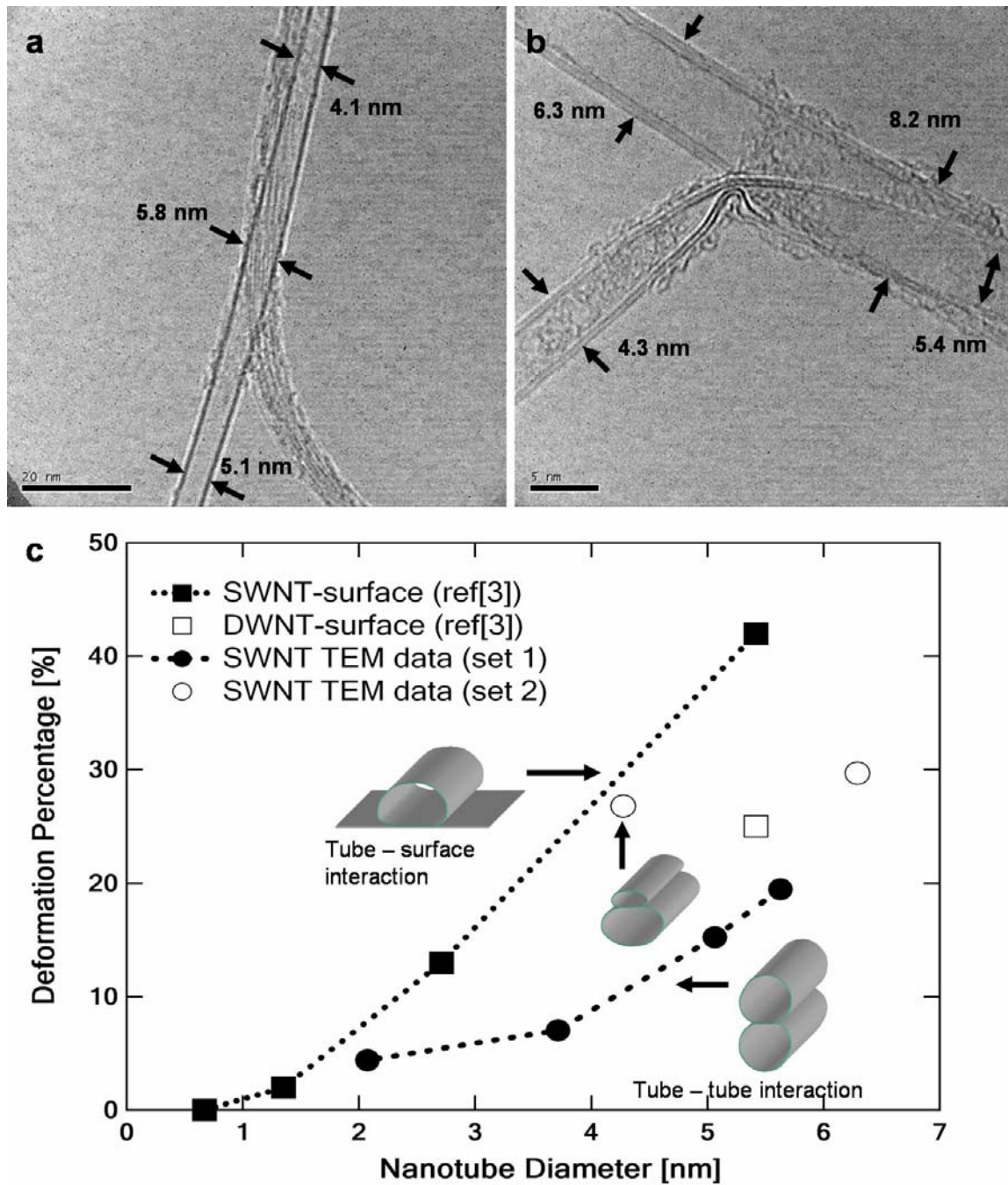


**Figure 41: Radial Deformation Measurements**

(a) Deformation of a single SWCNT in two different directions, due to its interaction with another bundle of nanotubes. (b) A buckled nanotube undergoing a large deformation. (c) The graph from our paper. The sets of data refer to the table provided their, and ref[3] refers to Ref. [99] here.

It should be noted that the deformation energy was *not* taken into account in the previous discussion regarding the binding energy,  $\gamma$ , between two nanotubes (nor was it included in any of our papers). In fact, the results of the calculated binding energies before can give an estimate of the deformation energy,  $D$ , of CNTs. However, it must be stated that these values are diameter dependant:

$$\gamma + D = \text{func}(\text{diameter}, \# \text{CNT walls})$$

(18)

From the simulated results, it is known that nanotubes of smaller radii deform less. Calculating the deformation energy is therefore a question of the interplay between the two energies. If we are to take the calculated (simulation) values of the binding energy, per diameter (noted in the previous section), as essentially correct, then the difference between the measured values of  $\gamma + D$  and the estimated value of  $\gamma$  alone (binding energy), should give an estimated value for the deformation energy,  $D$ . For example, for the  $\sim 3.5$  nm CNT described before, using a binding energy of  $\sim 0.5$  eV/Å, the deformation energy, would be around  $\sim 0.3$  eV/Å, and the value goes to zero for smaller tubes (as it could not be negative). The measured value of  $\gamma = 0.225$  eV/Å measured in Reference [98] is, in our view, *lower* than the actual value, as it does not take the deformation of the CNTs into account, as well as not corresponding to other simulated results. Finally, we also did not take both the functional dependence of  $EI$  on the deformation, nor the extra elastic energy spent on *stretching* the tubes into the configuration they are in. This last term should lower the fraction of the energy calculated for just the deformation of the tubes even more.

### 6.4.2 Twisting and Melting

Several other systems were viewable by using this method of combining the *in situ* growth of CNTs directly onto the TEM grids (Ref. [92]). Two of them will be briefly described here.

One interesting feature discussed in our paper was the twisting of a single SWCNT, and, due to the unique capabilities imparted by the method, the ability to precisely measure the deformation of the SWCNT under such a deformation. Figure 42a shows such a twisted SWCNT. The diameter of the SWCNT was  $\sim 4.2$  nm (as measured far from the twisted segment), and a measurement of the exact deformation caused by the twisting is presented in Figure 42b. Here, the sub-nanometer measurements give an exact picture of the change in diameter in the tubular structure.

Additionally, viewing the CNTs in the TEM, over a hole, for over a minute causes the irradiation of the nanotubes, and their denaturing. This can be described as "active analysis" of the CNTs. This was shown for a buckled nanotube (exemplifying the TSI) in Figure 42c-e. The nanotube not only "stuck" more to the surface as a result of the irradiation, but also became amorphous, appearing to become a wire consisting of sheets of graphene, as seen by the atomic planes in Figure 42c. Figure 42e also shows the results of prolonged viewing of SWCNTs over the hole in the grid. Here, the twisted tube shown in Figure 42a was destroyed due to the irradiation of the electron beam. The cross-over points can no longer be seen, and the tubular structure apparently became an amorphous wire.

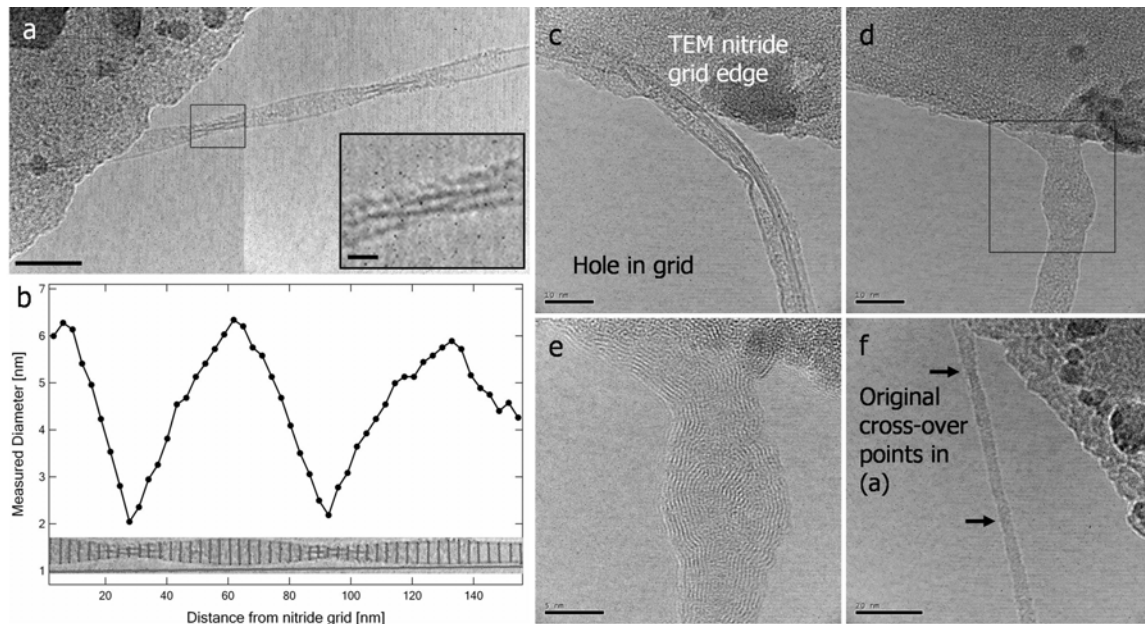


**Figure 42: TEM Measurements of Twisting and Irradiation**

(a) A twisted SWCNT off the edge of the nitride grid; scale bar: 20 nm (inset: a close-up of the crossover point; scale bar: 2 nm). (b) Measurement of diameter of the twisted SWCNT. The data points correspond to the measured lines in the inset below. (c-e) The effects of irradiating a nanotube with the electron beam. The buckled tube in (c) became an amorphous mass in (e) after a minute of high energy irradiation. (f) The effects of irradiation on the twisted tube in (a). The cross-over points are no longer visible due to the nanotube's denaturing.

## 6.5 Raman Spectroscopy Mapping

We now return to the SWCNT networks between pillars. To characterize the formed networks of SWCNTs, a method of RS mapping was implemented, as described in the previous chapter. Samples with suspended networks were raster-scanned over the course of a few  $\mu\text{m}^2$  with a Raman laser, which was attached to a computer system that searched for the G-band peak, at  $1594\text{ cm}^{-1}$ . The mapping of each pixel (corresponding usually to an area of  $0.5 \times 0.5\text{ }\mu\text{m}^2$ ) was then related by the computer into a color-coded two-dimensional drawing. Figure 43a portrays an HRSEM, top-down, image of a suspended CNT network, with a black square demarcating the area that was Raman-scanned. In Figure 43b, a mapping of this region is shown, with a brighter pixel signifying a stronger G-band peak in the spectrum. The darker, circular areas seen in the lower right correspond to the pillar tops, which have few nanotubes on them, as well as giving off a weaker signal than the suspended segments (as was described in the Literature Review section). The two images were superimposed in Figure 43c, using an isometric view for clarity of the pillars. The correlation between suspended nanotubes and RS signal is distinctly evident. Another type of RS mapping can also be used, in which one scans in one direction only are done, giving a one-dimensional mapping. This method is ideal if only information regarding the suspended regions of nanotubes is of interest, as is in the case of the stamping of the suspended segments described in this thesis. Figure 43d displays such a line-mapping, with the width of the line being  $0.5\text{ }\mu\text{m}$ , corresponding to the diameter of the RS laser. Again, the correlation between suspended segments and intensity of the RS signal is

apparent. A small artifact that can be seen in this image is the spreading of the signal at the top of the line (see arrow). This is due to a SWCNT that was out of the focal plane of the laser (focused on the plane of the pillar tops), creating an artificially large signal due to the spreading of the laser. This was verified in an isometric image of the pillars (not shown), showing the bottom SWCNT as growing off one of the pillars, and hitting the side of the adjacent pillar. These SWCNTs, which are not on the same plane as the pillar tops, are not as important for the following stamping step, since they should not be stamped along with the other suspended nanotubes.

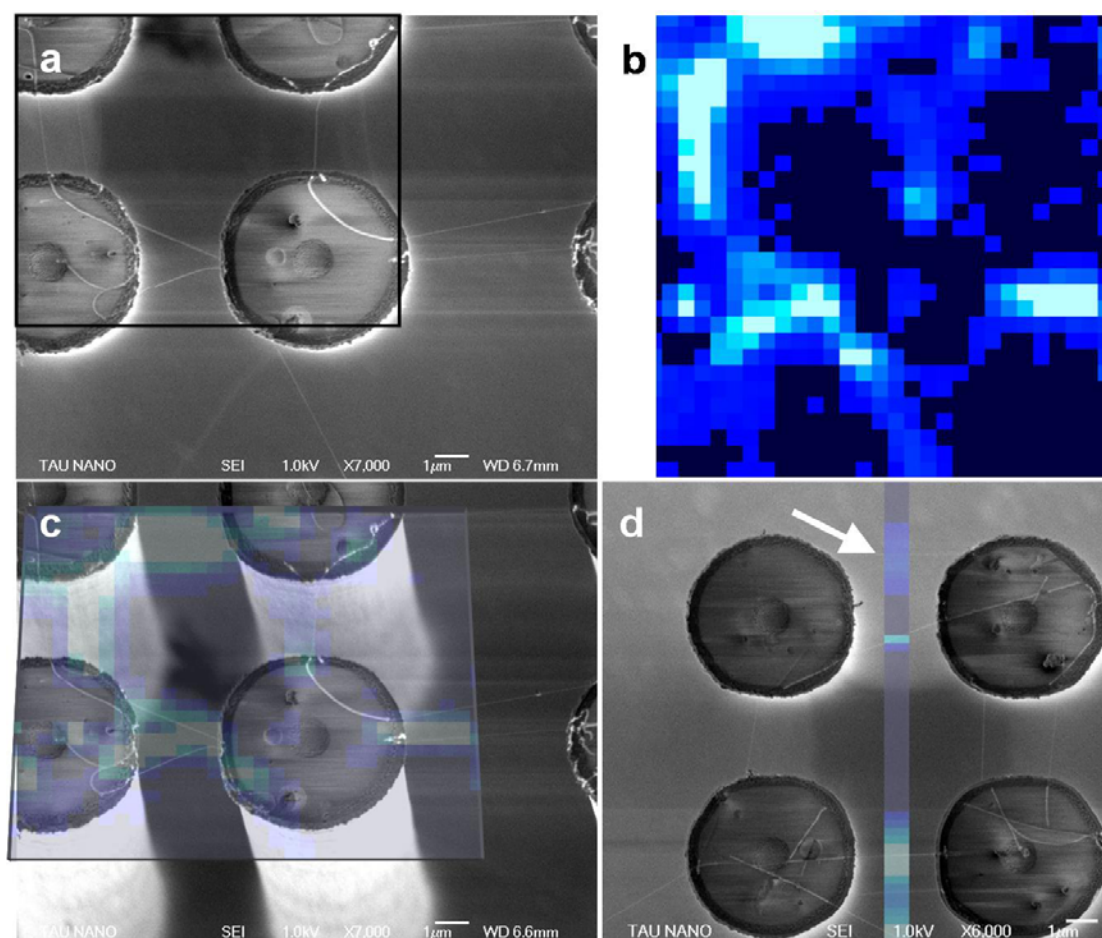


**Figure 43: Raman Mapping Images**

(a) HRSEM image of nanotubes between pillars. The black box signifies the area that was mapped. (b) Raman mapping with brighter pixels signifying a stronger G-band signal. (c) Overlapping images with the semi-transparent Raman mapping placed directly on an image of the pillars. (d) A line-mapping, with a 0.5  $\mu\text{m}$  wide line in one direction. The arrow points to the spreading of the signal due to the nanotube being out of focus.

Improving the resolution of the mapping to pixels with smaller sizes (as in Figure 44a, with 0.2  $\mu\text{m}$  per pixel) is still limited by the diameter of the laser spot. This figure also emphasizes the difference in signal between suspended segments of SWCNT, which results in the bright signal from the RS mapping, and the segments adhering to the  $\text{SiO}_2$  substrate. The bottom right side of the inset in Figure 44a barely registers the existence of the nanotubes on the surface, while the suspended segment is brightly displayed.

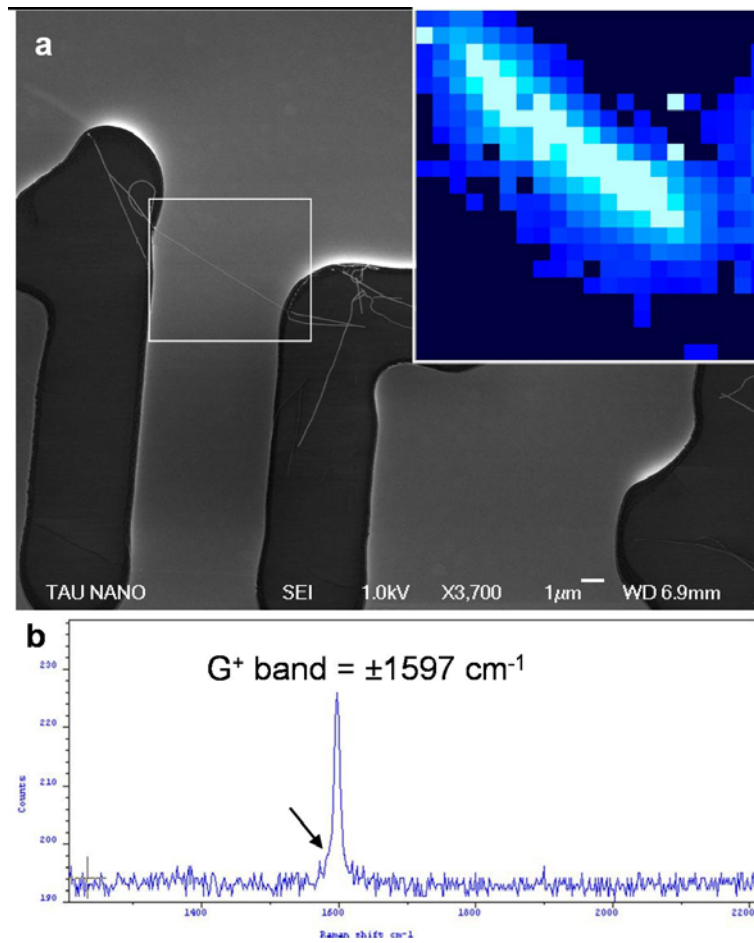


**Figure 44: Intensity of Suspended Raman Signal**

(a) HRSEM image of a suspended nanotube and demarcated mapping area. Inset: Raman mapping with a higher pixel resolution (2  $\mu\text{m}$  per pixel). (b) A single spectrum taken from one of the pixels of a suspended nanotube. The arrow points to the kink on the left side of the G-band, as described in the text.

Although a mapping of the RBM band would give the most vital structure-specific information, the G-band can be used for this purpose as well. As described in the Literature Review, a correlation between the diameter of the nanotube and the internal shifts and broadening of the G-band exists as well. For nanotubes over  $\sim 1.5$  nm, the shift between the  $\omega_{+G}$  and  $\omega_{-G}$  is so small, that it merely results in a broadening of the single  $\omega_{+G}$  band. If one looks closely at the peak appearing in Figure 44b, one can see a slight asymmetry in the peak, with a broadening to the left, as expected. Using this equation, with the constant  $C$  taken as  $-45.7 \text{ cm}^{-2}$  (for semi-conducting nanotubes),  $\omega_{+G}$  as the constant G-band peak (which here is at  $1597 \text{ cm}^{-1}$ ), and  $\omega_{-G}$  as the splitting of the peak to the left of the original G-band peak, allowed us to determine the approximate SWCNT width of  $\sim 2.5$  nm for the nanotube depicted in the spectrum of Figure 44b.

The RS method described here can be used as a way to scan all the suspended nanotubes between the pillars, imparting precise structural (and, therefore, electronic) properties of each SWCNT. If the line-scan method is used, then one only needs to scan the areas between pillars, which are spatially well-defined, to obtain this information. Incorporating the RS mapping into the stamping procedure, as described by us in Ref. [91], is an important feature of the method described in this thesis.



## 6.6 Stamping Networks of SWCNTs

The next step in the process flow, the most crucial and innovative, is the stamping of the suspended network of SWCNTs onto another substrate. The theoretical basis for the stamping was previously described, and consists of the preference of a suspended nanotube, when brought into close contact with another substrate (from above/below), to adhere to the new substrate, due to the strong binding energy to the new substrate. Theoretically, only the suspended segments of nanotube should transfer to the new substrate, and the parts on the pillar tops should have almost no preference towards either remaining attached to the SiO<sub>2</sub> pillar tops, or the new surface. This was also the theory posited in Refs. [77,81], and served as a basis for our initial assumptions. In the case of the studies cited in Refs. [81,82], the optimal transfer medium was found to be PMMA (requiring it to be poured, and then cured on the substrate), which was used to “hold the nanotube in place”. However, it eventually turned out that both of these assumptions were unfounded. While we found that a transfer medium was necessary, it turned out to be DI water, and that the nanotubes did not necessarily “break off” the pillar tops.

As stated, many attempts were made at transferring the network of nanotubes from the pillar stamp to other substrates. After a few (failed) attempts, the method tried in Ref. [82] was attempted using PMMA, unsuccessfully. As a result, variations on this method were employed, with varying success. These attempts included the use of a wide range of liquid solvents, namely: acetone, IPA, hexane, methanol, ethanol and DI water. Most of these attempts were made at room temperature, except the case where PMMA was used. Initial attempts to stamp the nanotubes utilized the MJB-3 mask aligner to align the two substrates, as well as bring the two substrates together (along the z-axis) and apply pressure. The source substrate was attached to a transparent flexible slide, with holes drilled near the location the substrate was attached to. Adding the solvents was facilitated by injecting small amounts of liquid in between the two substrates, via the drilled holes, using a syringe. Other attempts simply utilized the manual attachment of the two substrates (without alignment, by simply placing the source on the target with a tweezers). This was done at either room temperature or on a hot plate at temperatures  $\leq 100^{\circ}\text{C}$ .

The results of these initial attempts are displayed in Figure 45. These results are examples of transfers of individual SWCNTs on both Si and SiO<sub>2</sub> substrates, using both hexane and ethanol. These two solvents were found to be the most successful in the initial attempts. In either case, long, straight, completely isolated segments of SWCNTs were found on these surfaces after stamping. These results, proved the concept to be possible, but did not demonstrate large scale transferring of nanotubes from the networks to the target substrates. In some cases, such as in Figure 45a and c, the orientation of the stamped SWCNTs displayed the geometries of the pillars, yet to a low extent only. Note that nanotube transfer was achieved almost only when the samples were heated, thus the methods of alignment using the mask aligner were invalidated.

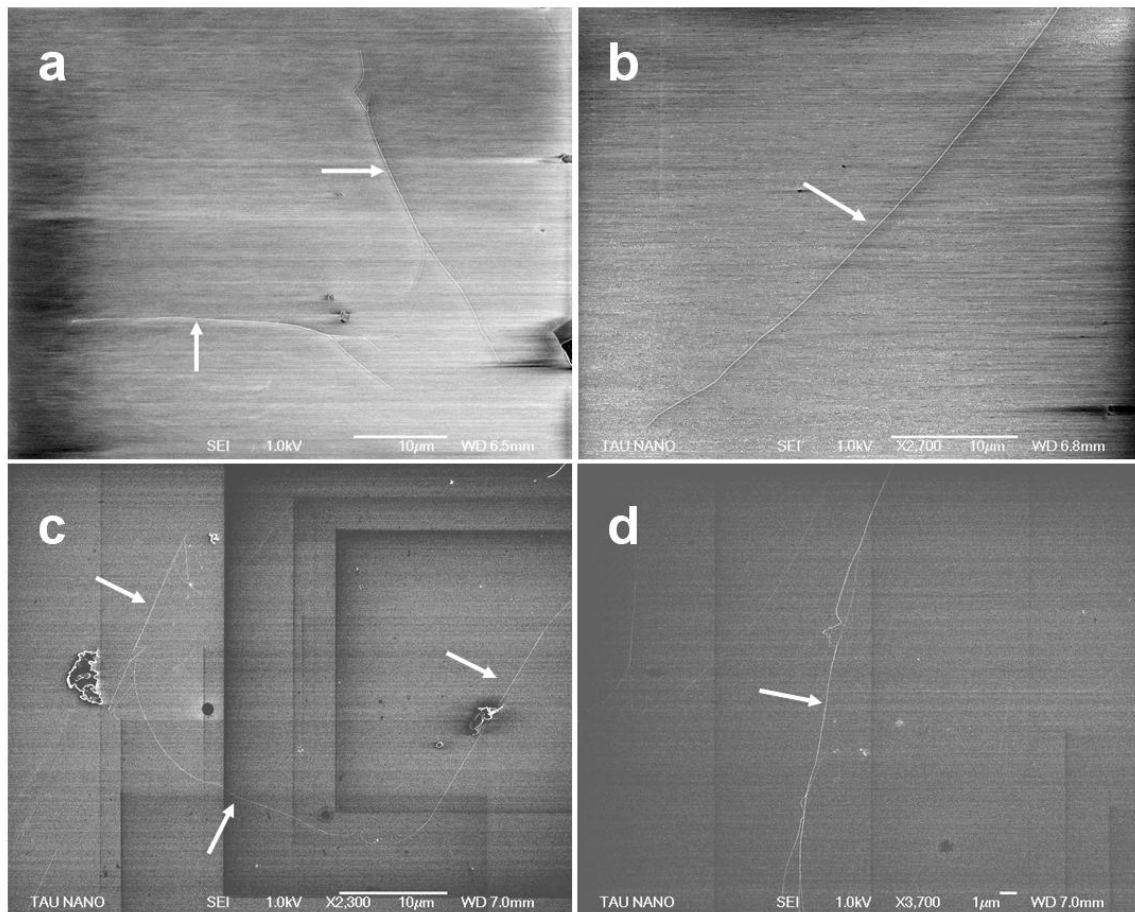


**Figure 45: Initial Stamping Results**

(a-b) Transferred nanotubes on a  $\text{SiO}_2$  substrate using hexane. (c-d) Nanotubes on a Si substrate using ethanol.

The initial transferring of nanotubes onto both Si and  $\text{SiO}_2$  substrates proved that the concept was tenable, yet the method was lacking in the sense that it was difficult to find the transferred tubes afterward, and more importantly, the low yield of transferred tubes. The main reasons for this low yield were both in the low yield of suspended nanotubes on the initial stamp (due to the initial growth process failures), as well as the combination of transfer media and temperatures. Better results were achieved when the temperatures were raised to 150-200 °C on the hot plate, and either ethanol or DI water were used. Figure 46a and b display the results of stamping on  $\text{SiO}_2$  using ethanol at 150 °C. What is important in these images is that the location of the pillar tops is evident from the markings they leave on the target substrate. Some of these stains are residual debris that was brought in by the liquid, such as chipped pieces of Si/ $\text{SiO}_2$ , and leftover bits of Fe catalyst (still others were caused by residual debris on the hot plate). Regardless, these results signified the first successful attempt at transferring large arrays of nanotubes onto a substrate, while retaining some of the initial array properties.



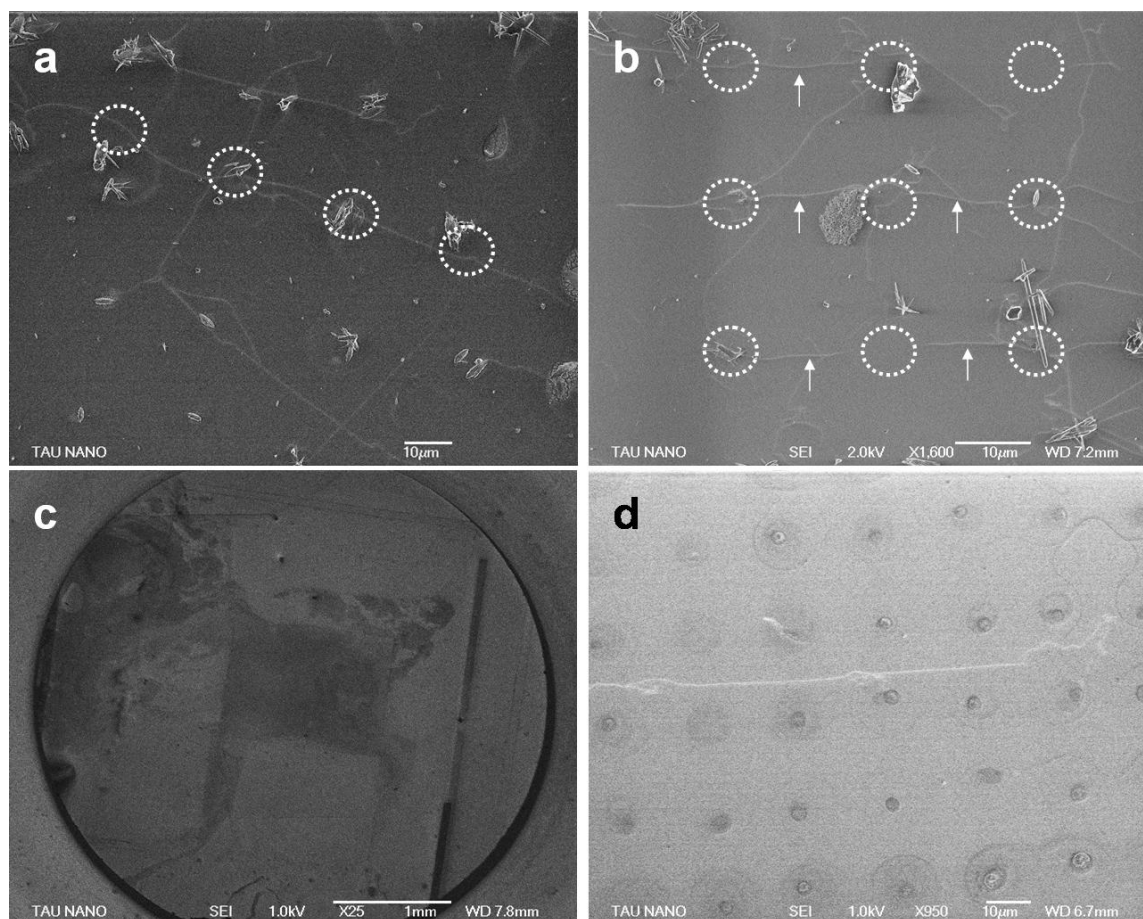


**Figure 46: Markings Made During Stamping Process**

(a-b) Nanotubes transferred onto SiO<sub>2</sub> using ethanol at 150° C. The white circles signify the locations of the pillars during the transfer process, as can be seen by some of the residues left behind. (c) Lowest magnification HRSEM image showing the location of the stamped die as a dark box in the center. (d) Image of a failed transfer, with the residues of the stamping array distinctly visible.

The best transfer results were obtained using DI water, as will be shown below, however, the residue left by the transfer medium is also an important feature in the transfer process. The medium, e.g. DI water, leaves a “stain” on the substrate that facilitates the locating of the stamped nanotubes. For example, in Figure 46c, the dark marking of the stamped die can be seen in the low magnification ( $\times 25$ ) HRSEM image. Without such markings, finding the miniscule array of stamped nanotubes (comprising a few hundred square microns) on a “large” substrate (of around two centimeters squared) is quite difficult. In addition, the markings left by the pillars themselves, as in Figure 46d, also ease the process of finding the nanotubes. The markings in Figure 46a and b are residual artifacts, and their existence is a testament to contaminants on the pillared stamp. The best transfer examples did not contain residual debris (although they almost always leave a large boxlike marking, as in Figure 46c).

The debris described here is part of a major complication in the transfer process, that of close-contact between the pillar tops and the target substrate. Even the residues formed by residual catalyst particles on the pillars signify that the nano-topography of the pillar tops are not completely flat. If the nanotubes are transferred by means of the

close-range interactions between the suspended segments and the target substrate, interactions whose range is no more than a few nanometers, then every nanotopographical detail is important. A 10 nm particle of Fe on the surface is like a large boulder, when compared to the 1-4 nm SWCNTs. Therefore, the optimal conditions are when the debris on the pillar tops is kept at a minimum. Furthermore, this issue is further aggravated by the fact that the pillars are placed in a well, due to the DRIE restrictions described, so that topographical anomalies on the surrounding regions may prevent the pillar tops from being in direct contact with the target surface.

The best transfer results were obtained, as stated before, using DI water on the hot plate, at temperatures ranging from 150-200° C (our most recent results points to a preference of higher temperatures, closer to 200° C). Figure 47 displays some of these stamping results. In all the images, the nanotubes transferred are very long and relatively straight. The spacing between rows of nanotubes in Figure 47a and b are defined exactly by the distance between pillars. The reason that there are few nanotubes in the vertical direction is testament to the effect of the gas-flow during the growth. The long strands of horizontal nanotubes signify that they are indeed single strands of nanotube, grown in the direction of the gas-flow, yet perpendicular segments are also seen. The diagonal segments seen in Figure 47b also are a result of non-nearest-neighboring growth between adjacent pillars in the initial network growth. Figure 47c is an example of how long and straight the stamped nanotube can be after transfer. The nanotubes here display extremely long (~20  $\mu\text{m}$ ) and straight segments, with perpendicular orientation, due to the square-like array of pillars in the stamp substrate. The fact that the long strands of nanotube are aligned in the gas-flow direction and are transferred in one single strand proves that the segments of nanotube adhering to the pillar top were also transferred, and did not “snap off” as was implied by the initial theoretical assumptions.

Figure 47e and f display even better results of stampings. Here, the exact positions of the stamping pillars during transfer are distinctly noticeable by the white spots left behind. These spots are actually SWCNTs transferred from the pillar tops themselves onto the target substrate (as shown in the inset of Figure 47f). This example of nanotubes being transferred from  $\text{SiO}_2$  to  $\text{SiO}_2$  does not comply with the theoretical assumptions of nanoimprinting described in the Literature Review, and is currently being investigated by us.

Since the effects of gas-flow could be seen in some of the transfer processes, our latest designs have tried growing nanotubes in only one direction, as can be seen in the inset of Figure 47d, with the teeth-like pattern described earlier. Here, the transferred results show that the distance between nanotubes is exactly that of the distance between neighboring “teeth”. Moreover, it is interesting to note that the nanotubes seen in the top and bottom of this image were transferred from the pillar tops (in essence, the areas below and above the teeth), to the new substrate. This means that the initial theory of only the suspended segments being transferred is also incorrect, as these nanotubes should have had no preference of being transferred from the  $\text{SiO}_2$  stamping substrate (pillar tops), to the  $\text{SiO}_2$  target substrate.

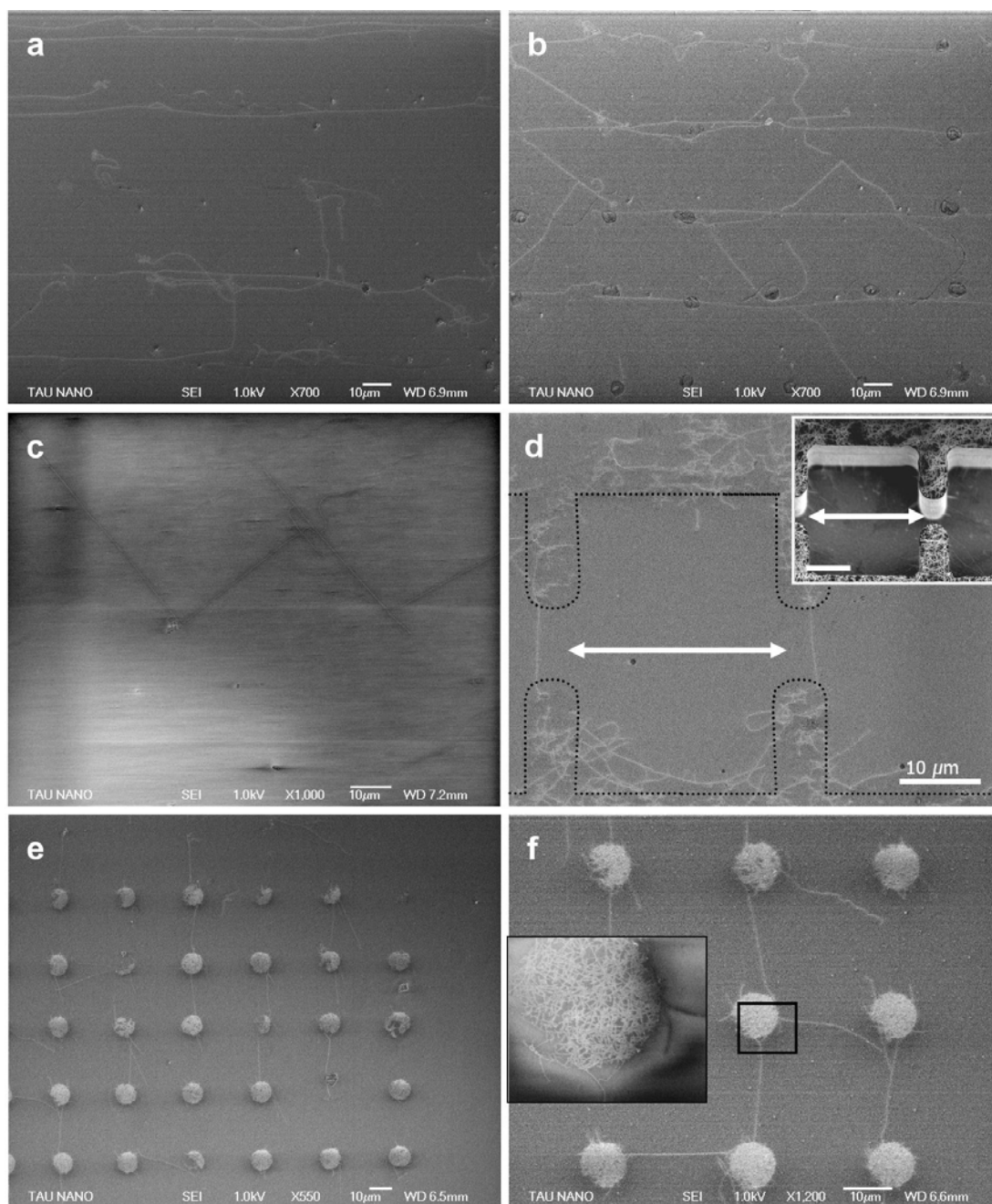


**Figure 47: Best Stamping Results**

(a-b) Large scale networks of transferred nanotubes, showing the spacing defined by the array of pillars. (c) A large “W” formed by perpendicular growth of the nanotubes between the pillars. (d) Transferred nanotubes between teeth-like pillars (shown in the inset). Arrows are 25  $\mu\text{m}$  long. (e-f) High yield of stamping including the nanotubes on the pillar tops. The white spots are the mesh of nanotubes that existed on the pillar tops prior to stamping, as demonstrated in the inset of (f).

## 6.7 TEM Stamping Verification

A question that is always raised in any stamping method of nanotubes is this: Are the transferred nanotubes individual tubes, or bundles? To answer this question, the HRSEM is inadequate, as it cannot differentiate between the two. An AFM would

also be inadequate, as it would be difficult to differentiate between two small diameter adjoining nanotubes (although, an STM should). The TEM is ideal for this, yet, how could one view the transferred network after being transferred onto a thick, opaque substrate?

The solution to this problem once again relied on the robust TEM nitride grids described before. An array of nanotubes was stamped *directly* onto a TEM grid, as rendered (not to scale) in Figure 48a and b. The stamping process was particularly delicate, in order not to fracture the thin nitride grid viewing area. In fact, the stamping was implemented upside down, with the grid stamped from *above*, and not as rendered. The grid chosen included the small 2  $\mu\text{m}$  holes, so that the nanotubes would be seen over these holes, and it was assumed that over the entire 500  $\mu\text{m}^2$  viewing area, with a multitude of such holes, a statistical chance of finding such a transferred nanotube would occur. Figure 48c, d and e are TEM images of such a nanotube suspended (after transfer) over a hole (there were many such instances). The transferred nanotube was measured to be  $\sim 4$  nm in diameter. Here again, the method of finding individual nanotubes on such a large grid, by viewing them at extreme defocused conditions, was found to be crucial.

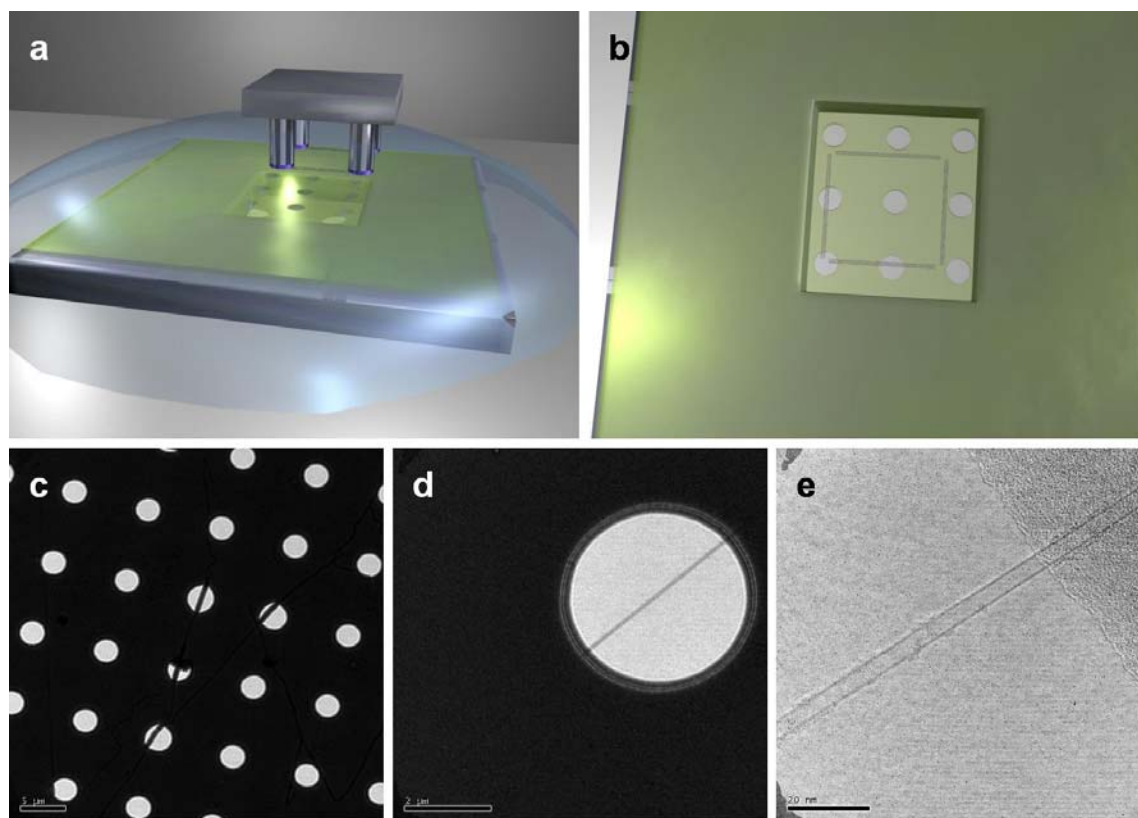


**Figure 48: TEM Verification of Stamped Nanotubes**

(a-b) Renderings of the stamping procedure, showing a pillared substrate attached to the TEM grid with a small amount of DI water. (b) The transferred nanotubes would include some that would extend across at least one of the holes in the grid. Renderings are *not* to scale. (c-e) TEM images of the transferred nanotubes. Each image is a magnification of the previous one, with the final one, (e), displaying the 4 nm tube at the edge of the hole in the nitride grid.

The results of this transfer procedure provide conclusive evidence that the nanotubes transferred were isolated SWCNTs (in most cases), and the images in Figure 48d and e display the straightness and lack of defects in the transferred nanotube.

## 6.8 CNTFET Fabrication

Ultimately, the transferred nanotubes' purpose are be integrated in an architecture that would utilize them as nanowires or CNTFETs. Two methods were used for such integration: stamping them onto electrodes, or adding the electrodes afterwards.

The first method used at implementing such a device used the concept of stamping the nanotubes onto a ready-made substrate containing electrodes. These electrodes consisted of large scale Cr-Au blocks (~70 nm high) with separated regions of differing spacing. The pillar die was stamped directly onto these electrodes, without any alignment, in the hopes that a few would bridge the gap between adjacent electrode pairs. Figure 49a shows such an electrode, and Figure 49b shows one of the sets of electrodes with a nanotube in between.

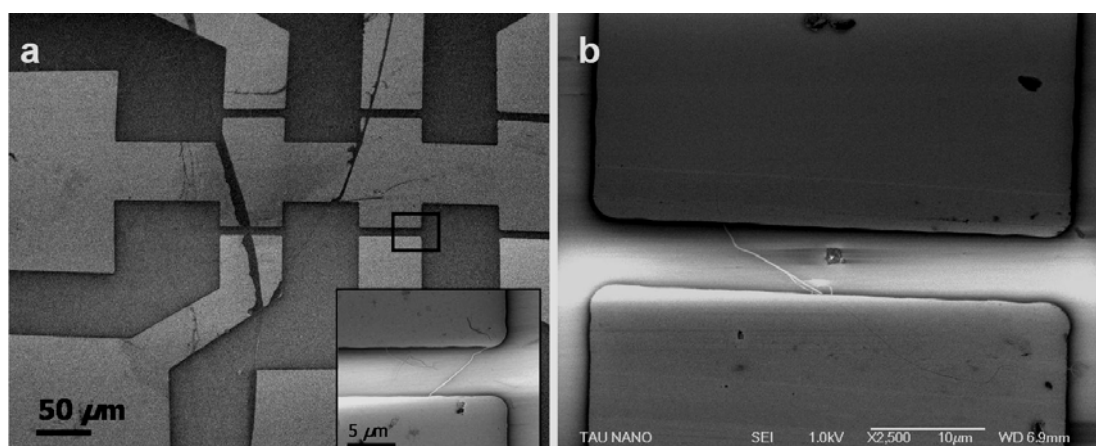


**Figure 49: Stamping onto Existing Electrodes**

- (a) HRSEM image of the electrode pattern, with six sets of gaps (black lines are stains created during the stamping procedure). Inset shows a nanotube between two of the electrodes. (b) Another image of a SWCNT between two electrodes.

The other method of contacting the nanotubes is to stamp them onto another ( $\text{SiO}_2$ ) surface, and then attach the electrodes. Since the nanotubes are undetectable using optical means, no alignment process using standard photo-lithography could be used. Instead, a target substrate was first marked with Cr-Au alignment marks, consisting of small crosses at a distance of 1 cm, and fabricated using regular photo-lithography. This substrate was then stamped with an array of nanotubes, far from the crosses (which would otherwise impede the direct contact between the pillar tops and the substrate surface). The sample was then taken to the HRSEM in the RAITH (e-beam lithography, with the assistance of Dr. A. Tsukernik), and a coordinate system was created using the alignment marks. Simple contacts were then drawn using the RAITH software on three such isolated nanotubes. The sample was then coated with PMMA, and written upon using the e-beam. Finally, electrodes (Cr 8 nm, Au 20 nm) were evaporated on them.

The results of this lithography steps are presented in Figure 50a and b. These images are unique in that the nanotubes are completely straight underneath. The small features of the electrodes signify how many parallel sets of electrodes could theoretically be placed on the same long segment of nanotube. Each electrode is 200 nm thick (70 nm high), and the distance between pairs of electrodes ranged from 0.5 to 1.5  $\mu\text{m}$  in Figure 50a, and 1  $\mu\text{m}$  in Figure 50b.

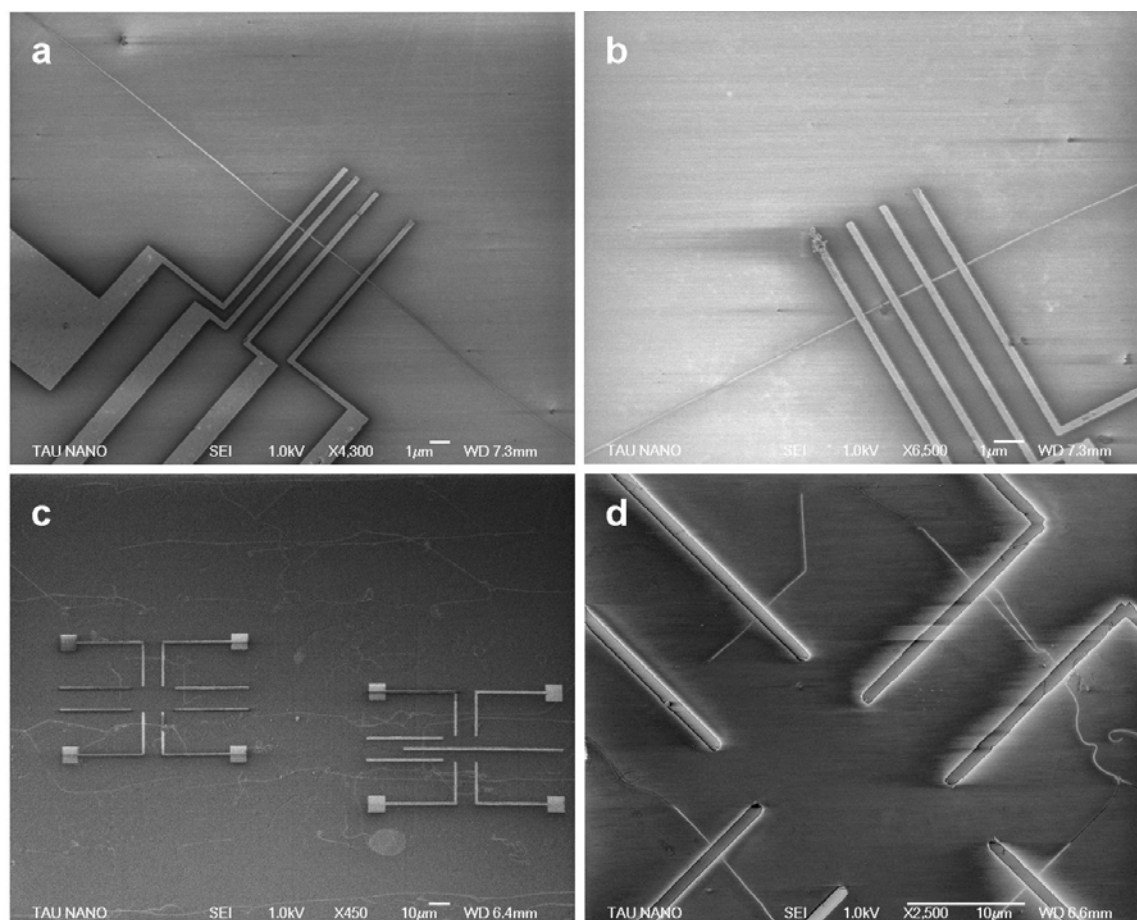


**Figure 50 Electrodes Patterned on Stamped Nanotubes**

(a-b) E-beam defined electrodes on single long, straight strands of nanotubes. (c) Complex e-beam patterned designs on large nanotube arrays. (d) Design utilizing the orthogonal array of SWCNTs.

In addition to contacting electrodes, a more interesting architecture was designed to utilize the orthogonal placement of the CNTs displayed in Figure 47. The electrodes were created in a similar fashion, using regular photo-lithography to create the alignment marks, and then e-beam lithography to create the electrodes. The results depicted in Figure 50d are one of the best examples of the alignment of nanotubes on a substrate, with the distance and orientation of the nanotubes under well-controlled parameters. However, to be critical, one of the problems with the results depicted in these bottom two images is that the nanotubes are not as straight and well ordered as they were before the placement of the electrodes. In fact, what had happened was that the double lithography (photo- and e-beam), which include the cleaning (in solvents) and spin-coating of a resist, accidentally moved the nanotubes a bit, destroying some of their alignment straightness. The nanotubes in Figure 50d were originally (before



electrode patterning) straighter, and the nanotube between the upper left two electrodes originally stretched between the two electrodes, completing the circuit. The spin-coating and surface preparation processes are actually quite aggressive on the nanoscale, where the size of the nanotubes is almost comparable to the size of the molecules comprising the resists and solvents. Therefore, when preparing such devices in the future, special care must be taken in order to protect these fragile systems.

## 6.9 Electrical Measurements

The imprinting of the nanotubes on different substrates was the primary goal of this thesis and was demonstrated in the images above. To demonstrate that these are also viable devices, they were also tested electronically. Using the setup described in the previous chapter, the electrodes shown in Figure 49 and Figure 50 (a and b) were contacted at either end, providing a source and drain voltage, and the underlying Si was also contacted, providing a gate voltage (gate thickness was thus  $\sim 500$  nm, as defined by the thickness of the thermal oxide grown on the wafers). Measurements were made on both types of CNTFETs (those created by placing the nanotubes onto existing electrodes, and also those made by adding the electrodes on top of the tubes). In the former case, the Au is in contact with the SWCNT, whereas in the latter case, it is the Cr.

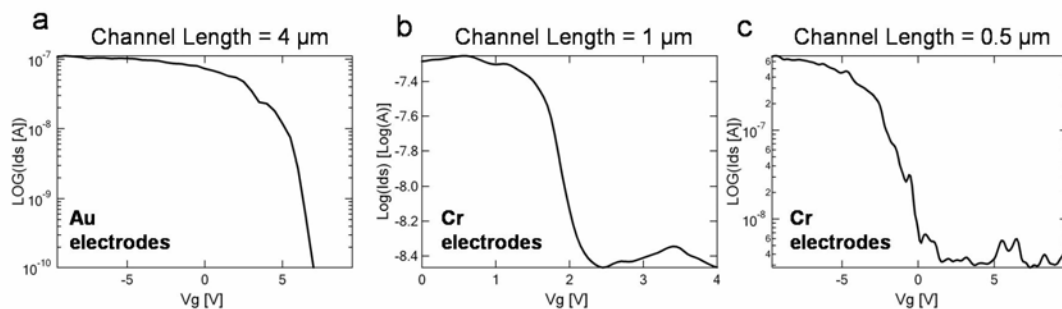


**Figure 51: I-V Characteristics of the CNTFETs**

(a) Nanotube placed over existing Au electrodes. (b-c) Nanotube transistors from Figure 50a and b. All measurements used a drain-source voltage of 0.1 V.

Figure 51 displays typical I-V curves of p-type SWCNT transistors, with varying channel lengths. The graphs are semi-logarithmic, to stress the on-off gain ratio. The CNTFET in Figure 51a of a nanotube placed on existing electrodes, with a gap of  $\sim 4$   $\mu\text{m}$ , shows an on-off gain ratio of four orders-of-magnitude, achieving a saturation current of 0.1  $\mu\text{A}$ , and an off current of a few pA. Figure 51b and c display the I-V curves for the p-type SWCNT transistors displayed in Figure 50a and b. Here, the on-off gain ratio was two orders-of-magnitude for the short transistor (0.5  $\mu\text{m}$  channel), and only one order-of-magnitude for the longer one (1  $\mu\text{m}$  channel). The discrepancy may be due to the difference in work functions between the Cr and the Au (4.5 and 5.1 eV, respectively), which in each case, had a different metal contacting the nanotube. The different surface properties of the two samples may also contribute to the observable shift in the threshold voltage between these two devices. These transistors were measured without any annealing processes, which are known to improve the characteristics. Regardless, these CNTFETs demonstrated characteristics



comparable with existing individual CNTFETs derived using the other methods described in the Literature Review. More measurements of these CNTFETs do not appear here since these electrodes were destroyed after continuous use by the probe station (scratching the electrodes). However, these measurements will soon be repeated, when new CNTFETs will be created using this method.

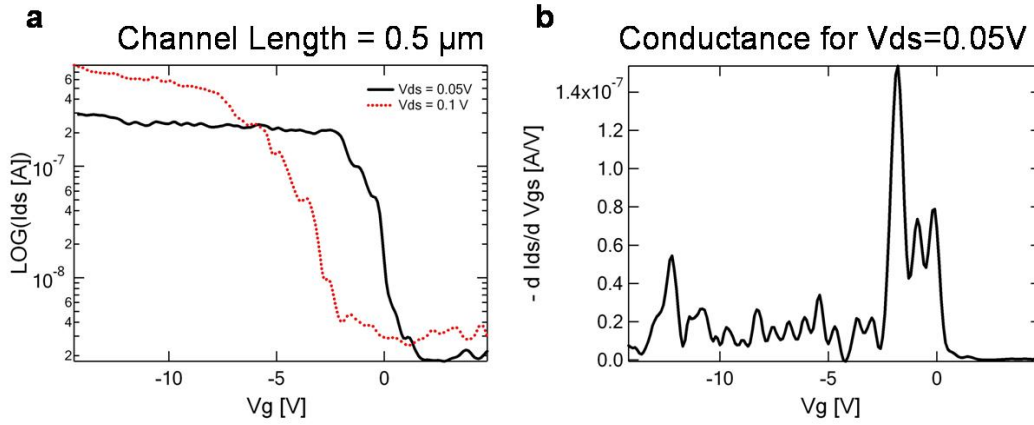


**Figure 52: Conductance Measurements of a CNTFET**

(a) The same CNTFET characteristic appearing in Figure 52c, at different drain-source voltages. (b) The conductance of the CNTFET at  $V_{ds}=0.05\text{V}$ . The peak conductance is used to find the mobility of the holes.

To measure the mobility of one of these transistors, the characteristic curve was differentiated with respect to the gate voltage (Figure 52). Taking the peak mobility from each curve, and using the formula given in Appendix 2, the mobility of each was found. In both the samples containing electrodes placed before imprinting the nanotubes, and those with the electrodes placed after imprinting, the gate oxide thickness was defined by the initial 500 nm thick thermal oxide layer. Considering the case for a  $\sim 2.5\text{ nm}$  SWCNT (an average diameter for CVD grown SWCNTs), the total capacitance can be estimated to about  $0.3\text{ pF/cm}$  [with  $C_{\text{gate}} \ll C_{\text{quantum}}$ , and  $C_{\text{gate}} \sim 2\pi\epsilon/\ln(2h/d)$ , as in Appendix 2]. Calculating the conductance ( $-dI_{ds}/dV_{gs}$ ) near the transition region for the transistors, shown in Figure s4b, we can deduce an approximate mobility of  $\sim 500\text{ cm}^2/\text{Vs}$  for the holes in this "p-type" transistor [ $\mu \sim L^2/C \cdot V_{ds}(dI/dV)$ ]. This number, while higher than that of silicon, is lower than many traditional CNT-based transistors, however, it should be noted that no annealing was done to improve these characteristics, as is customary.

## 7 Summary, Conclusions and Future Developments

### 7.1 Summary and Conclusions

The physicist R. Feynman initially envisioned the construction of nano-sized materials by creating small robotic hands that would in turn be used to fabricate even smaller hands [1]. The chemist R. E. Smalley criticized this concept as a pipe dream (or, tube dream?) since he argued that stiction would occur at the molecular level when dealing with such small nanometric objects, rendering these approaches useless [2]. The imprinting method described here paradoxically utilizes both concepts: finger-like pillars in the micrometer scale are used to manipulate individual SWCNTs, while the adhesion of the nanotubes to the target substrate is also crucial to this work.

The research described in this thesis had dynamic goals, all of which were achieved. The original goal of emulating the results of creating suspended networks of nanotubes was first achieved, followed by our published work on explaining the formation process of these networks [90]. To achieve this task, a novel TEM method was developed and reported [92]. The indeterminate dynamic goal of utilizing these structures to create useable arrays of nanotubes was also implemented by using the concept of imprinting large pre-arranged networks of nanotubes onto different substrates.

When integrated with the RS mapping technique, the stamping technique can be upgraded into a more complete method of creating nanocircuitry, as described in our paper [91]. By integrating both the stamping method presented, as well as the RS mapping, one can quickly and inexpensively create large arrays of CNT devices, while simultaneously acquiring the chiral indices of each of the stamped nanotubes (see Figure 53). The scheme would start with the growth of a suspended network of nanotubes, followed by its complete RS mapping to create a database of (n,m) values per tube; then, the nanotubes would be stamped onto another substrate, with the ensuing network comprised of well-identified, individually isolated SWCNTs. The advantages of this scheme are as follows:

- The use of long, defect-free SWCNTs grown in the suspended state
- Precise structural information related by the Raman mapping
- Simple, one-shot procedure enabling the creation of an entire prearranged network of individual SWCNTs
- Use of long and straight segments of nanotubes, with the same electronic properties
- The ability to imprint on a variety of substrates that would not otherwise survive the CVD growth process

This final point is crucial: it means that the process described is fully IC compatible, and can even be implemented on plastic substrates. Further modifications of the scheme could include chirality-controlled CVD growth of CNTs by selectively choosing the catalysts [103] deposited on the pillar tops, as well as better control of both the yield and directionality of the SWCNTs between the pillars, and removal of

stray nanotubes [86]. In terms of CNTFET properties, one can tailor the sensitivity of each parallel array of CNTFETs (on each nanotube segment,) to the specifications of each individual nanotube.

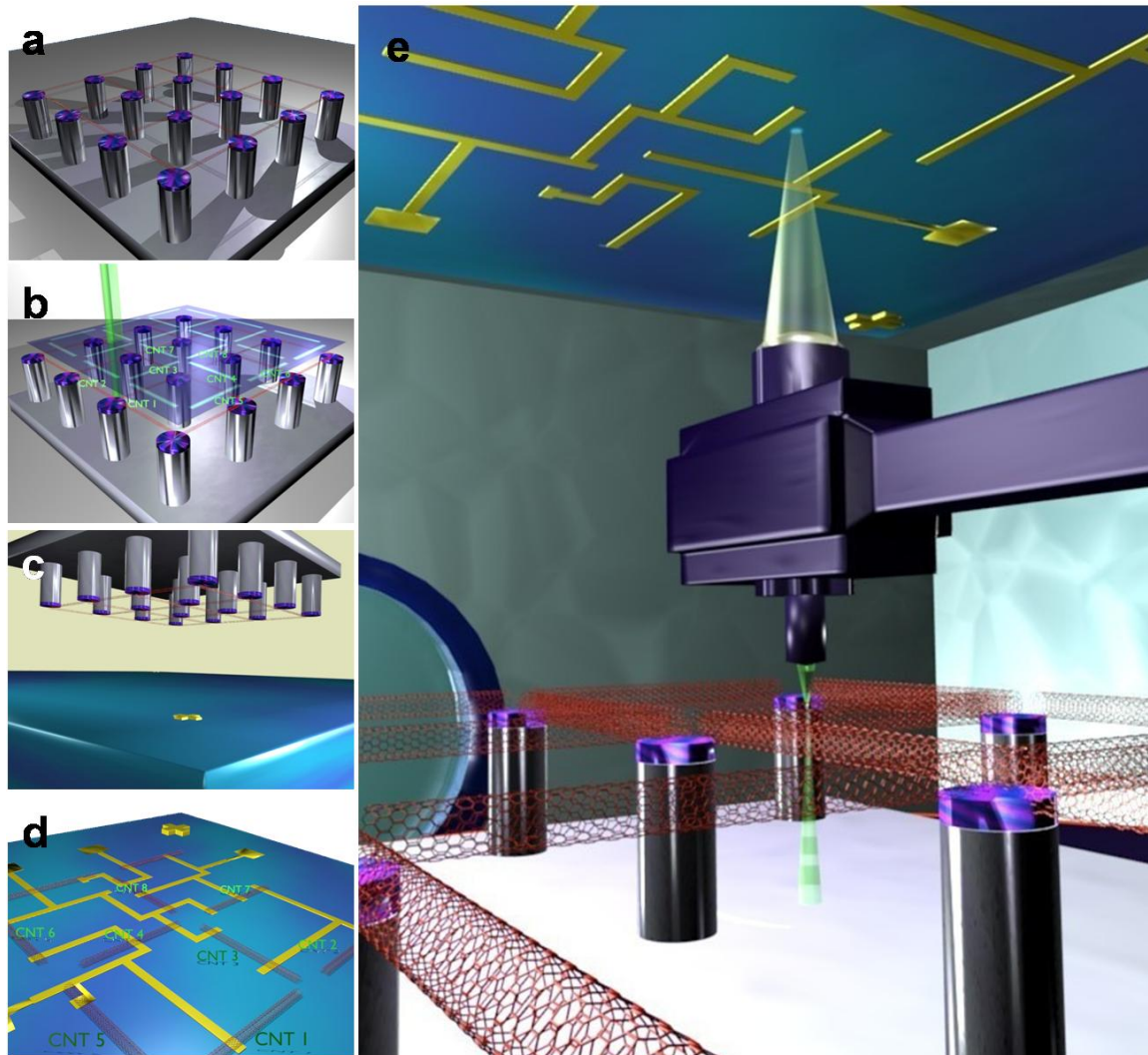


**Figure 53: Complete Method for Stamping Nanotube Networks**

(a) Nanotube growth between pillars. (b) Raman mapping of each suspended nanotube. (c) Stamping of the nanotubes onto a substrate with alignment marks. (d) Organized array of identified nanotubes in a pre-arranged circuit. (e) A theoretical setup of a system aligning the network of pillars to a pre-arranged circuit, while simultaneously Raman scanning the nanotubes.

Figure 53e displays a rendering of such a systematic device, with the simultaneous RS mapping and alignment to another substrate. This would combine the RS system with existing nano-imprinting technology. A scheme such as this would be a comprehensive and scalable technique for creating large scale devices. The major limitations in this scheme lie in the yield of transferred tubes, and in the initial growth of the network of CNTs between the initial pillars, where little control over the number of suspended nanotubes between adjacent pillars. Some of these problems have been addressed in this thesis. For example, using our liquid-based catalyst deposition, we have achieved nearly 100% yields of CNTs between neighboring pillars - much higher than previously reported methods. However, this also leads to

the growth of more than one CNT between each pillar. The solution to this problem has been found by us to be a matter of pillar geometry: small pillar tops ( $\leq 1\ \mu\text{m}$ ) will yield fewer stray CNTs between pillars, and larger spacing ( $>20\ \mu\text{m}$ ) accomplishes a further filtration of surplus nanotubes suspended between adjacent pillars, with shorter tubes falling to the ground. It would also prevent the diagonal growth of nanotubes between non-adjacent pillars. Further investigation of improving the initial network growth is currently under investigation.

One of the more practical aspects of the nanotube imprinting method presented here is that, once the process is well-defined, the transition from a single wafer of silicon, to a stamped array of nanotubes can theoretically be implemented in the course of about two days, by a single individual. Therefore, the final results presented never accurately portray the amount of effort entailed. Nevertheless, the quality of results should be measured by their *objective* worth. Consequently, when evaluating the images of the transferred nanotubes, one must compare them to the current state-of-the-art techniques existing today, and as described in the Literature Review. While the quality of some of the images both here and there is comparable, it is the inherent advantages of this system in comparison to the others that makes it useful. Unlike the two-stage rapid-annealing method [80], this stamping process is done in one step, and the final substrate need not be exposed to the high temperature CVD heating process. In addition, unlike the stamping method of Refs. [81,82], this method allows the simultaneous stamping of numerous nanotubes, in a prearranged fashion, and not just one by one. Furthermore, the Rayleigh spectroscopy method described there is far less robust than the RS mapping described here.

The competition in the field of CNT patterning is such that each passing day may introduce a similar or better method. In fact, the main competition to the work presented here was by a collaborative group at Columbia University (Refs. [37,81,82]), who demonstrated the individual stamping of SWCNTs, (as in Figure 23c,) over the last two years. Moreover, their method of identifying specific nanotubes using Rayleigh spectroscopy mirrors our use of Raman spectroscopy, as is their overall claims of creating a complete methodology of patterning individual SWCNTs. Needless to say, I believe that this work holds its own in comparison, with many clear advantages.

## 7.2 Future Developments

The method described in this thesis has recently been patented by us. As such, we are very interested in taking the technology a few steps further. Designs for devices using this method have already been drawn up, and their implementation is well underway. Since the method allows one to create arrays of nanotubes on different surfaces, some of the devices planned are designed to utilize this to the fullest. Four such devices will be described below.

The first device planned will simply rely on the placement of parallel nanotubes on a surface, and contacting them with many perpendicular electrodes. By using the ambipolar properties of the SWCNT, both electrons and holes can be injected into the tube (as described in Figure 17), resulting in a set of IR sources, as rendered in Figure 54a, this can also act as an IR detector. This device utilizes the straightness property

of the imprinted tubes, whereby each adjacent set of electrodes on the strand of nanotube is contacting an SC-SWCNT with *exactly* the same band-gap, thereby emitting identical IR wavelengths. Using this same geometry, one can also create a flow sensor, using the method described in Ref. [57], with each set of parallel SWCNTs simultaneously detecting the flow rate.

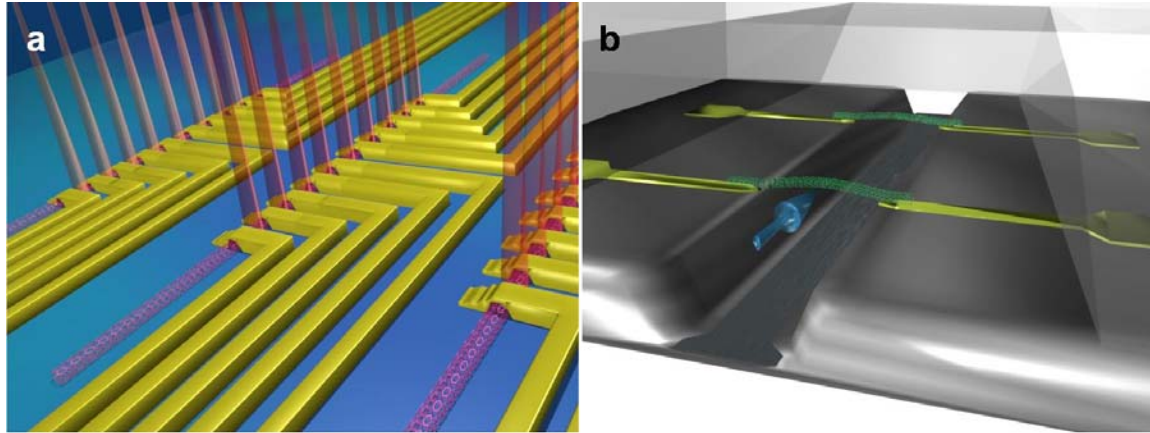


**Figure 54: Possible Future Devices**

(a) An IR source fabricated on parallel strands of SWCNTs. Between each set of electrodes is an identical band-gap semi-conductor, emitting the same IR wavelength.

(b) Nanotubes positioned over small trenches in a PDMS defined micro-fluidic channel. The liquid flow causes the nanotube to bend, which will be detected by an external circuit.

Another device envisioned would place a SWCNT over a small trench, with electrodes at either end, as rendered in Figure 54b. The substrate would then be encased in a PDMS defined micro-fluidic channel, and a liquid would be injected through the channel. Since the strain on the nanotube induced by the flow of the liquid should result in its bending, one would expect the resistance of the nanotube to change. Therefore, this could also act as a nanoscaled flow meter for micro-fluidics.

A similar device would also place nanotubes over a trench, but, due to the fact that the initial network of nanotubes is comprised of taut tubes, the bridging nanotube stamped over a set of separated electrodes will also remain straight and taut. This can be used as an electromechanical oscillator [104], with the advantage of the devices devised using this method consisting of nanotubes without any slack.

A final device would rely on a two-step process to obtain perpendicular sets of straight nanotubes, so that the second imprinting step will place a set of SWCNTs perpendicular to the first. These nanotubes would then be attached to electrodes, with one of the perpendicular SWCNTs acting as a gate to the other, as rendered in Figure 55. This local gating is not only useful in terms of CNTFET design, but also includes the use of the one-dimensional SWCNT channel and the tiny, single nanometer gate, to act as a zero-dimensional quantum dot. This type of design is only possible with the precise placement technique devised in this thesis.

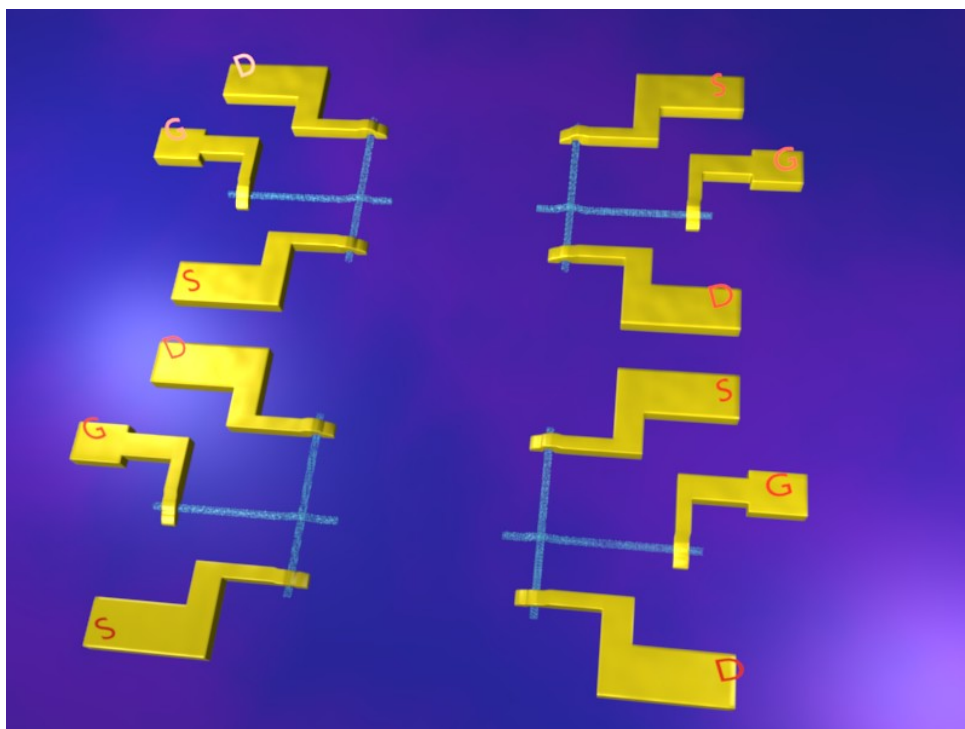


**Figure 55: Local Gating of Perpendicular Sets of Aligned Nanotubes**

A double stamping procedure will place a set of perpendicular SWCNTs on top of an existing set, allowing the local gating of the CNTFETs.

As stated, these devices are currently being designed, with some of the devices expected to be fabricated within the next year.



## 8 References

1. "There's plenty of room at the bottom", Richard P. Feynman, December 1959, At Caltech's official page:  
<http://www.its.caltech.edu/~feynman/plenty.html>
2. Chemical and Engineering News: This was part of a series of articles consisting of open letters between Prof. Smalley, and one of the founding fathers of nanotechnology, K. Eric Drexler at the site:  
<http://pubs.acs.org/cen/coverstory/8148/8148counterpoint.html>
3. Iijima S, "Helical microtubules of graphite carbon" *Nature* **354**, 56–8 (1991)
4. Iijima S, Ichihashi T "Single-shell carbon nanotubes of 1-nm diameter" *Nature* **363** 603–5 (1993)
5. Oberlin A, Endo M, Koyama T "Filamentous growth of carbon through benzene decomposition" *J. Cryst. Growth* **32**, 335–49 (1976)
6. *Carbon Nanotube Synthesis, Structure and Applications*; Dresselhaus, M S, Dresselhaus, G, Avouris, Ph, Eds.; Springer: Berlin, 2001
7. Dai, H "Carbon nanotubes: opportunities and challenges" *Surf. Sci.* **500**, 218–241 (2002)
8. McEuen P L, Fuhrer M S, Park H "Single-Walled Carbon Nanotube Electronics" *IEEE Trans. Nanotechnol.* **1**, 78–88 (2002)
9. Popov, V N "Carbon nanotubes: properties and application" *Mater. Sci. Eng. R* **43**, 61–102 (2004)
10. Belin T, Epron F "Characterization methods of carbon nanotubes: a review" *Mater. Sci. Eng. B* **119**, 105–118 (2005)
11. Li X, *et al.* " Bottom-Up Growth of Carbon Nanotube Multilayers: Unprecedented Growth" *Nano Lett.* **5**, 1997–2000 (2005)
12. Tersoff J, Ruoff R S "Structural Properties of a Carbon-Nanotube Crystal" *Phys. Rev. Lett.* **73**, 676–679 (1994)
13. Durkop T, Kim B M, Fuhrer M S "Properties and applications of high-mobility semiconducting nanotubes" *J. Phys.: Condens. Matter* **16**, 553–580 (2004)
14. Bachilo S M, Strano M S, Kittrell C, Hauge R H, Smalley R E, Weisman R B "Structure-Assigned Optical Spectra of Single-Walled Carbon Nanotubes" *Science* **298**, 2361–2366 (2002)
15. Gao B, Chen Y F, Fuhrer M S, Glatli D C, Bachtold A "Four-Point Resistance of Individual Single-Wall Carbon Nanotubes" *Phys. Rev. Lett.* **95**, 196802–196804 (2005).
16. Yu M F, Files B S, Arepalli S, Ruoff R S "Tensile Loading of Ropes of Single Wall Carbon Nanotubes and their Mechanical Properties" *Phys. Rev. Lett.* **84**, 5552–5555 (2000)
17. Service R F "Breakthrough of the Year" *Science* **294**, 2442 (2001)
18. Ajayan P M, Iijima S "Capillarity-induced filling of carbon nanotubes" *Nature* **361**, 333 (1993)
19. Monthieux M "Filling single-wall carbon nanotubes" *Carbon* **40**, 1809–1823 (2002)
20. Svensson K, Olin H, Olsson E "Nanopipettes for Metal Transport" *Phys. Rev. Lett.* **93**, 145901–145905 (2004)



21. Smith B W, Monthieux M, Luzzi D E “Encapsulated C<sub>60</sub> in carbon nanotubes” *Nature* **396**, 323-324 (1998)
22. Meyer R R, Sloan J, Dunin-Borkowski R E, Kirkland A I, Novotny M C, Bailey S R, Hutchison J L, Green M L H “Discrete Atom Imaging of One-Dimensional Crystals Formed Within Single-Walled Carbon Nanotubes” *Science* **289**, 1324-1326 (2000)
23. Kiang C H, Goddard W A III, Beyers R, Bethune D S “Structural Modification of Single-Layer Carbon Nanotubes with an Electron Beam” *J. Phys. Chem.* **100**, 3749-3752 (1996)
24. Smith B W, Luzzi D E “Electron irradiation effects in single wall carbon nanotubes” *J. Appl. Phys.* **90**, 3509-2515 (2001)
25. Ruoff R S, Tersoff J, Lorents D C, Subramoney S, Chan B. “Radial deformation of carbon nanotubes by van der Waals forces” *Nature* **364**, 514–516 (1993)
26. Hertel T, Walker R E, Avouris Ph “Deformation of carbon nanotubes by surface van der Waals forces” *Phys. Rev. B* **58**, 13870–13873 (1998)
27. Yu M F, Kowalewski T and Ruoff R S “Structural Analysis of Collapsed, and Twisted and Collapsed, Multiwalled Carbon Nanotubes by Atomic Force Microscopy” *Phys. Rev. Lett.* **86**, 87-90 (2001)
28. Falvo M R, Clary G J, Taylor R M II, Chi V, Brooks F P Jr, Washburn S, Superfine R “Bending and buckling of carbon nanotubes under large strain” *Nature* **389**, 582-584 (1997)
29. Hertel T, Martel R and Avouris Ph “Manipulation of Individual Carbon Nanotubes and Their Interaction with Surfaces” *J. Phys. Chem. B* **102**, 910 (1998)
30. Brintlinger T, Chen Y F, Durkop T, Cobas E, Fuhrer M S, Barry J D, Melngailis J “Rapid imaging of nanotubes on insulating substrates” *Appl. Phys. Lett.* **81**, 2454-2456 (2002)
31. Rao A M, Richter E, Bandow S, Chase B, Eklund P C, Williams K A, Fang S, Subbaswamy K R, Menon M, Thess A, Smalley R E, Dresselhaus G, Dresselhaus M S “Diameter-Selective Raman Scattering from Vibrational Modes in Carbon Nanotubes” *Science* **275**, 187-191 (1997)
32. Dresselhaus M S, Dresselhaus G, Jorio A, Souza Filho A G, Saito R “Raman spectroscopy on isolated single wall carbon nanotubes” *Carbon* **40**, 2043-1061 (2002)
33. Jorio A, Pimenta M A, Souza Filho A G, Saito R, Dresselhaus G, Dresselhaus M S “Characterizing carbon nanotube samples with resonance Raman scattering” *New J. Phys.* **5**, 1–17 (2003)
34. Kaminska K, Lefebvre J, Austing D G, Finnie P “Real-time global Raman imaging and optical manipulation of suspended carbon nanotubes” *Phys. Rev. B* **73**, 235410-235416 (2006)
35. Son H, Hori Y, Chou S G, Nezich D, Samsonidze Ge G, Dresselhaus G, Dresselhaus M S, Barros E B “Environment effects on the Raman spectra of individual single-wall carbon nanotubes: Suspended and grown on polycrystalline silicon” *Appl. Phys. Lett.* **85**, 4744-4746 (2004)
36. Lefebvre J, Austing D G, Bond J, Finnie P “Photoluminescence Imaging of Suspended Single-Walled Carbon Nanotubes” *Nano Lett.* **6**, 1603-1608 (2006)
37. Sfeir M Y, Wang F, Huang L, Chuang C C, Hone J, O’Brien S P, Heinz T F, Brus L E “Probing Electronic Transitions in Individual Carbon Nanotubes by Rayleigh Scattering” *Science* **306**, 1540-1543 (2004)

38. Tans S J, Devoret M H, Dai H, Thess A, Smalley R E, Geerligs L J, Dekker C "Individual single-wall carbon nanotubes as quantum wires" *Nature* **386**, 474-477 (1997)
39. Tans S J, Verschueren A R M, Dekker C "Room-temperature transistor based on a single carbon nanotube" *Nature* **393**, 49-53 (1998)
40. Martel R, Schmidt T, Shea H R, Hertel T, Avouris Ph "Single- and multi-wall carbon nanotube field-effect transistors" *Appl. Phys. Lett.* **73**, 2447-2449 (1998)
41. Leonard F, Tersoff J "Role of Fermi-Level Pinning in Nanotube Schottky Diodes" *Phys. Rev. Lett.* **84**, 4693 - 4696 (2000)
42. Derycke V, Martel R, Appenzeller J, Avouris Ph "Carbon Nanotube Inter- and Intramolecular Logic Gates" *Nano Lett.* **1**, 453-456 (2001)
43. Chen Z, Appenzeller J, Lin Y M, Sippel-Oakley J, Rinzler A G, Tang J, Wind S J, Solomon P M, Avouris Ph "An Integrated Logic Circuit Assembled on a Single Carbon Nanotube" *Science* **311**, 1735 (2006)
44. Zhou X, Park J Y, Huang S, Liu J, McEuen P L "Band Structure, Phonon Scattering, and the Performance Limit of Single-Walled Carbon Nanotube Transistors" *Phys. Rev. Lett.* **95**, 146805-146809 (2005)
45. Leonard F, Stewart D A "Properties of short channel ballistic carbon nanotube transistors with ohmic contacts" *Nanotechnol.* **17**, 4699-4705 (2006)
46. Avouris Ph, Appenzeller J, Martel R, Wind S J "Carbon Nanotube Electronics" *Proc. IEEE* **91**, 1772-1784 (2003)
47. Gao B, Chen Y F, Fuhrer M S, Glatli D C, Bachtold A "Four-Point Resistance of Individual Single-Wall Carbon Nanotubes" *Phys. Rev. Lett.* **95**, 196802-196805 (2005)
48. Javey A, Guo J, Wang Q, Lundstrom M, Dai H "Ballistic carbon nanotube field-effect transistors" *Nature* **424**, 654-657 (2003)
49. Rosenblatt S, Lin H, Sazonova V, Tiwari S, McEuen P L "Mixing at 50 GHz using a single-walled carbon nanotube transistor" *Appl. Phys. Lett.* **87**, 153111-153113 (2005)
50. Tseng Y C, Xuan P, Javey A, Malloy R, Wang Q, Bokor J, Dai H "Monolithic Integration of Carbon Nanotube Devices with Silicon MOS Technology" *Nano Lett.* **4**, 123-127 (2004)
51. Mahar B, Laslau C, Yip R, Sun Y "Development of Carbon Nanotube-Based Sensors—A Review" *IEEE Sens. J.* **7**, 266-284 (2006)
52. Kong J, Franklin N R, Zhou C, Chapline M G, Peng S, Cho K, Dai H "Nanotube Molecular Wires as Chemical Sensors" *Science* **287**, 622-625 (2000)
53. Besteman K, Lee J O, Wiertz F G M, Heering H A, Dekker C "Enzyme-Coated Carbon Nanotubes as Single-Molecule Biosensors" *Nano Lett.* **3**, 727-730 (2003)
54. Ciraci S, Dag S, Yildirim T, Gulseren O, Senger R T "Functionalized carbon nanotubes and device applications" *J. Phys.: Condens. Matter* **16**, 901-960 (2004)
55. Daniel S, Rao T P, Rao K S, Rani S U, Naidu G R K, Lee H Y, Kawai T "A review of DNA functionalized/grafted carbon nanotubes and their characterization" *Sens. Act. B* **122**, 672-682 (2007)
56. Ghosh S, Sood A K, Kumar N "Carbon Nanotube Flow Sensors" *Science* **299**, 1042-1044 (2002)

57. Bourlon B, Wong J, Miko C, Forro L, Bockrath M "A nanoscale probe for fluidic and ionic transport" *Nature Nanotechnol.* **2**, 104-107 (2007)
58. Franklin N R, Wang Q, Tombler T W, Javey A, Shim M, Dai H "Integration of suspended carbon nanotube arrays into electronic devices and electromechanical systems" *Appl. Phys. Lett.* **81**, 913-915 (2002)
59. Hierold C, Jungen A, Stampfer C, Helbling T "Nano electromechanical sensors based on carbon nanotubes" *Sens. Act. A* **136**, 51-61 (2007)
60. Misewich A, Martel R, Avouris Ph, Tsang J C, Heinze S, Tersoff J "Electrically Induced Optical Emission from a Carbon Nanotube FET" *Science* **300**, 783-786 (2003)
61. Martel R, Derycke V, Lavoie C, Appenzeller J, Chan K K, Tersoff J, Avouris Ph "Ambipolar Electrical Transport in Semiconducting Single-Wall Carbon Nanotubes" *Phys. Rev. Lett.* **87**, 256805-256808 (2001)
62. Chen J, Perebeinos V, Freitag M, Tsang J, Fu Q, Liu J, Avouris Ph "Bright Infrared Emission from Electrically Induced Excitons in Carbon Nanotubes" *Science* **310**, 1171-1174 (2005)
63. Freitag M, Chen J, Tersoff J, Tsang J C, Fu Q, Liu J, Avouris Ph "Mobile Ambipolar Domain in Carbon-Nanotube Infrared Emitters" *Phys. Rev. Lett.* **93**, 076803-076806 (2004)
64. Im J, Lee M, Myung S, Huang L, Rao S G, Lee D J, Koh J, Hong S "Directed-assembly of single-walled carbon nanotubes using self-assembled monolayer patterns comprising conjugated molecular wires" *Nanotechnol.* **17**, 3569-3573 (2006)
65. Hannon J B, Afzali A, Klinke Ch, Avouris Ph "Selective Placement of Carbon Nanotubes on Metal-Oxide Surfaces" *Langmuir* **21**, 8569-8571 (2005)
66. Wang Y, MasPOCH D, Zou S, Schatz G C, Smalley R E, Mirkin C A "Controlling the shape, orientation, and linkage of carbon nanotube features with nano affinity templates" *Proc. Natl. Acad. Sci. USA* **103**, 2026-2031 (2006)
67. Ph. Avouris and Ch. Klinke, private communication. This was in the context of the developments of the work described in Reference 65.
68. Kong J, Zhou C, Morpurgo A, Soh H T, Quate C F, Marcus C, Dai H "Synthesis, integration, and electrical properties of individual single-walled carbon nanotubes" *Appl. Phys. A* **69**, 305-308 (1999)
69. Zhang Y, Chang A, Cao J, Wang Q, Kim W, Li Y, Morris N, Yenilmez E, Kong J, Dai H "Electric-field-directed growth of aligned single-walled carbon nanotubes" *Appl. Phys. Lett.* **79**, 3155-3157 (2001)
70. Joselevich E, Lieber C M "Vectorial Growth of Metallic and Semiconducting Single-Wall Carbon Nanotubes" *Nano Lett.* **2**, 1137-1141 (2002)
71. Nagahara L A, Amlani I, Lewenstein J, Tsui R K "Directed placement of suspended carbon nanotubes for nanometer-scale assembly" *Appl. Phys. Lett.* **80**, 3826-3828 (2002)
72. Radu I, Hanein Y, Cobden D H "Oriented growth of single-wall carbon nanotubes using alumina patterns" *Nanotechnol.* **15**, 473-476 (2004)
73. Diehl M R, Yaliraki S N, Beckman R A, Barahona M, Heath J R "Self-Assembled, Deterministic Carbon Nanotube Wiring Networks" *Angew. Chem. Int. Ed.* **41**, 353-356 (2002)
74. Xin H, Woolley A T "Directional Orientation of Carbon Nanotubes on Surfaces Using a Gas Flow Cell" *Nano Lett.* **4**, 1481-1484 (2004)

75. Ismach A, Segev L, Wachtel E, Joselevich E "Atomic-Step-Templated Formation of Single Wall Carbon Nanotube Patterns" *Angew. Chem. Int. Ed.* **116**, 6266-6269 (2004)
76. Kang S J, Kocabas C, Ozel T, Shim M, Pimparkar N, Alam M A, Rotkin S V, Rogers J A "High-performance electronics using dense, perfectly aligned arrays of single-walled carbon nanotubes" *Nature Nanotechnol.* **2**, 230-236 (2007)
77. Hines D R, Mezheny S, Breban M, Williams E D, Ballarotto V W, Esen G, Southard A, Fuhrer M S "Nanotransfer printing of organic and carbon nanotube thin-film transistors on plastic substrates" *Appl. Phys. Lett.* **86**, 163101-163103 (2005)
78. Ahn J H, Kim H S, Lee K J, Jeon S, Kang S J, Sun Y, Nuzzo R G, Rogers J A "Heterogeneous Three-Dimensional Electronics by Use of Printed Semiconductor Nanomaterials" *Science* **314**, 1754 (2006)
79. Li S, Yan Y, Liu N, Chan-Park M B, Zhang Q "Transfer Printing of Submicrometer Patterns of Aligned Carbon Nanotubes onto Functionalized Electrodes" *Small* **3**, 616-621 (2007)
80. Huang S, Maynor B, Cai X, Liu J "Ultralong, Well Aligned Single-Walled Carbon Nanotube Architectures on Surfaces" *Adv. Mater.* **15**, 1651-1655 (2003)
81. Huang X M H, Caldwell R, Huang L, Jun S C, Huang M, Sfeir M Y, O'Brien S P, Hone J "Controlled Placement of Individual Carbon Nanotubes" *Nano Lett.* **5**, 1515-1518 (2005)
82. Chandra B, Caldwell R, Huang M, Huang L, Sfeir M Y, O'Brien S P, Heinz T F, Hone J "Electrical transport measurements of nanotubes with known (n, m) indices" *Phys. Stat. Sol. B* **243**, 3359-3364 (2006)
83. Cassell A, Franklin N, Tomblor T, Chan E, Han J, Dai H "Directed Growth of Free-Standing Single-Walled Carbon Nanotubes" *J. Am. Chem. Soc.* **121**, 7975-7976 (1999)
84. Franklin N R, Dai H "An Enhanced CVD Approach to Extensive Nanotube Networks with Directionality" *Adv. Mater.* **12**, 890-894 (2000)
85. Homma Y, Kobayashi Y, Ogino T, Yamashita T "Growth of suspended carbon nanotube networks on 100-nm-scale silicon pillars" *Appl. Phys. Lett.* **81**, 2261-2263 (2002)
86. Jung Y J, Homma Y, Vajtai R, Kobayashi Y, Ogino T, Ajayan P M "Straightening Suspended Single Walled Carbon Nanotubes by Ion Irradiation" *Nano Lett.* **4**, 1109-1113 (2004)
87. Matsumoto T, Homma Y, Kobayashi Y "Bridging Growth of Single-Walled Carbon Nanotubes on Nanostructures by Low-Pressure Hot-Filament Chemical Vapor Deposition" *Japn. J. Appl. Phys.* **44**, 7709-7712 (2005)
88. Homma Y, Tagaki D, Kobayashi Y "Suspended architecture formation process of single-walled carbon nanotubes" *Appl. Phys. Lett.* **88**, 023115-023117 (2006)
89. Jung Y J, Homma Y, Ogino T, Kobayashi Y, Takagi D, Wei B, Vajtai R, Ajayan P M "High-Density, Large-Area Single-Walled Carbon Nanotube Networks on Nanoscale Patterned Substrates" *J. Phys. Chem. B* **107**, 6859-6864 (2003)
90. Abrams Z R, Hanein Y "Tube-Tube and Tube-Surface Interactions in Straight Suspended Carbon Nanotube Structures" *J. Phys. Chem. B* **110**, 21419-21423 (2006)

91. Abrams Z R, Ioffe Z, Tsukernik A, Cheshnovsky O, Hanein Y "A complete scheme for creating predefined networks of individual carbon nanotubes" *accepted: Nano Lett. July 2007*
92. Abrams Z R, Lereah Y, Hanein Y "Transmission electron microscope imaging of single-walled carbon nanotube interactions and mechanics on nitride grids" *Nanotechnol.* **17**, 4706–4712 (2006)
93. Abrams Z R, Hanein Y "Radial deformation measurements of isolated pairs of single-walled carbon nanotubes" *Carbon* **45**, 738–743 (2007)
94. Minot E D, Yaish Y, Sazonova V, Park J Y, Brink M, McEuen P L "Tuning Carbon Nanotube Band Gaps with Strain" *Phys. Rev. Lett.* **90**, 156401-156404 (2003)
95. Homma Y, Takagi D, Suzuki S, Kanzaki K, Kobayashi Y "Electron-microscope imaging of single-walled carbon nanotubes grown on silicon and silicon oxide substrates" *J. Electron Microsc.* **54**, 3-7 (2005)
96. Kasumov Yu A, Khodos I I, Kocrak M, Kasumov A Yu "Scanning and transmission electron microscope images of suspended single-walled carbon nanotube" *Appl. Phys. Lett.* **89**, 013120-013122 (2006)
97. Private communication: this information came from a discussion with Prof. D. Tomanek of Michigan University.
98. Chen B, Gao M, Zuo J M, Qu S, Liu B, Huang Y "Binding energy of parallel carbon nanotubes" *Appl. Phys. Lett.* **83**, 3570-3571 (2003)
99. Hertel T, Walker R E, Avouris Ph "Deformation of carbon nanotubes by surface van der Waals forces" *Phys. Rev. B* **58**, 13870 (1998)
100. Tang T, Jagota A, Hui C Y "Adhesion between single-walled carbon nanotubes" *J. Appl. Phys.* **97**, 074304-074309 (2005)
101. Gupta S, Dharamvir K, Jindal V K "Elastic moduli of single-walled carbon nanotubes and their ropes" *Phys. Rev. B* **72**, 165428-165443 (2005)
102. Ruoff R S, Tersoff J, Lorents D C, Subramoney S, Chan B "Radial deformation of carbon nanotubes by van der Waals forces" *Nature* **364**, 514-516 (1993)
103. Bachilo S M, Balzano L, Herrera J E, Pompeo F, Resasco D E, Weisman R B "Narrow (n,m)-distribution of single-walled carbon nanotubes grown using a solid supported catalyst" *J. Am. Chem. Soc.* **125**, 11186-11187 (2003)
104. Sazonova V, Yaish Y, Ustunel H, Roundy D, Arias T A, McEuen P L "A tunable carbon nanotube electromechanical oscillator" *Nature* **431**, 284-287 (2004)

## 9 Appendix

### Appendix 1: Raman Spectroscopy

#### 9.1 The Physics of Raman Spectroscopy

A brief description of the physics behind Raman spectroscopy is presented here. Only the highlights of this method are presented. Further information can be found in existing literature.

A brief physical process describing the origin of the vibrational mode frequencies is given in Figure 56. The vibrational modes are used in both Raman and Infrared spectroscopy, with a difference in the physical process involved. The Rayleigh signal is of the same frequency as the initial input (laser). Raman spectroscopy (RS) is similar to IR spectroscopy (IRS) in that they are both dependant on the quantum selection rules that govern such vibrations. However, whereas in IRS, the vibrational modes are a result of the change in the induced *dipole* moment, RS arises from the change in the induced *polarizability*. This subtle difference means that for centro-symmetric molecules, one cannot have both IR and Raman modes active at the same time. In addition, IRS relates to photons emitted between two distinct energy levels in the vibration itself, whereas RS deals with the change of the photon energy from the central peak to those of the phonons (vibrational modes). Finally, since RS is a diffraction related process, the light resulting from RS is at an angle to the original light source direction (as in Bragg diffraction), whereas in IRS, the signal is always in the same direction as the source.

The Raman signal is caused by the induced change in polarizability, as described in Figure 57, which shows the mathematical relation between the polarization and the input photon frequency.

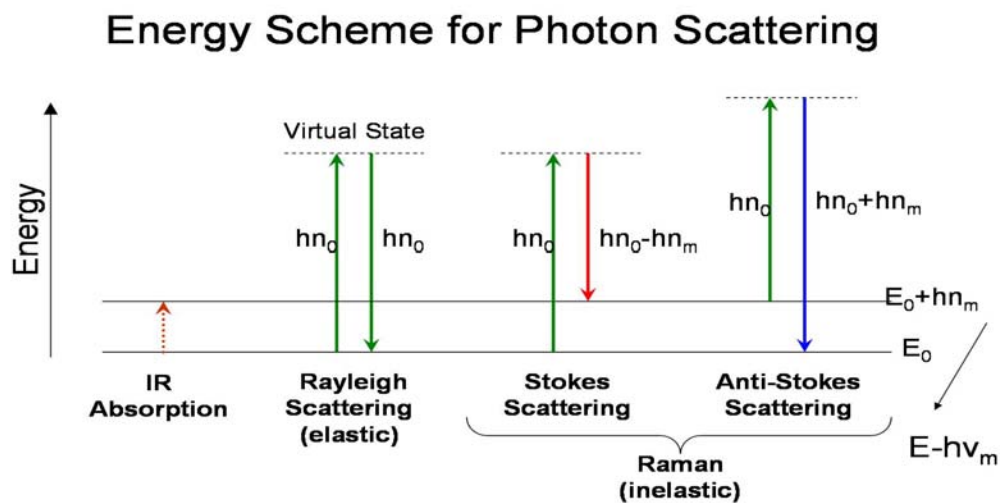


**Figure 56: Graphical Representation of the Raman Effect**

Also included are the IR and Rayleigh absorption. The energy  $h\nu_m$  is that of the vibrational modes – i.e. phonons.

## Scattering of radiation from a diatomic molecule

$q = q_0 \cos(2\pi\nu_m \cdot t)$   
 $E = E_0 \cos(2\pi\nu_0 \cdot t)$

OUTPUT

Induced dipole moment:  $P = \alpha E = \alpha E_0 \cos(2\pi\nu_0 \cdot t)$

For a small amplitude of vibration, the polarizability  $\alpha$  is a linear function of  $q$ :

$$\alpha = \alpha_0 + \left( \frac{\partial \alpha}{\partial q} \right)_{q=0} \cdot q + \dots$$

$$\Rightarrow P = \alpha_0 E_0 \cos(2\pi\nu_0 \cdot t) + \left( \frac{\partial \alpha}{\partial q} \right)_{q=0} \cdot q_0 \cos(2\pi\nu_m \cdot t) \cdot E_0 \cos(2\pi\nu_0 \cdot t) =$$

$$= \underbrace{\alpha_0 E_0 \cos(2\pi\nu_0 \cdot t)}_{\text{Rayleigh scattering}} + \frac{1}{2} \left( \frac{\partial \alpha}{\partial q} \right)_{q=0} q_0 E_0 [\underbrace{\cos(2\pi\{\nu_0 - \nu_m\} \cdot t)}_{\text{Stokes scattering}} + \underbrace{\cos(2\pi\{\nu_0 + \nu_m\} \cdot t)}_{\text{Anti-Stokes scattering}}]$$

**Figure 57: Source of Raman Signal from a Diatomic Molecule**

Displayed are the vibrational modes of a simple molecule induced by an interacting photon with incoming field  $E$ . The photon is scattered at both the same frequency (Rayleigh scattering), as well as given (or subtracted) an extra amount (Stokes/Anti-Stokes scattering).

To better understand the difference between IRS and RS, Figure 58 demonstrates two examples of molecules for which both RS and IRS occur. As can be seen, for each vibrational mode in these simple molecules, either the total dipole of the molecule will change (graphically presented by the asymmetry in the molecule), or the “size” of the dipole will change (i.e., change in polarizability). For  $\text{H}_2\text{O}$ , which is inherently non-symmetric, both RS and IRS occur, however, in  $\text{CO}_2$ , which is a linear molecule, the first mode, ( $\nu_1$ ) changes only the size of the dipole, and is thus only Raman active, whereas in the other two vibrational modes ( $\nu_2$ ,  $\nu_3$ ), the dipole changes, but its size on either “side” of the vibrational mode is the same, so that, on average, the net size of the dipole/polarizability remains unchanged, leaving these modes as IR active only.

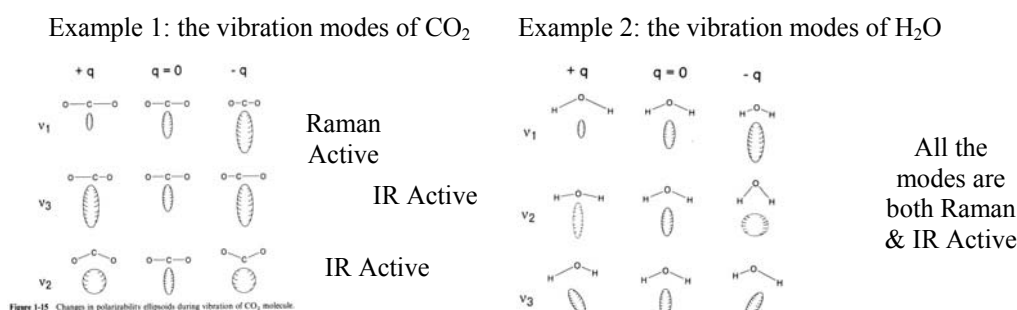


**Figure 58: Difference between Raman and IR Signals**

Two graphical representations demonstrating the differences between IR and Raman spectroscopy. The major difference is whether the dipole has changed, or whether the overall polarizability has changed.



The instrumentation used in RS consists of a laser, which is preferably tunable to an extent, an optical system for controlling the laser, a photon counter (such as a photomultiplier), and a system for isolating each wavelength (monochromator). Figure 59 displays a generic system for RS, quite similar to the one used in this report, other than the motorized chuck handling the substrate. These systems are usually quite compact and operate at room temperature. The Raman effect comprises a very small fraction, about 1 in  $10^7$ , of the incident photons.

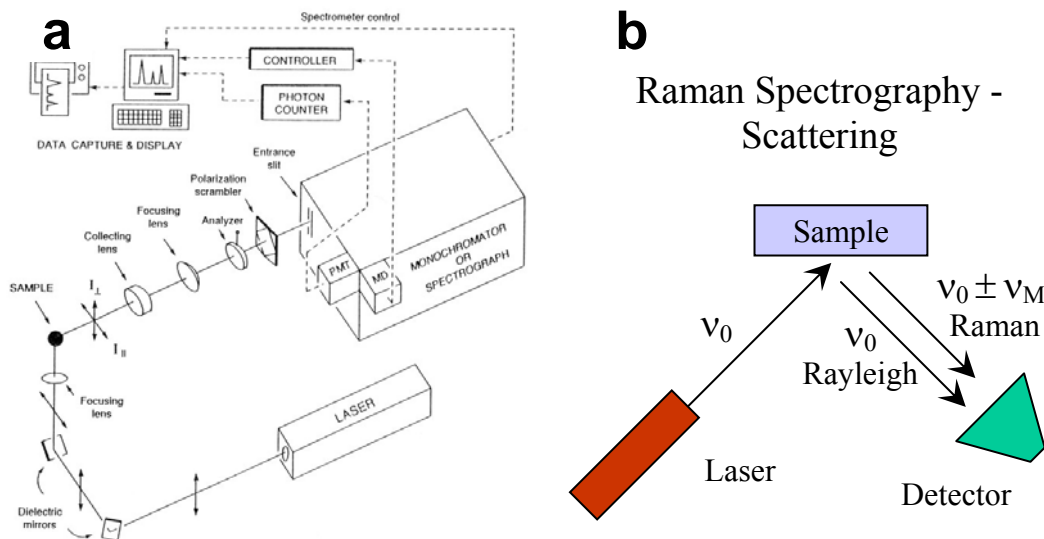


**Figure 59: Raman spectroscopy instrumentation.**

(a) Schematic of a typical RS system. (b) RS is a scattering effect, with the light scattered at a specific angle. The Rayleigh scattering is the bulk of the signal, with the offset (Stokes/Anti-Stokes) Raman signal consisting of only a small fraction of the scattered signal.

## 9.2 Spectral Information from SWCNTs

Figure 60 supplies some tables and graphs from some of the cited references [31,33]. The diameter of the SWCNTs can be found using equation (8) in the text. This, with the information in the table, can relate the exact (n,m) values of the specific nanotube. In addition, using equation (13), and detecting the shift in the G-band, as was done in the Results section, one can also isolate the (n,m) values. The DOS of a couple of SWCNTs are also displayed. The Van-Hove singularities are distinctly visible. To get the picture containing the valence and covalence bands (for SC SWCNTs), simply mirror-image each DOS to the left.

Possible  $(n, m)$  and their calculated  $\omega_{\text{RBM}}$  and  $E_{ii}$  values in the resonant window  $1.48 \leq E_{ii} \leq 1.68$  eV for  $E_{\text{laser}} = 1.58$  eV, where  $E_{ii} = E_{11}^{\text{M}}$  for metallic SWNTs and  $E_{ii} = E_{22}^{\text{S}}$  for semiconducting SWNTs (see Fig. 2a)

| $(n, m)$                         | $d_t$<br>(nm) | $\theta$<br>(°) | $\omega_{\text{RBM}}$ ( $\text{cm}^{-1}$ ) <sup>a</sup> |                            | $E_{11}^{\text{M}}$ <sup>b</sup><br>(eV) |      |
|----------------------------------|---------------|-----------------|---|----------------------------|--|------|
|                                  |               |                 | (calc.)   | (exp.)                     |  |      |
| (18, 6)                          | 1.72          | 13.9            | 144.4   | 144(2)                     | 1.49                                     | 1.40 |
| (19, 4)                          | 1.69          | 9.4             | 146.8   | —                          | 1.53                                     | 1.42 |
| (20, 2)                          | 1.67          | 4.7             | 148.3   | —                          | 1.55                                     | 1.42 |
| (21, 0)                          | 1.67          | 0.0             | 148.8   | <b>148(5)</b> <sup>c</sup> | 1.56                                     | 1.43 |
| (15, 9)                          | 1.67          | 21.8            | 148.8   | —                          | 1.51                                     | 1.46 |
| (12, 12)                         | 1.65          | 30.0            | 150.3   | <b>151(3)</b>              | 1.50                                     |      |
| (16, 7)                          | 1.62          | 17.3            | 153.0   | <b>154(5)</b>              | 1.57                                     | 1.49 |
| (17, 5)                          | 1.59          | 12.5            | 156.4   | <b>156(6)</b>              | 1.62                                     | 1.51 |
| (13, 10)                         | 1.59          | 25.7            | 156.4   | <b>156(1)</b>              | 1.58                                     | 1.55 |
| (18, 3)                          | 1.56          | 7.6             | 158.8   | 158(1)                     | 1.66                                     | 1.52 |
| (19, 1)                          | 1.55          | 2.5             | 160.0   | <b>160(3)</b>              | 1.68                                     | 1.54 |
| (14, 8)                          | 1.53          | 21.1            | 162.0   | 161(1)                     | 1.65                                     | 1.58 |
| (11, 11)                         | 1.51          | 30.0            | 164.0   | <b>164(1)</b>              | 1.63                                     |      |
| (15, 6)                          | 1.49          | 16.1            | 166.7   | <b>165(1)</b>              | 1.72                                     | 1.62 |
| (16, 4)                          | 1.46          | 10.9            | 170.4   | 169(1)                     | 1.79                                     | 1.64 |
| (17, 2)                          | 1.44          | 5.5             | 172.7   | 174(1)                     | 1.81                                     | 1.65 |
| (18, 0)                          | 1.43          | 0.0             | 173.5   | 176(1)                     | 1.83                                     | 1.65 |
| $E_{22}^{\text{S}}$ <sup>d</sup> |               |                 |   |                            |  |      |
| (14, 1)                          | 1.15          | 3.4             | 215.1   | 210(1)                     | 1.50                                     |      |
| (10, 6)                          | 1.11          | 21.8            | 223.1   | —                          | 1.51                                     |      |
| (9, 7)                           | 1.10          | 25.9            | 224.9   | —                          | 1.48                                     |      |
| (11, 4)                          | 1.07          | 14.9            | 232.2   | 229(1)                     | 1.60                                     |      |
| (10, 5)                          | 1.05          | 19.1            | 236.1   | 237(2)                     | 1.54                                     |      |
| (12, 2)                          | 1.04          | 7.6             | 238.2   | —                          | 1.66                                     |      |
| (8, 7)                           | 1.03          | 27.8            | 240.3   | 239(2)                     | 1.61                                     |      |
| (11, 3)                          | 1.01          | 11.7            | 244.7   | —                          | 1.57                                     |      |

Resonance with  $E_{33}^{\text{S}}$  and  $E_{44}^{\text{S}}$  is also possible under these conditions, but these resonant SWNTs are not listed in this table. The experimentally observed  $\omega_{\text{RBM}}$  values are also listed, along with the number of times (between parentheses) each  $(n, m)$  was found for a particular experiment on a particular sample [4]

<sup>a</sup> Bold face indicates those  $\omega_{\text{RBM}}$  observed to have a relatively large intensity.

<sup>b</sup> Two  $E_{11}^{\text{M}}$  values are given for each crystalline chiral  $(n, m)$  SWNT because of the trigonal warping effect, but armchair  $(n, m)$  nanotubes have only one  $E_{ii}$  value. Bold face indicates  $E_{ii}$  values predicted to have large intensities.

<sup>c</sup> In this particular experiment there was an ambiguity between (20, 2) and (21, 0) in the  $(n, m)$  assignment.

<sup>d</sup> Each semiconducting nanotube, such as those in resonance with  $E_{22}^{\text{S}}$ , has only one  $E_{22}^{\text{S}}$  value.

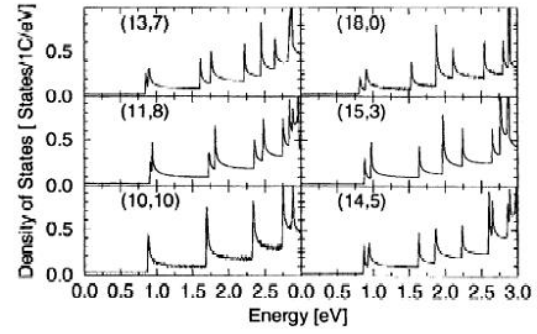
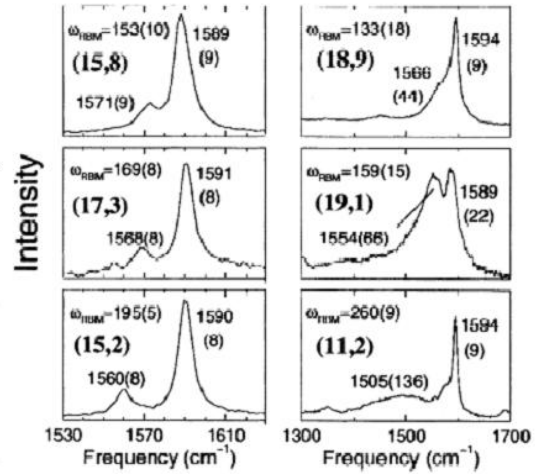


Fig. 3. The 1D electronic density of states versus energy (measured from the Fermi level) for several metallic nanotubes of approximately the same diameter, showing the effect of chirality on the van Hove singularities: (10, 10) (armchair), (11, 8), (13, 7), (14, 5), (15, 3) and (18, 0) (zigzag). Only the densities of states for the conduction  $\pi^*$ -band are shown; the mirror image of these plots gives the electronic density of states for the valence  $\pi$ -band [15] within the tight binding approximation, and assuming the overlap integral to be  $s=0$  [2].



**Figure 60: Tables and Graphs of Spectral Information from Nanotubes**

All information taken from Dresselhaus *et al.* [32,33]

## Appendix 2: CNTFET Device Equations

The following equations are taken from the cited references [8, 13, 40, 49, 94].

Beginning with the assumption that the gate capacitance  $C'_g$  is much *smaller* than the quantum capacitance ( $C_{gate} \ll C_Q$ ) as defined by:

$$C_{quantum} = \frac{4e^2}{\pi\hbar v_F} \equiv e^2 g(E) \quad (\text{a1})$$

with  $g(E)$  as the DOS of the 1-D SWCNT, and  $v_F$  being the Fermi velocity.

The back gate capacitance, per unit length, for a dielectric of thickness  $h$ , dielectric constant  $\epsilon$ , and a nanotube of diameter  $d$  is approximately given by:

$$\frac{C}{L} = \frac{2\pi\epsilon\epsilon_0}{\ln(1+2h/d)} \cong \frac{2\pi\epsilon\epsilon_0}{\ln(2h/d)} \quad (\text{a2})$$

so that we can consider the back-gate capacitance only in the calculations.

Under the assumption that SWCNTs are 1-D electronic wires with quantized wave numbers:

$$k_F = \frac{\pi}{4} n = \frac{\pi C'_g \Delta V_g}{4e} \quad (\text{a3})$$

The energy of the electrons in this 1-D system can be found, using relativistic notation as:

$$E = \pm \sqrt{(mv_o)^2 + (\hbar k v_o)^2} \quad (\text{a4})$$

Therefore, the velocity can also be found using the derivative of the energy:

$$v = \frac{1}{\hbar} \frac{dE}{dk} = \frac{\hbar^2 v_o^2 k}{E} \quad (\text{a5})$$

and the mass of the electron in the 1-D system can be found by:

$$m = \frac{\hbar}{3\pi\hbar v_o} \quad (\text{a6})$$

Furthermore, the conductance  $G$  of such a system, using the Drude model, is:

$$G_{1D} = \frac{4e^2}{h} \frac{\tau_F v_F}{L} = \frac{4e^2}{h} \frac{l_F}{L} \quad (\text{a7})$$

with  $l_F$  as the mean free path of the electrons at the Fermi energy level. In 1-D systems, a correlation between the mean velocity  $v_F$ , and the relaxation time  $\tau_F$  is:

$$\frac{v_F}{\tau_F} = \frac{v_o}{\tau_o} \quad (\text{a8})$$

with the “o” subscript signifying the relaxation time at high velocities. Now plugging in equations a1, a4, a5 and a8 into a7, we get:

$$G = \frac{4e^2}{h} \frac{(\tau_o/v_o)}{L} v_F^2 = \frac{4\tau_o e^2}{hL v_o} \frac{\hbar^2 v_o^2 \pi^2 C_g'^2 \Delta V_g^2}{e^2} \frac{1}{m^2 v_o^2 + \hbar^2 k^2 v_o^2}$$

here, we need to plug in the mass, a6, and the wave-number, a3, and after a bit of algebra:

$$G = \frac{4e^2}{h} \tau_o v_o \frac{9d^2 \pi^2 C_g'^2 \Delta V_g^2}{64e^2} \frac{1}{1 + \frac{9d^2 \pi^2 C_g'^2 \Delta V_g^2}{64e^2}} =$$

$$\frac{4e^2}{h} \tau_o v_o \frac{\left(\frac{\Delta V_g}{a}\right)^2}{1 + \left(\frac{\Delta V_g}{a}\right)^2} \quad (\text{a9})$$

with :  $a = \frac{8e}{3d\pi C_g'}$

where the term  $\tau_o v_o$  is equal to the mean free path at high energies.

To get the mobility of a Field Emission device, we need the derivative of the conductance, as a function of the gate voltage:

$$\mu_{FE} = \frac{L}{C_g'} \frac{dG}{dV_g} = \dots = \frac{3\pi d v_o}{h} e \tau_o \frac{\frac{\Delta V_g}{a}}{\left(1 + \left(\frac{\Delta V_g}{a}\right)^2\right)^2} \quad (\text{a10})$$

Thus we receive the formula for the effective mass of the electron (equation a6) as the first part of the equation.

Note that larger diameter SWCNTs ( $d$ ) result in smaller effective masses, and thus, higher mobilities, which is desirable.

From an experimental point of view, to calculate the mobility, one measures the current at a constant drain-source voltage  $V_{sd}$ , and for different gate voltages, to obtain:

$$\mu_n = \frac{L^2}{C_{total} V_{sd}} \frac{dI_{sd}}{dV_g} \quad (\text{a11})$$

and the typical formula for the current, at low voltages is:

$$I_{sd} = \frac{\mu_n C_{total}}{2L} (V_g - V_{th})^2 \quad (\text{a12})$$

A final equation with relevance to this work is the relation between the strain on a SWCNT and its band-gap. Since the nanotubes are assumed to be completely taut, very little strain is expected, however, for any measurable amount of strain,  $\sigma$ , the change in band-gap energy is assumed to act according (to the first order,) to:

$$E_{gap} = E_{gap}^0 + \frac{dE_{gap}}{d\sigma} \sigma \quad (\text{a13})$$

### 9.3 Fabrication Recipes

#### Appendix 3: Photo-Lithography Protocol for S1818

| General Description |                     |                  |
|---------------------|---------------------|------------------|
| S1818               |                     |                  |
| Objective:          | Author: Yael Hanein | Date: 12/29/2003 |
| Comments:           |                     |                  |
|                     |                     |                  |

| Process   |                                |   |
|-----------|--------------------------------|---|
| Singe     |                                | Comments:<br>Mask aligner:<br>11 mW/cm <sup>2</sup> |
|           | 170 deg, 5 min                 |   |
| Spin      |                                |   |
|           | 100 rpm/sec to 2500 rpm 40 sec |   |
| Pre bake  |                                |   |
|           | 100 deg 2 min                  |   |
| Exposure  |                                |   |
|           | 20 sec                         |   |
| Develop   |                                |   |
|           | MF319, 40 sec                  |   |
| Rinse     |                                |   |
|           | DI Water                       |   |
| Post bake |                                |   |
|           | 100 deg 5 min                  |   |

| General Description |                   |  |
|---------------------|-------------------|--|
| Thickness           | 2.6 $\mu\text{m}$ |  |
|                     |                   |  |

#### Appendix 4: Photo-Lithography Protocol for TI-35ES

| General Description |                         |                 |
|---------------------|-------------------------|-----------------|
| TI-35ES             |                         |                 |
| Objective:          | Author: Moti- Ben David | Date: 10/3/2007 |
| Comments:           |                         |                 |
|                     |                         |                 |

| Process        |   |
|----------------|---|
| Singe          |   |
|                | 170 deg, 10 min   |
| Spin           |   |
|                | 100 rpm/sec to 500 rpm 5 sec<br>300 rpm/sec to 3000 rpm 40 sec                              |
| Pre bake       |   |
|                | 100 deg 2 min   |
| Exposure       |   |
|                | $Dose = 200 \frac{mJ}{cm^2}$ , 17 sec (MJB3, MA6 = $11.7 \frac{mW}{cm^2}$ )                 |
| Delay          |   |
|                | <i>at room temperature for 20 min</i>   |
| Reversal bake  |   |
|                | $100^{\circ}C - 120^{\circ}C$ , 3 min <i>on the hotplate</i>                                |
| Flood exposure |   |
|                | $Dose = 700 \frac{mJ}{cm^2}$ , 60 sec (MJB3, MA6 = $11.7 \frac{mW}{cm^2}$ )                 |
| Develop        |   |
|                | <i>Cleared + 20% for side wall profile (20 – 30 sec) , 726MIF</i>                           |
| Rinse          |   |
|                | DI Water  |
| Hard bake      |   |
|                | $135^{\circ}C - 145^{\circ}C$ , 2 min <i>on the hotplate (loosin g side – wall profile)</i> |

### Appendix 5: Photo-Lithography Protocol for AZ-5214

| General Description |                        |                  |
|---------------------|------------------------|------------------|
| AZ 5214E            |                        |                  |
| lithography         | Author: Moti Ben-David | Date: 06/12/2005 |
| Comments:           |                        |                  |
|                     |                        |                  |

| Process        |                                |
|----------------|--------------------------------|
| Singe          |                                |
|                | 120 deg 5min                   |
| Spin           |                                |
|                | 250 rpm/sec to 2000 rpm 40 sec |
| Pre bake       |                                |
|                | 110 deg 2 min                  |
| Exposure       |                                |
|                | 1.2 sec (MA-6)                 |
| Reversal bake  |                                |
|                | 120 deg 2min                   |
| Flood exposure |                                |
|                | 60sec (MA-6)                   |
| Develop        |                                |
|                | AZ726MIF 25 sec                |
| Rinse          |                                |
|                | DI Water                       |
| Post bake      |                                |
|                | 120 deg 2min                   |

| General Description |                   |
|---------------------|-------------------|
| Thickness           | 2.5 $\mu\text{m}$ |
|                     |                   |



**Appendix 6: RIE Protocol**

| General Description      |                      |                 |
|--------------------------|----------------------|-----------------|
| SiO <sub>2</sub> etching |                      |                 |
| Objective:               | Author: Itsik Kalifa | Date: 14.9.2004 |
| Comments:                |                      |                 |
|                          |                      |                 |

| Process                |          |  |
|------------------------|----------|--|
| RF                     |          |  |
|                        | 200w     |  |
| Reflected              |          |  |
|                        | 0w       |  |
| Plasma Temperature     |          |  |
|                        | 18 c     |  |
| Gas 1-O <sub>2</sub>   |          |  |
|                        | 6 sccm   |  |
| Gas 2-CHF <sub>3</sub> |          |  |
|                        | 100 sccm |  |
| Gas 3-Ar               |          |  |
|                        | 0sccm    |  |
| Refractive index       |          |  |
|                        | 1.46     |  |
| Chamber Pressure       |          |  |
|                        | 50mTorr  |  |

| General Description |           |  |
|---------------------|-----------|--|
| Etching Rate        | 50 nm/min |  |
|                     |           |  |

## Appendix 7: DRIE Protocol

| General Description   |  |                |
|---|--|----------------|
| DRIE O <sub>2</sub> /SF <sub>6</sub> /C <sub>4</sub> F <sub>8</sub> Silicon Etching |  |                |
| Program:  | 25mo2ext                                   | 25 micron etch |
| Comments:   | SiO <sub>2</sub> hard mask                 |                |
|   | C <sub>4</sub> F <sub>8</sub> Teflon layer |                |

| Process                       |                       |                      |
|-------------------------------|-----------------------|----------------------|
| RF                            |                       | Pre-selected process |
|                               | 60/600W 13.56MHz      |                      |
| C <sub>4</sub> F <sub>8</sub> |                       |                      |
|                               | Deposit: 70 Etch: 0.5 |                      |
| SF <sub>6</sub>               |                       |                      |
|                               | Deposit: 0.5 Etch: 60 |                      |
| O <sub>2</sub>                |                       |                      |
|                               | Deposit: 0.5 Etch: 10 |                      |
| Ar                            |                       |                      |
|                               | Deposit: 40 Etch: 10  |                      |

| General Description                |                              |          |
|------------------------------------|------------------------------|----------|
| Etching Rate                       | 3-4 $\mu\text{m}/\text{min}$ | 37 loops |
| Selectivity (SiO <sub>2</sub> :Si) | (50-100:1)                   |          |

**Appendix 8: Protocol for CVD Synthesis of Carbon Nanotubes – C-CVD**

(Updated by Ze'ev Abrams, April 2007)

Sample \_\_\_\_\_

Name(s): \_\_\_\_\_

Comments: \_\_\_\_\_

\_\_\_\_\_

\_\_\_\_\_

*Clean all tools and dishes. (Acetone + IPA)***Catalyst Preparation**

- Iron (III) nitrate nonahydrate, 99.99%, Lot#: \_\_\_\_\_
- # \_\_\_\_\_ granules into 20cc of IPA. OR: \_\_\_\_\_
- Sonicate (55kHz) for 40 min.
- Centrifuge 1.5cc at 6200rpm for 10 min. OR: \_\_\_\_\_

**Sample Cleaning**

- Rinse sample in Acetone + sonicate for 1 min.
- Rinse sample in IPA + sonicate for 1 min.
- Dry with Nitrogen.
- Place on Hot Plate (setting 1-2 = 90-150° C)

**Sample Preparation – (Plasma) PDMS stamp**

Stamp Type/Date \_\_\_\_\_

- Drop 3 catalyst solution drops onto the stamp.
- Wait 10 seconds. OR: \_\_\_\_\_
- Dry with Nitrogen.
- Attach stamp to substrate – Sample above stamp, top down! (Push down with finger to remove bubbles)
- Wait 10 min.
- Remove substrate from stamp.

**Sample Preparation – without stamp**

- Drop 2 / 3 catalyst solution drops onto substrate.
- Wait 10 seconds.
- Rinse in Hexane cup.
- Dry immediately with Nitrogen.

**C-CVD**

- Protocol used: \_\_\_\_\_



## Appendix 9: Additional Images

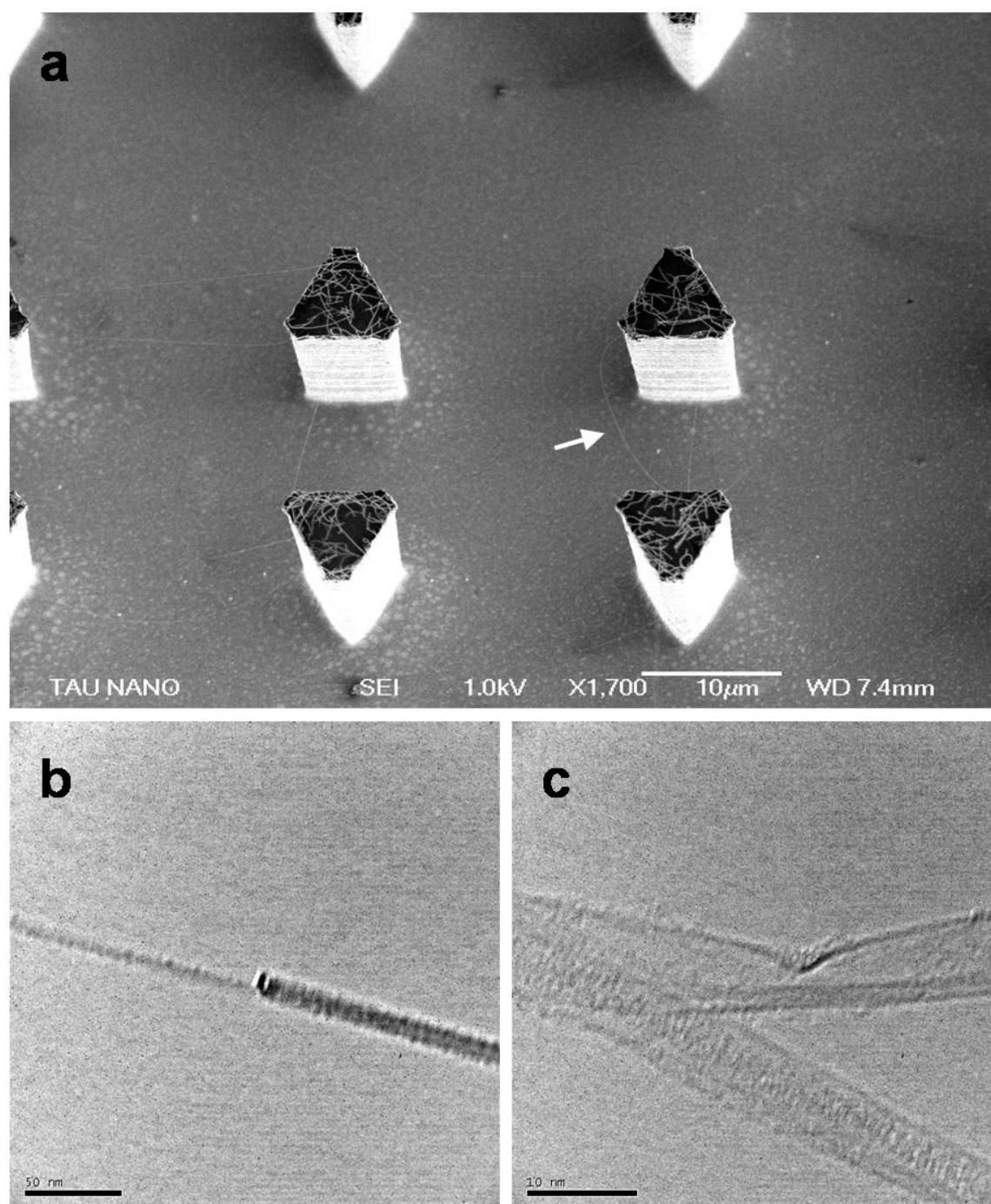


**Figure 61: Additional Images**

(a) Triangular pillars with suspended nanotubes. The white arrow points to a non-taut suspended nanotube, do to the high tangential angle between the nanotube and the pillar top curvature. (b) Out of focus TEM image of a SWCNT ending midway along another suspended segment of SWCNT. (c) A close up of the buckle described in the text.

## תקציר

בעזרת הכלים שנוצרו עם פיתוח הננו-טכנולוגיה, רבים מהחלקים הפעילים של התקנים אלקטרוניים מוזערו לרמה המולקולארית. האלמנטים הננומטרים והננו-חומרים הללו בעלי תכונות משופרות בהשוואה לאלמנטים המיוצרים בשיטה הנפחית הרגילה בזכות תהליכים פיזיקאליים ייחודיים המתרחשים כאשר מתקרבים למימדים מזעריים אלו, לדוגמא אפקטים קוונטים. אחד ממובילי המחקר בתחום הננו-חומרים הוא תחום הננו-צינוריות פחמן, אשר מספקות תכונות ללא מתחרים לאפליקציות רבות. ברם, כאשר דנים באספקטים שונים בפבריקציה ואינטגרציה של הננו-צינוריות בננו-התקנים ובפרט, בננו-מעגלים, אנו נתקלים במכשול משמעותי: כיצד ניתן לתמרן את האובייקטים הננומטרים הללו, כך שנוכל לשלבם, למקמם ולבודד אחד מן השני?

מחקר זה מתאר שיטה למיקום פרטני של צינוריות פחמן מסוג single walled במבנה שנקבע מראש, תוך שימוש בשיטה של ננו-הטבעה אשר אינה תלויה בסוג המצע והמתאימה למעגלים משולבים. השיטה מתבססת על גידול של ננו-צינוריות בין מיקרו-עמודים מסיליקון, דבר היוצר רשת של ננו-צינוריות תלויות ומתוחות, ולאחר מכן הטבעתה של רשת זו על מצע אחר, פעולה המשמרת את האופי הנקי, ארוך וישר של הננו-צינוריות. שיטה זו לא דורשת מהמצע להיות חשוף לטמפרטורות גבוהות, כנדרש בדרך כלל בגידול ננו-צינוריות על מצע, כמו כן ניתן להשתמש בשיטה זו עבור סוגים שונים של מצעים ושכבות דקות.

ניתן תאור מודל של יצירת רשת התלויה בין עמודי סיליקון, זאת בנוסף לתיאור ולהדגמת שיטת מיפוי הרשת על ידי ספקטרוסקופיית Raman. מיפוי זה יכול לשמש לזיהוי של סוג הננו-צינורית ברשת התלויה לפני ההטבעה, פעולה אשר ניתן לשלבה בשיטה כללית יותר לצורך הטבעת רשתות גדולות ושלמות של ננו-צינורות.

התוצאות המתוארות להלן הינן בין הטובות ביותר בהצגת יכולת שליטה במיקומם של ננו-צינוריות פחמן. בידי השיטה המתוארת לספק התקדמות טכנולוגית לקראת ארגון של רכיבים מולקולרים בגדלים ננומטרים.

# **אוניברסיטת תל-אביב**

הפקולטה להנדסה על שם איבי ואלדר פליישמן

## **סידור רשתות של ננו-צינוריות פחמן**

חיבור זה הוגש כעבודת גמר לקראת התואר  
"מוסמך אוניברסיטה" בהנדסת חשמל ואלקטרוניקה

על ידי

**זאב אייברמס**

העבודה נעשתה במחלקה להנדסת חשמל-פיסיקלית  
בהנחיית ד"ר יעל חנין

יולי 2007  
תמוז תשס"ז

# **אוניברסיטת תל-אביב**

הפקולטה להנדסה על שם איבי ואלדר פליישמן

## **סידור רשתות של ננו-צינוריות פחמן**

חיבור זה הוגש כעבודת גמר לקראת התואר  
"מוסמך אוניברסיטה" בהנדסת חשמל ואלקטרוניקה

על ידי

**זאב אייברמס**

יולי 2007  
תמוז תשס"ז